THESIS FOR THE DEGREE OF DOCTOR OF PHILOSOPHY

Performance Evaluation and Life Cycle Cost Analysis of the Electrical Generation Unit of a Wave Energy Converter

PINAR TOKAT

Department of Electrical Engineering
Division of Electric Power Engineering
CHALMERS UNIVERSITY OF TECHNOLOGY
Gothenburg, Sweden, 2018

Performance Evaluation and Life Cycle Cost Analysis of the Electrical Generation Unit of a Wave Energy Converter
PINAR TOKAT
ISBN 978-91-7597-705-8

Doktorsavhandlingar vid Chalmers Tekniska Högskola
Ny serie nr. 4386
ISSN 0346-718X

Department of Electrical Engineering
Division of Electric Power Engineering
Chalmers University of Technology
SE–412 96 Gothenburg
Sweden
Telephone +46 (0)31–772 1000

Printed by Chalmers Reproservice
Gothenburg, Sweden, 2018

To my family

Performance Evaluation and Life Cycle Cost Analysis of the Electrical Generation Unit of a Wave Energy Converter

PINAR TOKAT
Department of Electrical Engineering
Chalmers University of Technology

Abstract

The main focus of this work is the performance and the economical assessment of a radial flux generator that is used in wave power applications. The wave energy converter (WEC) used in this work is a point absorber, that is considered to move only in heave. The generation unit of the WEC consists of a permanent magnet machine and a power electronic converter.

The straight and v-shaped interior mounted permanent magnet generators, surface mounted permanent magnet generator and neodymium and ferrite assisted synchronous reluctance generators are selected as the main generator designs to be studied in this work. These designs are analysed using finite element method (FEM) and the annual energy productions and losses are quantified. Furthermore, some design variations such as, different iron materials, stator slot geometries and a SiC MOSFET based converter are investigated, in order to assess the impact of a specific design variation on the energy efficiency. An economical evaluation of these variants using the life cycle cost (LCC) analysis is performed, in order to quantify the economical consequences of the energy losses during the operational life time, as well as determining the costs of the initial generator investment. The results obtained suggest favorable WEC generator types and design alterations for LCC improvements.

An important finding is that the PM assisted SRM generator provides the best energy performance, given the same geometry and material limitations. The annual energy production achieved by the SMPM generator is fairly similar to that of the IPM generator, despite not being able to provide the required torque at high speed operations, since the high speed operations occur rarely. Moreover, it is found that the poor field weakening trajectory of the SMPM can be improved by placing iron pieces at magnet sides. Another interesting result is that even though the annual energy production is increased when the rotor material is replaced by a cobalt-iron, due to its high costs, this design was not found economically favorable. The design variation that improves the electric generation system of the WEC to the highest degree is found to be the SiC MOSFET based converter design, rather than the IGBT variant. The annual energy losses decrease by 5 MWh, due to up to 3 times lower converter losses. Owing to the substantial energy improvement, the SiC MOSFET case is the economically favorable choice compared to the generation system that uses an IGBT converter, despite the MOSFET modules being 7 times more costly than its IGBT counterpart.

Acknowledgments

The researched is financed by the Ocean Energy Center, Västra Götalandsregionen and Chalmers Area of Advance. The financial support is gratefully appreciated.

First and foremost, I would like to express my gratitude to my main supervisor Prof. Torbjörn Thiringer, for his never ending support, guidance and encouragements during the project and off work. Furthermore, a special thanks to my co-supervisor Dr. Emma Grunditz for valuable discussions. I would also like to thank my examiner Prof. Ola Carlson for his support. The help received from Dr. Guilherme Moura Paredes regarding the hydrodynamic simulations is sincerely appreciated.

I would like to take this opportunity to thank all my friends and colleagues at Electric Power Engineering, for making it possible to work in a very pleasant environment.

Finally, I would like to thank my family for their unconditional love and support.

Preface

This project was initially introduced by the Ocean Energy Center at Chalmers University of Technology and financed by Västra Götalandsregionen, in 2012 and the task for the Electric Power Engineering was to design a suitable electric generation unit for a single point absorber type WEC. The present PhD work was afterwards funded by the Chalmers Energy Initiative (CEI) and with the support of CEI, a guest researcher Dr. Guilherme Moura Paredes was engaged to further develop the single point absorber model, calculating wave power and wave energy estimates, as well as the hydrodynamic simulation of the updated single point absorber model.

List of Nomenclature

FW	Field weakening
IPM	Interior Mounted Permanent Magnet
LCC	Life Cycle Cost
MTPA	Maximum Torque per Ampere
NPVL	Net Present Value of Losses
SF	Stacking Factor
SMPM	Surface Mounted Permanent Magnet
SRM	Synchronous Reluctance Machine
VPM	V-shaped Interior Permanent Magnet
WEC	Wave Energy Converter
a	Wave amplitude
A	Added mass
B	Radiation damping
B	Magnetic flux density
C	Hydrostatic stiffness
C	Wave celerity
C_g	Group celerity for irregular waves
c_w	Wave force coefficients
d	Water depth
e	Induced voltage
E_{on}	On-state losses
E_{off}	Off-state losses
F	Fetch
F	Force
f_{sw}	Switching frequency
g	Gravitational acceleration
H	Field intensity
H	Wave height
H_s	Significant wave height
i	Current

J	Current density
k	Wave number
L	Inductance
M	Modulation index
M	Buoy mass
N	Number of turns
n_p	Number of pole pairs
N_{pb}	Number of parallel branches
P	Power
R	Resistance
R_{F0}	Internal resistance of the diode
R_T	Internal resistance of the semiconductor switch
$\Re$	Reluctance
$S_{JONSWAP}$	JONSWAP spectrum
S_{PM}	Pierson-Moskowitz spectrum
T	Wave period
t_{bl}	Blanking time
T_e	Energy period
T_e	Electrodynamic Torque
T_m	Magnet Torque
T_r	Reluctance Torque
T_z	Mean wave period
u	Voltage
V_{DC}	DC-link voltage
V_{F0}	Constant forward diode voltage drop
V_T	Offset voltage of the semiconductor switch
α	Phillips constant
β	Current angle
β	Parallel conduction angle
γ	Shape factor
ϵ	Phase shift of wave elevation
η	Wave elevation

η	Efficiency
θ_w	Phase shift of wave induced forces
λ	Wave length
μ_o	Permeability of free space
μ_r	Relative permeability
ξ	Buoy displacement
ρ	Water density
ρ_{cu}	Electrical resistivity of copper
σ	Spectral width parameter
ϕ	Phase shift of the buoy displacement
ϕ	Load angle
φ	Angle of displacement power factor
Φ_c	Flux in a coil
Ψ	Flux Linkage
Ψ_m	Magnet flux linkage
ω	Angular frequency
ω_m	Maximum angular frequency of the wave spectrum
ω_r	Angular speed of magnet rotation

Contents

Chapter 1

Introduction

1.1 Background

Due to the increasing population, the higher life standards and the technological developments, the electricity demand has been growing steadily. In order to supply the growing energy demand, whilst not contributing to more greenhouse gas emissions, the popularity of the sustainable energy sources for electricity generation has been increasing. The European Union 2020 climate and energy package aims to reduce the greenhouse gas emissions and increase the amount of energy produced by the sustainable resources in Europe [1].

Solar power and wind power are popular sustainable energy sources and are widely available for electricity production. Another promising renewable energy source, ocean wave power, is currently at the developing stages. The power from the sun that heats the earth's surface causes a heat difference, which generates winds. Winds, that are generated by solar heating, blow over large bodies of water and generates ocean waves, therefore the wave energy can be considered as a concentrated form of the solar energy [2]. Once generated, waves can travel significantly long distances with little energy loss, until they interact with the seabed at near shore areas [3]. A recent study states that "the wave energy provides 15-20 times more available energy per square meter than either wind or solar" [4]. The theoretical gross wave energy resource is estimated to be 3.5 TW, excluding the wave areas that have less than 5 kW/m wave power and the net resource, where the ice covered areas are eliminated from calculation, is estimated to be 3 TW. The gross and net theoretical resources in Europe are 381 GW and 286 GW, respectively, according to [5]. It is estimated that the global wave energy potential is approximately 2000 TWh annually, in [6]. Portugal, France and the UK are identified as some of the European countries that have the highest wave energy potential. In the UK, the practical offshore resource is found to be 50 TWh per year [7].

Compared with the solar and wind energy sources, ocean waves have smaller power fluctuations over a long period of time, therefore it can be considered as a more stable renewable energy source. Furthermore, it is economically comparable to solar and wind energies [8]. However, despite the large potential and promising aspects of the wave energy, currently there are very few commercial wave energy projects in operation or under construction. In 2016, it is

determined that the total commercial ocean energy capacity in operation is 0.5 GW, whilst 1.7 GW is under construction. Most of this capacity is achieved by tidal power applications and only 1% is accounted for by wave energy applications [9]. One of the main challenges regarding electricity production through ocean waves is the development of a mechanical system that can harness the wave energy effectively. Another important issue is the fluctuating power levels, since the available wave power can significantly differ from calm sea states to extreme sea states. This brings up the challenge of designing a wave energy converter (WEC) that can operate efficiently at the sea states with highest energy potentials, yet is able to withstand the highly excited sea states [10]. Furthermore, the requirements on the system components in order to be able to operate in the harsh ocean environment and/or wet devices, lead to high investment costs. Therefore, in order for the wave energy to be an attractive energy source, reducing the component cost and increasing the efficiency of the WEC technologies are highly important.

1.2 Previous Work and Challenges

There are many studies regarding the WEC generation unit, such as [7], where an overview of the current electric generator technology for the WECs are presented, however this work does not focus any specific operation and is rather a theoretical comparison.

The point absorber technology is fairly popular amongst other WEC types, due to the simplicity of the design. [11] presents an effective model predictive control of a point absorber in order to maximize the energy capture, however the electrical generation system is not specified. Furthermore, many studies using the point absorbers consider a linear electric generator, such as [12], which suggests an optimization of the linear PM generator of the WEC for a fairly basic buoy type WEC and [13], where results from an experiment regarding the Seabased system linear generator are presented.

The point absorber systems that use a rotational generator for electric power generation are not as available in literature. There are mere a handful of studies using this configuration, one of which is presented in [14], where, a constrained PTO and an oversized unconstrained PTO for a single capture and a double capture point absorbers are compared. Another valuable paper using the same system is presented in [15], where a tunable control strategy is introduced in order to suggest an effective trade off between the unconstrained high power extraction and a constrained PTO for a viable electrical device rating. Despite the very few valuable studies mentioned, there is a lack of investigations incorporating the radial flux machines for a point absorber type WEC. There are however some other marine energy concepts that use rotational machines as the electrical generator. In [16], a doubly fed induction generator is used for a surge WEC and in [17] a permanent magnet synchronous generator is used in a fixed pitch vertical axis marine current turbine. The main focus in the mentioned studies are not on the machine design, rather on the machine performance or overall device control for a pre-decided generator. However, an important aspect regarding the sustainable energy or any other industry application that needs adequate investigation is the design and evaluation of the electrical generation unit. The selection of an appropriate electric generator is crucial, since the generation system efficiency is highly dependent on the electrical machine efficiency. A usual practice regarding the

suitable generation selection for a specific application is the comparison of different options. such a comparison is presented in [18], where the performances of a surface mounted permanent magnet (SMPM) generator and an interior mounted permanent magnet (IPM) generator used in a 5 MW wind power application is investigated.

The SMPM and IPM are very common types of permanent magnet machines and used widely in various industrial applications. In [19] a comparison between SMPM and IPM motor drives for an electric vehicle application is presented, whereas [20] shows a similar comparison for high speed applications. Although valuable, the results are not applicable to a lower speed application like the wave energy. In [21] five different interior mounted PM machine topologies including surface mounted PM, straight, v-shaped and w-shaped interior mounted PM motors, are investigated for a hybrid electric vehicle. Moreover, in [22] a straight, v-shaped and u-shaped interior mounted PM motors with different stator designs are compared. Both studies include varying magnet volumes, which makes it challenging to economically quantify the energy performances.

Wave power studies regarding the synchronous reluctance generator is almost non existent, yet it is a promising machine type and is used for electric vehicle and other renewable energy applications. [23] compares the performance of a synchronous reluctance generator and [24] compares the permanent magnet assisted synchronous reluctance generator with an IPM generator performance for a wind power application. The mentioned two studies present very valuable insight, however they are conducted for a very high power level and lower rated speed. A performance assessment for ferrite and neodymium assisted synchronous reluctance machines is studied in [25] for an unspecified operation.

An extensive generator study for a wave power application is presented in [26], where an efficiency comparison between the brushed dc, induction, brushless dc and synchronous reluctance generators and drives is presented, yet the investigated average power rating is quite low, circa 100 W. In another extensive study [27], SMPM, inset mounted and three interior mounted (conventional, v-shaped and spoke) permanent magnet motors are compared for a specific vehicle application, yet the focus in this article is limited to fault-tolerance when the machines are used as in-wheel motors.

Performance studies are easy to come by in the literature for electrical machines, however, the energy efficiency comparison of different designs are not entirely sufficient in order to determine a favorable one, since the design with highest energy efficiency might not be the most economically favorable. In order to select the design that is both economically and energy-wise favorable for an application, a life cycle cost analysis is needed to be performed. In [28], a life cycle cost analysis for IGBT and SiC MOSFET wind power converters is conducted, however the study does not include the electric generator. [29] presents the life cycle cost as well as the environmental costs of a synchronous reluctance machine, where the construction, energy losses, emission and the end of life costs are included in the analysis, however the main focus is on the environmental costs rather than the cost of the generator performance. A life cycle assessment study on wave energy is shown in [30], where the emission costs, life cycle assessment and life cycle cost analysis is performed for the WaveStar WEC, In this work the electrical generation unit is not specified and the LCC analysis is only available for the cost of energy for the whole system.

Missing in available literature is an extensive electrical generation unit investigation for wave energy applications, where various materials, rotor geometries and the power electronic converters are quantified from an energy point of view, as well as the life cycle cost aspect, in order to obtain an economically favorable solution.

1.3 Purpose of the Work and Contributions

The purpose of this work is to evaluate different generator design with various rotor topologies and materials from an energy perspective and economically quantifying the impacts of these design variations through LCC analysis in order to select an economically favorable generator design for a specific wave energy application.

This work considers surface mounted and interior permanent magnet machines, both traditional designs and variations, as well as the permanent magnet assisted synchronous reluctance machine, with neodymium and ferrite magnets. The generation unit is dimensioned based on the power level obtained from a single point absorber simulation. The surface mounted, straight and v-shaped interior mounted and the neodymium permanent magnet assisted synchronous reluctance generators are selected to be the four main types of the investigated WEC generators. The outer diameter and axial length, the electric steel material and volume, copper and permanent magnet volumes of the main designs are kept identical, for a fair comparison of the generator performance. Following the initial assessment, a series of geometric and material alterations are to be investigated in order to understand the corresponding impacts of these alteration on the generation performance.

All main designs and alterations are economically evaluated through the life cycle cost analysis, in order to determine the relation between the life cycle cost and energy performance, as well as the costs of construction and materials.

The main contributions of this work are,

- Quantifying the life cycle cost of different generator designs that are investigated throughout the work.
- Quantifying the energy capture of using different types of permanent magnet and permanent magnet assisted synchronous reluctance machine WEC generators.
- Evaluating the economic impact of a SiC MOSFET based converter instead of the traditional IGBT based one, using life cycle cost analysis.
- Establishing the performance difference between the ferrite and neodymium permanent magnet assisted synchronous reluctance machines used as WEC generators.
- Determining the impact of different electric steels materials, as well as different stacking factors of the investigated laminations, on generator performance.
- Establishing the performance variation of different inset generator designs, based on the main surface mounted permanent magnet generator design.

- Evaluating the effect of the stator slot size variation on the generator performance.

1.4 List of Publications

1. P. Tokat and T. Thiringer, ”Sizing of IPM Generator for a Single Point Absorber Type Wave Energy Converter,” in IEEE Transactions on Energy Conversion, vol. PP, no. 99, pp. 1-1.

2. P. Tokat and T. Thiringer, ”Comparing IPM and SMPM as a WEC generator from a LCC perspective,” 2017 19th European Conference on Power Electronics and Applications (EPE’17 ECCE Europe), Warsaw, 2017, pp. P.1-P.6.

3. P. Tokat and T. Thiringer, ”The effect of the magnet placement for an internal permanent magnet wave energy converter generator,” 2016 XXII. International Conference on Electrical Machines (ICEM), Lausanne, 2016, pp. 2086-2092.

4. P. Tokat and T. Thiringer, ”Comparison of IPM, VPM, SMPM and PM-Assisted SRM Generator used as a WEC generator,”, submitted to XXIII. International Conference on Electrical Machines (ICEM’2018)

Not related to the work,

1. P. Tokat, T. Thiringer, and P. Chen, ”Development of an Analytically Described Pitch Regulator for a Wind Turbine to Be Used for Grid Disturbance Studies,” Hindawi Journal of Energy, vol. 2013, Article ID 203174, 9 pages, 2013.

Chapter 2

Hydrodynamic Theory

2.1 Wave Energy Converter Technologies

Ocean waves contain a tremendous energy potential. The device that captures the ocean wave energy, (usually for electric power generation) is called the wave energy converter. Some of the main parts of the wave energy converters are the power takeoff (PTO) and the electrical generation unit, which consists of the electric generator and the power electronic converter. This thesis focuses on the electrical generation unit of a single point absorber type WEC with a rotational electric generator.

The power takeoff of a wave energy converter is the mechanism that transfers the absorbed wave energy into usable electricity [31] and is the most distinctive part of the WEC, therefore the WECs are usually classified according to their PTO technologies. Some of the most common types of PTOs are oscillating water column [32],[33], hinged contour devices [34] and overtopping devices [35], [36]. The WECs using the mentioned PTOs are generally quite large.

Another WEC type, which has a smaller size compared with the aforementioned WECs is the Archimedes wave swing (AWS). AWS is a submerged hydraulic device that has an air filled chamber with a floater, which resembles a buoy, that moves vertically with the coming waves. The power takeoff of the AWS is a direct drive and a case study regarding a full scale prototype is presented in [37]. In [38] and [39], the design of the linear generator and a comparison between the conventional and the transverse flux permanent magnet linear generators are shown. A wave park of AWS is discussed in [40].

The type of WEC that is used in this project is a single point absorber, which is a relatively compact and simple system that can harness a substantial amount of energy. There are many studies regarding the point absorbers, however many of them include a direct drive linear generator. One of the few commercial wave parks, Seabased, uses point absorbers and it is located outside Lysekil, Sweden. This wave park consists of 36 WECs with an installed capacity of 3 MW [41], where each WEC has a buoy and a linear PM generator for the electric generation. [42], [13], [43] and [44] present detailed analyses on the Seabased technology.

2.2 Wave Description

2.2.1 Linear Wave Theory

Linear, or Airy wave theory is the linearized description of the propagation of the ocean waves that occur on the homogenous water surface. In linear wave theory, ocean waves are considered to be sinusoidal waves that have a single frequency. Furthermore the linear theory assumes that the wave amplitude is small compared to the wave length and the slope of the free surface is neglected [45]. These assumptions are reasonable when analyzing moderate sea states at deep water conditions, however linear theory cannot be used when analyzing extreme sea states or shallow water conditions since the aforementioned simplifications lead to inaccuracy.

Single frequency sinusoidal waves are named regular waves and are defined using a set of parameters. Figure 2.1 shows a basic representation of regular waves.

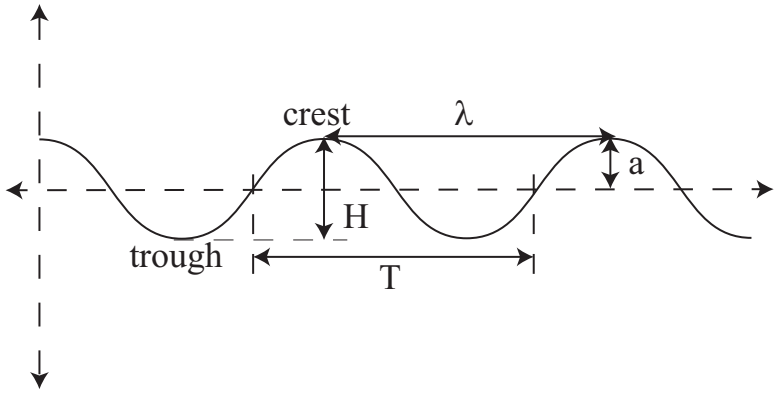

Figure 2.1: Regular wave representation

Here, λ represents the horizontal distance between two following wave crests and is called the wave length. The point where the wave has the maximum upward displacement within a cycle is called a wave crest and the opposite is the wave trough. The wave period, T, is the time during which the wave completes one full oscillation. The wave height, H, is defined as the vertical distance from crest to trough, whereas the wave amplitude, a, is the height between the mean water surface to the wave crest, as seen in the figure.

The free surface wave elevation above the static water level, η, for a single frequency regular wave is described as,

$$\eta = a\cos(\omega t - kx + \epsilon) \tag{2.1}$$

where, k is the wave number, ω is the angular frequency in rad/s, x is the position on the x-axis in m at time t, ϵ is the phase shift rad and a is

$$a = \frac{H}{2} \tag{2.2}$$

The angular frequency of the wave is

$$\omega = \frac{2\pi}{T} = 2\pi f \tag{2.3}$$

where f is the cyclic frequency of the wave. The number of radians per unit distance, also known as the wave number, k, is

$$k = \frac{2\pi}{\lambda} \tag{2.4}$$

The wave celerity that linear waves propagate with is

$$C = \frac{gT}{2\pi} \tanh(\frac{2\pi d}{\lambda}) \tag{2.5}$$

where g is the gravitational acceleration in kgm/s and d is the water depth [46].

The real ocean waves are random, however they can be represented as several linearized regular waves. The individual regular waves can be studied using linear wave theory and the overall effect is the linear summation of these individual calculations. Important wave parameters of the random ocean waves such as free surface elevation, position, velocity and acceleration can be determined using this method.

2.2.2 Irregular Waves

In reality, waves in the oceans and seas are not repeating sinusoids with infinitely long crests, but rather random oscillations. Waves that are containing several frequencies and amplitudes are called irregular waves. Figure 2.2 shows the general representation of irregular waves.

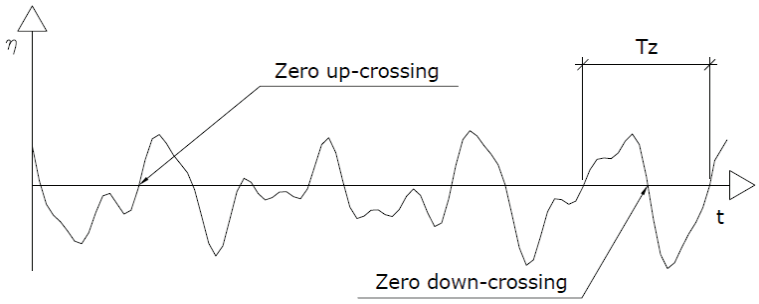

Figure 2.2: Irregular wave representation

The wave height is the difference between the highest crest and the lowest trough in a wave; the wave length is the distance between the zero-crossings and the period is the time interval

between them. Since an irregular sea-state contains several wave lengths, heights and periods, it is not possible to fully model it analytically using only a single wave height and period, as in the case of regular waves. However, it is possible to characterise the severity of a sea-state using empiric parameters. These parameters are significant wave height, H_s and mean wave period, T_z. Significant wave height is the average of the highest third of the recorded waves and mean wave period is the average period. In order to determine the most common sea states, i.e. significant wave heights and mean wave periods, of a given location, observations are to be collected over several years. The diagram that shows the significant wave heights and mean wave periods occurring at a given location and the probability of occurrence of each combination is called a scatter diagram.

Irregular waves cannot be analyzed with ease, however they can be broken down into several regular waves, which can be analyzed using linear theory. The wave height, wave period and the phase shift of the irregular wave can be estimated through Fourier analysis. The Fourier series, resulting from the analysis of the wave records can be illustrated graphically as amplitude and phase spectra.

The Pierson - Moskowitz (PM) spectrum is the fundamental spectrum for a fully developed sea, when a constant wind blowing for infinitely long time, therefore the energy transfer is balanced by dissipation, however the energy of the wave remains constant. The Pierson - Moskowitz spectrum is described only by the wind speed, i.e a one-parameter spectrum. It is represented as,

$$S_{PM}(\omega) = \alpha g^2 \omega^{-5} e^{-0.74(\frac{\omega_o}{\omega})^4} \tag{2.6}$$

where, α is the Phillips constant and is equal to 0.0081, $U_{19.5}$ is the wind speed that occurs 19.5 m above the water surface and ω_o is

$$\omega_o = \frac{g}{U_{19.5}} \tag{2.7}$$

The Pierson - Moskowitz Spectrum however cannot be used to reproduce a realistic spectrum of a developing sea, therefore a multi-parameter spectrum is to be used, which is called the Joint North Sea Wave Project (JONSWAP) spectrum. This spectrum is similar to the PM spectrum however a peak enhancement factor is added in order to better fit the collected North Sea measurements. JONSWAP spectrum is described as [46]

$$S_{JONSWAP}(\omega) = \alpha g^2 \omega^{-5} e^{-1.25(\frac{\omega_m}{\omega})^4} \gamma^{e^{-\frac{1}{2}(\frac{\omega-\omega_m}{\sigma\omega_m})^2}} \tag{2.8}$$

where $\gamma^{e^{-\frac{1}{2}(\frac{\omega-\omega_m}{\sigma\omega_m})^2}}$ is the shape parameter. ω_m is the modal angular frequency, which is the maximum frequency of the spectrum and is

$$\omega_m = 22(\frac{g^2}{U_{10}F})^{\frac{1}{3}} \tag{2.9}$$

where U_{10} is the wind speed at 10 m above the water surface and F is the distance over which the wind blows with constant speed and is named fetch and α is

$$\alpha = 0.076(\frac{U_{10}^2}{Fg})^{0.22} \tag{2.10}$$

σ is a spectral width parameter and is

$$\sigma = \begin{cases} 0.07, & \text{if } \omega \leq \omega_m \\ 0.09, & \text{if } \omega > \omega_m \end{cases}$$

Figure 2.3 shows the Pierson - Moskowitz and JONSWAP spectra using the same H_s.

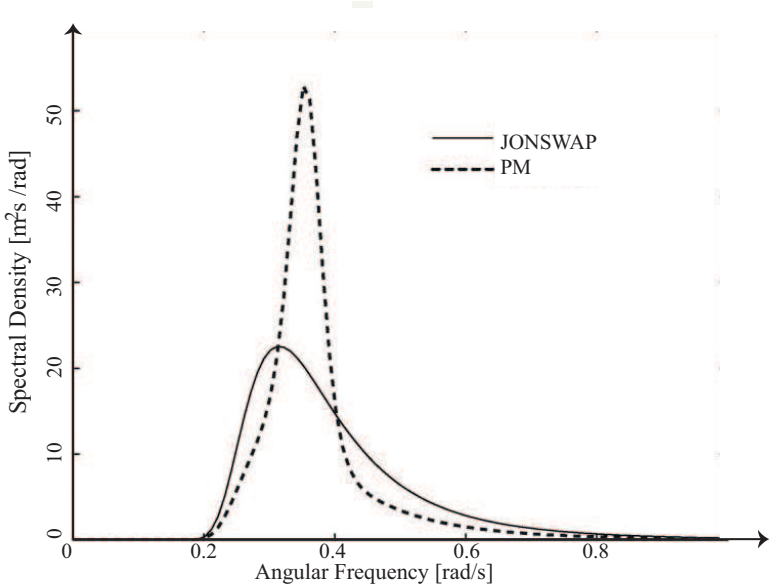

Figure 2.3: Pierson - Moskowitz and JONSWAP Spectra with the same significant wave height

It can be seen that the peak in the JONSWAP spectrum is much more prominent than the PM spectrum, due to the peak enhancement factor applied in order to achieve the JONSWAP relation. The JONSWAP spectrum represents a sea state that never reaches the fully developed state, therefore it is better suited for developing seas, such as the North Sea.

For practicality, wave analysis can be defined as a function of frequency instead of angular frequency, as well as by using the sea state parameters rather than wind speed and fetch. Accordingly, the JONSWAP spectrum can be described based on the significant wave height, H_s and the peak period, T_p, as,

$$S_{JONSWAP}(f) = \frac{H_s^2 f_p^4}{B} f^{-5} e^{-1.25(\frac{f}{f_p})^{-4}} \gamma^{e^{\frac{0.5(\frac{f}{f_p}-1)^2}{\sigma^2}}} \tag{2.11}$$

where, f_p is the peak frequency of the sea state and is equal to $1/T_p$ [47]. B is

$$B = 16(0.06533\gamma^{0.8015} + 0.13467) \tag{2.12}$$

The shape factor, γ, is 3.3 for oceans and large seas and is 1 for smaller seas [48].

The average wave power per unit wave front for irregular waves is

$$P_{wave} = \rho g \int_0^\infty C_g(f) S(f) df \tag{2.13}$$

where, ρ is the water density and C_g is the group celerity. The equation for deep waters, which is generally where the point absorbers are located becomes

$$P_{wave} = \frac{\rho g T_e H_s^2}{64\pi} \tag{2.14}$$

and T_e, the energy period is

$$T_e \approx 1.162 T_z \tag{2.15}$$

where T_z is the mean wave period.

2.3 Equation of Motion of the Single Point Absorber

When a rigid floating body is placed in water, there are six possible motions that can occur, which are commonly referred as the six degrees of freedom. In the three dimensional plane, a linear and a rotational motions is possible on each axes. The linear motions on the x,y and z axes are surge, sway and heave respectively. Similarly the rotational motion on the x axis is called roll, on the y axis it is pitch and on the z axis direction is named yaw. Figure 2.4 shows the six degrees of freedom on a floating body.

Here, the center of buoyancy is the center of the submerged volume of the floating body. For wave energy applications, it is common to assume that a point absorber only moves in the heave direction. Figure 2.5 shows a representation of the mechanical system of a floating object in heave.

It can be seen that the floating object is a mass-spring-damper system. Not unlike an electrical RLC circuit representation, the mass represents the inertia of the system resisting the change of current state, the damper dissipates the energy and the hydrostatic stiffness stores an energy based on the displacement. The mass-spring-damper system can be represented as

$$(M + A)\ddot{\xi}(t) + B\dot{\xi}(t) + C\xi(t) = F(t) \tag{2.16}$$

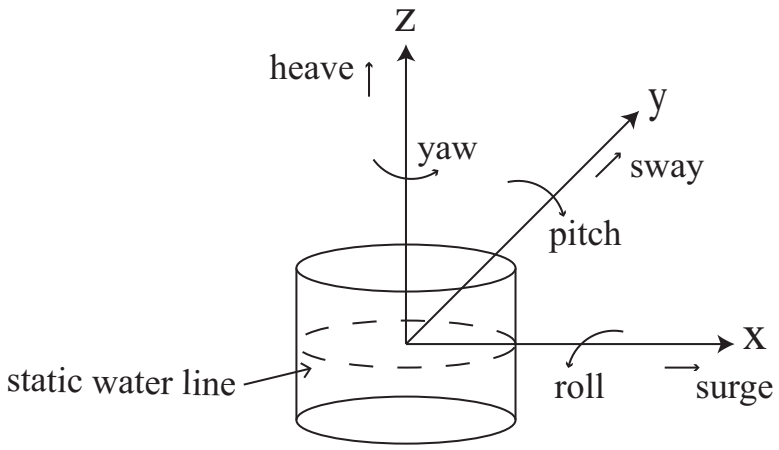

Figure 2.4: The six degrees of freedom of a rigid floating body

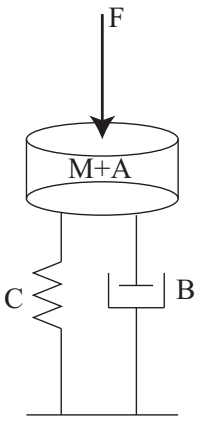

Figure 2.5: Mechanical representation of a floating body for the heave motion

where M is the mass of the body, A is the added mass, B is the radiation damping coefficient, C is the hydrostatic stiffness and F is the total of the wave induced forces. ξ is the displacement, therefore $\dot{\xi}$ is the velocity and $\ddot{\xi}$ is the acceleration of the body. The total wave induced force is

$$F(t) = \eta c_w \cos(\omega t + \theta_w) \tag{2.17}$$

where c_w is the wave force coefficients and θ_w is the phase shift between the wave elevation and the wave induced forces.

A, B and c_w represent the hydrodynamic effects on the floating body due to the oscillating motion of the body and the water, therefore these parameters are dependent on the oscillating frequency as well as the geometry of the floating object. For very basic geometries, there are analytical solutions for determining these parameters, however they are usually determined through experimentation or simulation. On the other hand, M and C only depend on the geometry of the body and are therefore independent of the frequency. The hydrostatic stiffness, C, is

$$C = \rho g A_b \tag{2.18}$$

here, A_b is the area of the floating body.

The motion of the floating body, using the equation of motion is to be sinusoidal and the frequency of the motion is equal to the wave frequency. Accordingly, the displacement of the body is

$$\xi(t) = \hat{\xi}\cos(\omega t + \phi) \tag{2.19}$$

where $\hat{\xi}$ is the amplitude of the displacement and ϕ is the phase shift between the incoming wave and the displacement. Using derivation, the velocity and the acceleration of the body can be calculated as

$$\dot{\xi}(t) = \upsilon(t) = -\omega\hat{\xi}\sin(\omega t + \phi) \tag{2.20}$$

$$\ddot{\xi}(t) = -\omega^2\hat{\xi}\cos(\omega t + \phi) \tag{2.21}$$

Additional external forces that are linear can be added in (2.16), such as the power extraction force of the electric generator for WEC applications. Note that the equation of motion is only valid for single frequency sinusoidal oscillations.

2.4 Electric Power Extraction

The electric generator that is coupled to the point absorber introduces a force that has the same frequency as the buoy movement. The power extraction force is

$$F_p(t) = -R_p\dot{\xi}(t) = -R_p\upsilon \tag{2.22}$$

where R_p is the power extraction coefficient and is dependent on the electric generator. The extracted power simply becomes

$$P_p(t) = F_p(t)\upsilon(t) = R_p\upsilon^2(t) \tag{2.23}$$

Chapter 3

The Electric Drive System

3.1 Electromagnetic Theory

This chapter explains the electromagnetic background necessary to explain the operation principles of a permanent magnet machine. Ampere's Law dictates the relation between the magnetic field and the enclosed current and is represented as

$$\oint Hdl = \int\int JdS = I_{enclosed} \tag{3.1}$$

where H is the field intensity in A/m, dl is the differential length in meters. J is the current density. Here, the magnetic flux density is related to the magnetic field intensity as

$$B = \mu H \tag{3.2}$$

μ is the permeability of the material and defined as

$$\mu = \mu_0 \mu_r \tag{3.3}$$

where μ_0 is the permeability of free space and μ_r is the relative permeability. Relative permeability for air is approximately 1, whereas the iron material has a very high permeability, up to 10000. Due to this fact, the field intensity is much higher in the air gap, than it is in the iron core. Relative permeability varies strongly with the flux density and for very high flux levels it will go towards 1. In an electric machine which has a complicated iron geometry, the flux density will differ strongly with regards to the geometry, as well as the relative permeability of the material. Observe that the relative permeability is a function of the flux. This makes analytical calculations for an electric machine quite complicated. Therefore, typically for machine analysis, Finite Element Method (FEM) calculations are used. An important quantity is the total flux linkage and it is related to the flux according to

$$\Psi = N\Phi_c \tag{3.4}$$

Φ_c is the flux in the coil and Ψ represents the total flux linkage. The flux linkage is related to the induced voltage in the coil as

$$e = -\frac{d\Psi}{dt} \tag{3.5}$$

where e is the electromotive force (emf). This means that the induced emf in a closed circuit is equal to the negative value of the time derivative of the enclosed magnetic flux and is called Faradays Law of Induction. The inductance of the electromagnetic circuit is formulated as

$$L = \frac{\Psi}{I} \tag{3.6}$$

The winding can be represented as a resistance and an inductance, which causes a voltage drop over it. The current-voltage relation can be calculated as

$$v = L\frac{di}{dt} + Ri \tag{3.7}$$

where R is the resistance of the wire. The current-voltage relation now becomes

$$v = L\frac{di}{dt} + Ri + \omega_r \Psi_m cos(\omega_r t) \tag{3.8}$$

where Ψ_m is the flux linkage of the magnet and ω_r is the angular speed of the magnet rotation. This voltage expression can be applied to any kind of electrical machine based on the corresponding topography and is usually the basis for analyzing an electrical machine.

In this work, permanent magnet machines are predominantly used. Figure 3.1 shows a simplified representation of the permanent magnet generator.

Phase A, Phase B and Phase C lines show the magnetic axes for each stator current phase and they are oriented 120^o apart from each other. The winding of Phase A is schematically displayed in the figure, where the magnetic direction is dictated through the right hand rule. It is important to know that the coils typically have several turns and might also be distributed in more than one slot. The induced voltage outlet for the A phase, where (3.5) is applicable when the resistance is ignored, is depicted in the figure.

In order to simplify the three phase analysis of the generator, d-q transformation can be used. d-q transformation is a method which reduces the three AC quantities regarding each phase into two DC quantities, when the AC system is considered to be symmetrical. The flux linkage in the machine is represented in the d-q axis where the d-axis represents the direction of the magnet flux [49]. For no load operation, the d-axis flux linkage is the same as the magnet flux linkage, which also is the total flux linkage of the generator. However, for the loaded case, a flux linkage on the q-axis will be formed, which then contributes to a resulting total flux linkage together with the magnet flux linkage as well as the d-axis flux linkage component created by the d-axis current.

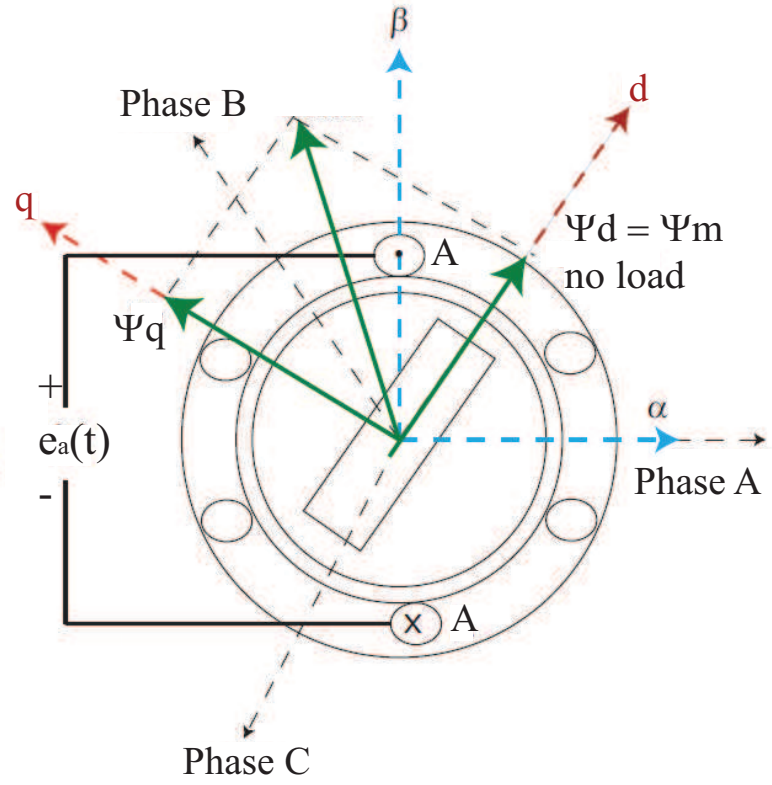

Figure 3.1: Simplified electromagnetic scheme of the permanent magnet machine. Direct and quadrature directions are displayed.

3.2 Permanent Magnet Machines

The permanent magnet (PM) machine rotor consists of permanent magnets for creating the rotor excitation. In a PM machine, the rotor losses are greatly lowered compared to those in an induction machine, due to the absence of windings in the rotor. The permanent magnets can be placed in several different ways and the permanent magnet machines can be divided into three categories based on the magnet placement. These are, the surface mounted permanent magnet(SMPM) if the magnets are fastened to the outer surface of the rotor, inset permanent magnet if the magnets are attached into the rotor surface and interior mounted permanent magnet (IPM) if the magnets are placed into ducts that are cut out off the rotor laminations. Figure 3.2 shows some of the different PM type designs [50].

The PM machine used in this work, which is also the most common variant for the kW level power applications, is a 3-phase machine operated with sinusoidal input current. The stator equations for the PM machine in d-q directions are

$$u_{sd} = R_s i_{sd} + L_{sd}\frac{di_{sd}}{dt} - \omega_r L_{sq} i_{sq} \tag{3.9}$$

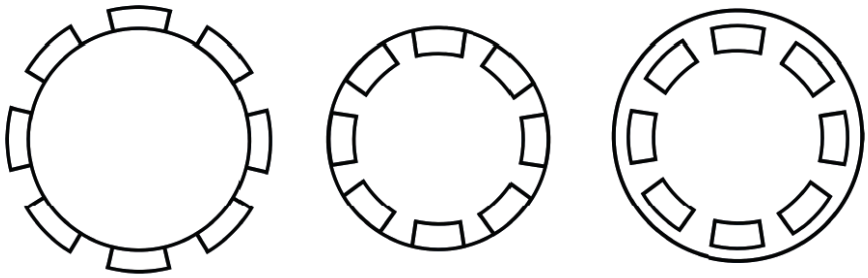

Figure 3.2: Three types of the permanent magnet machines, surface mounted, inset and interior permanent magnet machines respectively.

$$u_{sq} = R_s i_{sq} + L_{sq}\frac{di_{sq}}{dt} + \omega_r L_{sd} i_{sd} + \omega_r \Psi_m \tag{3.10}$$

where R_s is the stator resistance, L_{sd} and L_{sq} are the stator inductances in d and q directions, respectively. The initial value of Ψ_m can be determined by a no load test but it is dependent on the q-axis current and it is determined for various q-axis currents when the d-axis current is zero. Therefore, while performing the machine analysis it is represented as a function of the q-axis current. For a broader description, [51] can be studied. The magnet flux linkage decreases with increasing q-axis current due to saturation. The d and q axis inductances also vary, due to the same reason [51]. The current derivatives in (3.9) and (3.10) indicate electrical dynamics. However, since the mechanical system has a much longer time constant than the electrical ones, the electrical behaviour is considered to be in steady state onwards in this work. The steady state stator voltages thus become

$$u_{sd} = R_s i_{sd} - \omega_r L_{sq} i_{sq} \tag{3.11}$$

$$u_{sq} = R_s i_{sq} + \omega_r L_{sd} i_{sd} + \omega_r \Psi_m \tag{3.12}$$

The principle inductance determinations are shown in (3.6), so in order to calculate L_{sd} and L_{sq}, the flux linkages in the corresponding directions are to be obtained. Using measurements, analytical calculations for simplified cases or as in this work FEM calculations, the flux linkages in d and q directions can be determined for various operating points. The stator inductances in the d-q axis can be calculated as

$$L_{sd} = \frac{\Psi_d - \Psi_m}{i_{sd}} \tag{3.13}$$

$$L_{sq} = \frac{\Psi_q}{i_{sq}} \tag{3.14}$$

where Ψ_d and Ψ_q are the flux linkages in d and q directions.

The electromagnetic torque of the permanent magnet machine is

$$T_e = \frac{3n_p}{2}(\Psi_m i_{sq} + (L_{sd} - L_{sq})i_{sd}i_{sq}) \tag{3.15}$$

Here, n_p is the number of pole pairs. It can be observed that the electromagnetic torque depends on the magnet flux linkage as well as the machine parameters. For a better understanding, the electromagnetic torque can be divided in two parts that represents one dependency. It can be formulated as

$$T_e = T_m + T_r \tag{3.16}$$

where T_m represents the torque component that depends on the permanent magnet flux, is named magnet torque in this work. T_r is the torque component that is produced by the difference in reluctance of the d and q directions, and is called reluctance torque. The concept of reluctance is explained in coming section.

The magnet torque is

$$T_m = \frac{3n_p}{2}(\Psi_m i_{sq}) \tag{3.17}$$

and the reluctance torque is

$$T_r = \frac{3n_p}{2}(L_{sd} - L_{sq})i_{sd}i_{sq} \tag{3.18}$$

3.3 Reluctance - Inductance Relation and Concept of Saliency

It is mentioned before that three types of permanent magnet rotor topologies are considered in this work. The main difference between these is the machine reluctance ($\Re$). The magnetic reluctance of a uniform magnetic circuit is

$$\Re = \frac{l}{\mu_0 \mu_r A} \tag{3.19}$$

where l is the length of the reluctance path and A is the cross sectional area of the circuit. Figure 3.3 shows the d and q axis reluctance paths.

If the flux travels through different materials in series, the total reluctance is the sum of the individual reluctance values of these materials, as

$$\Re = \frac{l_1}{\mu_0 \mu_{r_1} A_1} + \frac{l_2}{\mu_0 \mu_{r_2} A_2} + ... + \frac{l_n}{\mu_0 \mu_{r_n} A_n} \tag{3.20}$$

It can be seen in Figure 3.3 that the magnetic flux travels through, ferromagnetic material (iron, electric steel or steel laminations), permanent magnets and air. The relative permeability

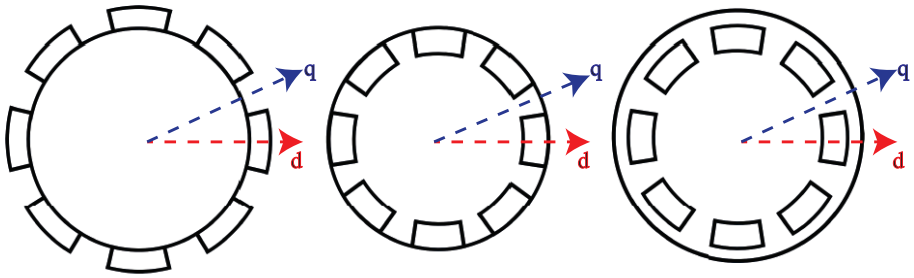

Figure 3.3: Direct and quadrature directions axes of the different type of permanent magnet machines .

of the permanent magnet is slightly above 1 and that of air is 1. The ferromagnetic materials typically have high relative permeability values, e.g. relative permeability of cobalt-iron is 18000, that of iron is 5000 and electrical steel is 4000. Since the cross sectional of the a rotational machine is uniform, the reluctance depends on the length of the magnetic circuit through different materials.

The d-axis of the SMPM machine forms over the rotor yoke, the permanent magnet over the magnet length and the airgap, until the flux reaches the stator. The q-axis flux travels through the same rotor length and an air pocket that is as long as the magnet length together with the airgap. Since both air and permanent magnet material has a μ_r of approximately 1, the resulting $\Re_d$ and $\Re_q$ values are equal for SMPM machines. For the inset and IPM machines this is not so, therefore $\Re_d$ and $\Re_q$ have different values. The machines that have different reluctance values in d and q axes paths are called salient machines, i.e. inset and IPM machines are salient and SMPM machine is non-salient. The inductance of any given axis is inversely related to the corresponding reluctance,

$$L \propto \frac{1}{\Re} \tag{3.21}$$

which means that the d and q axis inductances would be equal for a non-salient machine and vice versa. Due to (3.18), the reluctance torque is only present if the machine is salient.

3.4 PM Assisted Synchronous Reluctance Machine

The PM assited Synchronous Reluctance Machines (SRM) can be seen as a variant of the IPM machines with multi layer magnets or as a SRM machine that is fortified with permanent magnets, therefore they offer a good combination of the benefits of the high flux linkage supplied by the permanent magnets and the high reluctance torque of the reluctance machine design. The PM assisted SRM drives can be often found in electrical vehicle applications in the industry.

The PM assisted SRM has the same torque relation as the PM machines, as presented in the previous section, differing only regarding the value of the d and q inductances. The difference

between the d and q inductances for the PM assisted SRM is higher than the salient IPM and VPM designs, which causes a higher reluctance torque, based on (3.18), however the magnet torque is generally lower than the PM generators, due to the factors such increased leakage magnetic flux.

3.5 Machine Control Strategy

The torque required by the load can be achieved by many different current vectors, however for an energy efficient operation, a control strategy that provides low losses is preferable. One of the most common control strategies is called Maximum Torque per Ampere (MTPA), where the required torque is achieved with the shortest current vector, which minimizes the copper losses. The MTPA current vector can be expressed as

$$\vec{I} = I\angle\beta = i_{sd} + ji_{sq} \tag{3.22}$$

which means

$$i_{sd} = I\cos(\beta) \tag{3.23}$$

and

$$i_{sq} = I\sin(\beta) \tag{3.24}$$

where β is the MTPA angle. The torque relation for the permanent magnet generators is given in (3.15). The angle that maximizes the torque, i.e. the MTPA angle can be found analytically through

$$\frac{dT_e}{d\beta} = 0 \tag{3.25}$$

Equation (3.12) shows that the q-voltage is dependent on the angular speed and the magnet flux linkage, therefore the increasing speed causes an increase in the voltage. However the voltage increment is limited by the maximum converter voltage. Once the converter limit is reached, neither the voltage nor the current vector can be increased anymore. The speed where the voltage limit is reached, which is also where the maximum torque is achieved, is the rated speed of the generator. If the operating point demands speeds higher than the rated speed, the original MTPA strategy cannot be used anymore. To be able to operate at speeds higher than the rated speed where the voltage provided by the converter is not sufficient, the flux linkage in the machine is to be decreased according to (3.12). This is called the flux or field weakening. Figure 3.4 depicts a generic torque-speed relation for a drive system that is controlled using MTPA and Field weakening control. The solid line depicts the maximum operating trajectory. At low speeds, the maximum torque operation is achieved. For operating points with higher speeds than the rated, the maximum torque cannot be reached anymore, due to the decreased

flux linkage in order to cope with the available voltage level. The power is ideally constant in the field weakening operation, but this is rarely achieved in real operations.

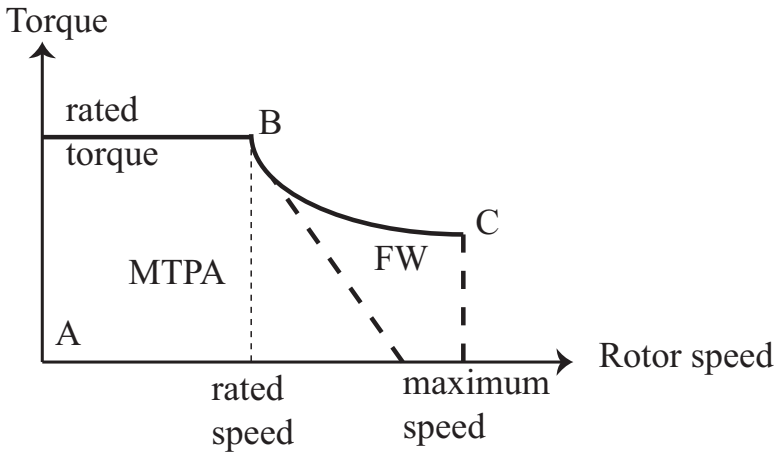

Figure 3.4: An example of torque-speed relation for the MTPA and Field Weakening Control.

Figure 3.5 shows an illustration of the current vector for a machine operation ranging from zero to the maximum speed for generator operation. The MTPA operation is between points A and B, and the field weakening operation is depicted between points B and C. The constant torque lines are specified with T and the number indicates the value, i.e T_1 is the lowest torque and T_5 is the highest. It can be observed that the lower torque values require lower currents and that the MTPA angle is low. With increasing torque, both the current and the current angle increase. Here, the current vector is constant in magnitude, therefore the increasing d-current causes the q-current to decrease, which leads to a reduced maximum torque, as can be seen from the figure. The voltage limit lines are indicated with U and they represent the maximum voltage values for a given speed. Here, the number indicates the rotor speed, meaning that U_1 is the voltage limit at the lowest speed and the speed increases with increasing number.

For a given torque value, the described current trajectory can be determined through a current minimization procedure using appropriate constraints. Here, the objective function defining the current vector is

$$f_0 = \sqrt{i_d^2 + i_q^2} \tag{3.26}$$

which is the function that is to be minimized. The machine control is valid as long as the machine voltage does not exceed the converter DC-link voltage, therefore it can be expressed as an inequality constraint,

$$(\sqrt{u_d^2 + u_q^2}) - \frac{V_{DC}}{\sqrt{3}} \leq 0 \tag{3.27}$$

To be able to solve the objective function for the desired torque, the electrodynamic torque of the machine needs to be equal to this torque reference, which is an equality constraint and can be expressed as

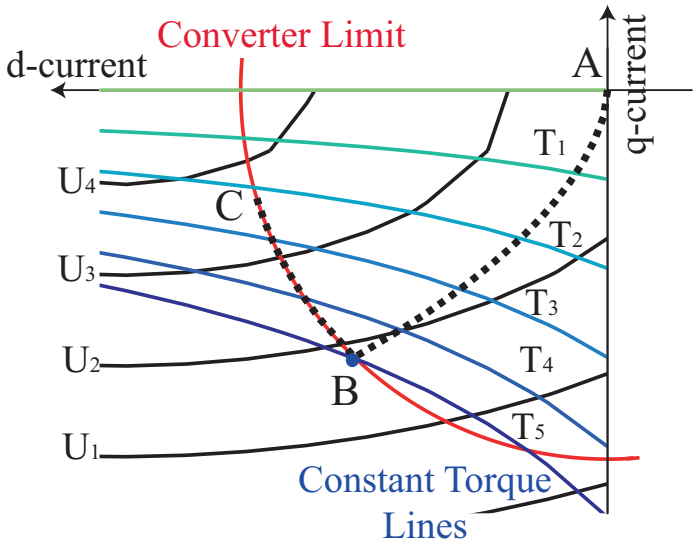

Figure 3.5: The current trajectory for the MTPA and Field Weakening Control.

$$\frac{3n_p}{2}(\Psi_m i_{sq} + (L_{sd} - L_{sq})i_{sd}i_{sq}) - T_{ref} = 0 \tag{3.28}$$

The resulting current vector for the whole operating region can thus be determined as

$$\text{minimize } f_0 \text{ for } \begin{cases} (\sqrt{u_d^2 + u_q^2}) - \frac{V_{DC}}{\sqrt{3}} & \leq 0 \\ \frac{3n_p}{2}(\Psi_m i_{sq} + (L_{sd} - L_{sq})i_{sd}i_{sq}) - T_{ref} & = 0 \end{cases}$$

In order to be able use this method, L_{sd}, L_{sq} and Ψ_m are to be determined. Ψ_m is a function of the q-axis current and is determined when the d-current is kept zero, as

$$\Psi_m(i_q) = \Psi_d(i_q) \tag{3.29}$$

Ψ_d is the flux on the d-direction. The inductance, as seen in (3.6), is the ratio between the flux linkage and the current. The d-axis inductance is therefore expressed as

$$L_{sd}(i_d, i_q) = \frac{\Psi_d(i_d, i_q) - \Psi_m(i_q)}{i_d} \tag{3.30}$$

since the magnet flux is aligned with the d-axis of the machine in this work. Similarly, the q-axis inductance is

$$L_{sq}(i_d, i_q) = \frac{\Psi_q(i_d, i_q)}{i_q} \tag{3.31}$$

3.6 Winding Placement and resistance calculation

Figure 3.6 depicts an illustration of the machine cross section and the d and q axes and the windings for two poles. The machine depicted here has double layer windings, as the stator considered in this project. The d and q axes are selected as shown in the figure and the angle between them is 90^o electrical.

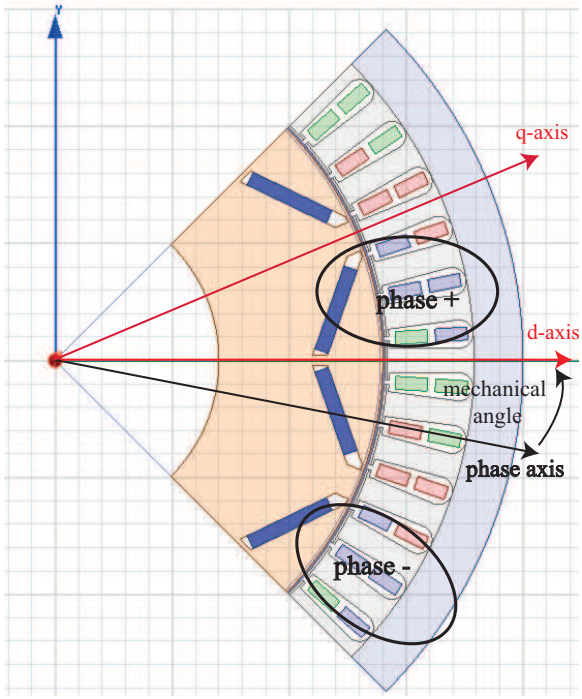

Figure 3.6: d-axis, q-axis and the phase axis depicted on the machine cross section.

The three phase axis lies between the positive and the negative coils of the same phase. One important issue for FEM calculations is to align the reference phase axis with one of the magnetic axes at the start of the simulation. In this example, the depicted phase is the reference axis and in order to align the d-axis to the reference, an initial mechanical angle is to be considered, which would mechanically align the rotor to a common electrical reference axis.

The phase sequence is generally a-b-c for the electric drive applications and the currents are set as

$$i_a = \hat{I}\cos(\omega t + \beta) \tag{3.32}$$

$$i_b = \hat{I}\cos(\omega t + \beta - \frac{2\pi}{3}) \tag{3.33}$$

$$i_c = \hat{I}\cos(\omega t + \beta + \frac{2\pi}{3}) \tag{3.34}$$

The current density, J, is

$$J = \frac{I}{S_c} \tag{3.35}$$

where S_c is the cross sectional area of the conductor and is

$$S_c = \frac{S_{coil}}{N} \tag{3.36}$$

where S_{coil} is the cross sectional area of the coil and N is the number of turns. Note that the area considered here is solely that of the copper material and the fill factor is to be considered if the stator slot area is more available for calculating the area of the conductor. A typical fill factor for an electrical machine with round wire windings ranges approximately between 40 - 50 %.

The rated current of the application is determined using a suitable current density value. For example, the current density for large machines with insignificant air circulation is roughly $4\ A/mm^2$, whereas it rises to $6\ A/mm^2$ for air cooled systems. The current density value increases for the forced cooled application and a lower current density is advised for compact designs. Appropriate selection of the rated current is of great concern, since the resistive losses manifest themselves as temperature increase and are quadratically proportional to the current. The resistive losses are

$$P_{resistive} = RI^2 \tag{3.37}$$

and the general expression of the resistance is,

$$R = \rho_{cu}\frac{l}{S_c} \tag{3.38}$$

where ρ_{cu} is the electrical resistivity (Ωm) and l is the conductor length. The electrical resistivity the copper is usually given for 20^oC and it is a temperature dependent parameter. The resistivity for any given temperature is

$$R_T = \rho_0[1 + \alpha(T - T_0)] \tag{3.39}$$

where, T is the present temperature, T_0 is the reference temperature (as mentioned usually 20^oC), ρ_0 is the resistivity at the reference temperature and α is the temperature coefficient.

Applying the general expression to the electrical machine, the resistance of the conductor becomes

$$R = \rho_{cu}\frac{2N(l_a + l_{ew})}{N_{pb}S_c} \tag{3.40}$$

where l_a is the active length, which is double the machine length, l_{ew} is the total length of the end windings for one conductor and N_{pb} is number of parallel branches. The length of the end winding can be determined as

$$l_{ew} = 2(l_{pitch} + l_{overhang}) \tag{3.41}$$

where l_{pitch} is the winding pitch, which is the length of the phase arc between the two points where it leaves and enters the machine frame. $l_{overhang}$ is the axial overhang, due to the needed bending of the end windings.

3.7 Two Level Inverter

Two level inverters are widely used for machine control. As it can be observed from Fig. 3.7, the inverter has six semiconductor switches and a diode in anti-parallel for each switch, with a DC-link voltage of V_{DC}. The current will flow through the anti-parallel diode when the switch oriented in the direction of the current is blocked. Each two switches, together with the anti-parallel diodes form a phase leg. The converter is typically controlled through pulse width modulation. To obtain the switching pattern, one method is to use voltage references that are compared with a carrier wave, which typically is a triangular signal. The upper switch is turned on when the reference is higher than the carrier wave for the corresponding phase and vice versa.

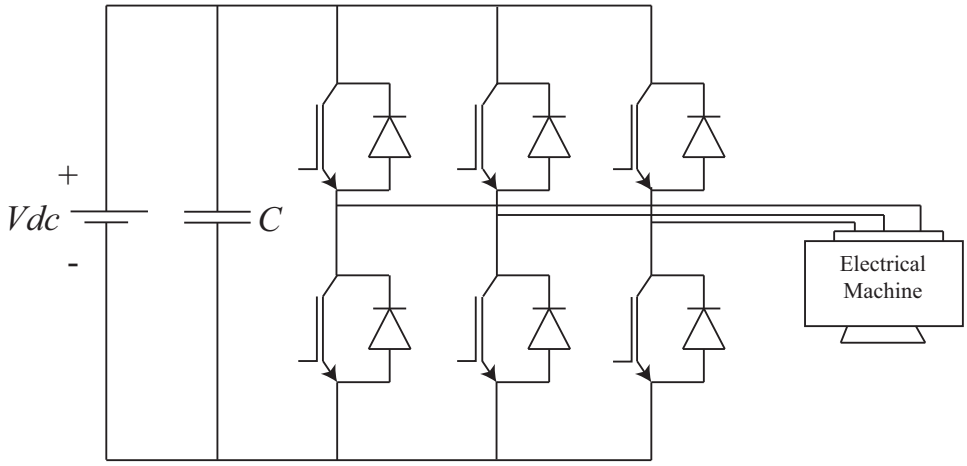

Figure 3.7: Topology of the two level inverter.

In order to utilize the DC-link voltage more effectively, the zero sequence signal injection method can be used. Addition of the zero sequence signal does not affect the machine operation, since the machine neutral point is not connected so that the line to line voltages remain sinusoidal. Using this method, the reference voltage signal is altered from the sine-wave. Here, the zero sequence method using the odd multiples of the third harmonics is used as a default. Fig. 3.8 shows the PWM modulation with zero sequence method, using the same line to line voltage magnitude. Another strategy of achieving the same voltage output is Space Vector Modulation.

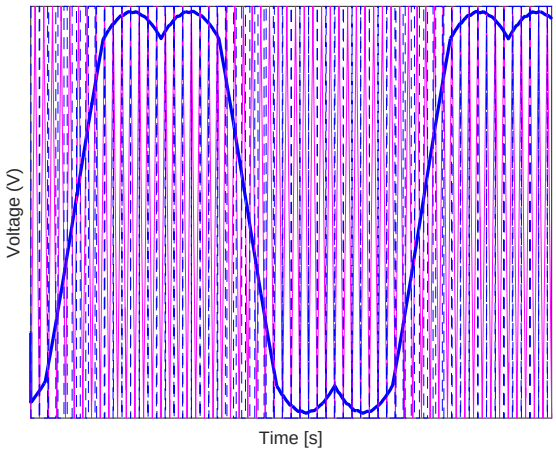

Figure 3.8: PWM modulation waveforms using zero sequence signal injection method.

The required DC-link voltage is

$$V_{DC} = \frac{\sqrt{3}\hat{V_{ph}}}{0.95} \tag{3.42}$$

which is approximately 15% higher than the traditional pure sinusoidal reference voltage modulation. 0.95 is a factor that adds a control margin and compensates for the effects of blanking time, minimum on and off times of the switches and the voltage drop in the modules.

There are several semiconductor component options that can be used as the switches of the power electronic converter. One of the most common semiconductor switches is the IGBT. The conduction loss for a single IGBT switch is

$$P_{cond_{IGBT}} = (\frac{1}{2\pi} + (\frac{M\cos(\varphi)}{8}))V_T\hat{I_1} + (\frac{1}{8} + (\frac{M\cos(\varphi)}{3\pi}) - \frac{\frac{1}{6}\cos(3\varphi)}{15})R_T\hat{(I_1)^2} \tag{3.43}$$

where $\cos\varphi$ is the displacement power factor, V_T is the offset voltage of the switch and R_T is the internal resistance. $\hat{I_1}$ is the peak current. Here, $1/6$ represents the magnitude of the third harmonic signal. M is the modulation index and is defined as

$$M = \frac{\hat{U_{max}}}{V_{DC}} \tag{3.44}$$

Here, $\hat{U_{max}}$ is the peak line-to-line voltage. The switching loss of a single IGBT is

$$P_{sw_{IGBT}} = f_{sw}(E_{on_{IGBT}} + E_{off_{IGBT}})(\frac{1}{\pi}\frac{\hat{I_1}}{I_{ref}})^{k_i}(\frac{V_{DC}}{V_{ref}})^{k_v} \tag{3.45}$$

where f_{sw} is the switching frequency, k_i and k_v are exponents of the current and voltage dependency of the switching losses and are selected to be 1 and 1.35 respectively [52]. $E_{on_{IGBT}}$ is the on state losses and $E_{off_{IGBT}}$ are the off-state losses. I_{ref} and V_{ref} are the reference current and voltage in which the switching loss data is given. The conduction loss of a single diode is

$$P_{cond_D} = (\frac{1}{2\pi} + (\frac{M\cos(\varphi)}{8}))V_{F0}\hat{I_1} + (\frac{1}{8} - (\frac{M\cos(\varphi)}{3\pi}) + \frac{\frac{1}{6}\cos(3\varphi)}{15})R_F\hat{(I_1)}^2 \tag{3.46}$$

where V_{F0} is the constant forward voltage drop and R_F is the internal resistance of the diode, i.e the forward voltage drop of the diode is

$$V_F = V_{F0} + R_F I(t) \tag{3.47}$$

The diode switching loss is

$$P_{sw_D} = f_{sw}(E_{sw_D})(\frac{1}{\pi}\frac{\hat{I}_1}{I_{ref}})^{k_i}(\frac{V_{DC}}{V_{ref}})^{k_v} \tag{3.48}$$

Here, E_{sw_D} is the diode switching energy loss, k_i is 1 and k_v is 0.6 [52]. It is to be noted that all loss components are defined based on the zero sequence injection method, as in [53].

Another semiconductor switch option is the Sic MOSFET. The MOSFET based converters tend to have lower losses than the IGBT based ones, furthermore the diode switching losses for the MOSFET converter are zero. The SiC MOSFET losses can be calculated using (3.43), 3.45 and 3.46, however the reverse conduction of the SiC MOSFET switches are not considered.

Compensating for the reverse conduction, the MOSFET conduction losses for one switch are

$$\begin{aligned} P_{c,MOS} = {} & \frac{R_T}{4\pi}\hat{I}^2((1-2t_{bl}f_{sw})(\pi/2+\beta-\frac{sin\beta}{2}) + 2Mcos\varphi(cos\beta-\frac{cos^3\beta}{3}))+ \\ & \frac{R_T}{4\pi(R_T+R_{F0})^2}[R_{F0}^2\hat{I}^2((1-2t_{bl}f_{sw})(\pi/2+\beta-\frac{sin\beta}{2}) - 2Mcos\varphi(cos\beta-\frac{cos^3\beta}{3}))+ \\ & V_{F0}^2((\pi-2\beta)(1-2t_{bl}f_{sw})-2Mcos\varphi cos\beta)+2R_d\hat{I}V_d(2cos\beta(1-2t_{bl}f_{sw})-Mcos\varphi(\pi/2+\beta-\frac{sin\beta}{2}) \end{aligned} \tag{3.49}$$

and the diode conduction losses for one diode are

$$P_{c,MOS} = \frac{R_{F0}}{4\pi(R_T+R_d)^2}(\hat{I}^2R_T^2(\pi/2-\beta+\frac{sin\beta}{2}-2Mcos\varphi(cos\beta-\frac{cos^3\beta}{3}))+$$
$$V_{F0}^2(\pi-2\beta-2Mcos\varphi cos\beta)-2\hat{I}R_TV_{F0}(2cos\beta-Mcos\varphi(\pi/2-\beta+\frac{sin\beta}{2})))-$$
$$\frac{V_{F0}}{4\pi(R_T+R_{F0})}(M\hat{I}R_Tcos\varphi(\pi/2-\beta+\frac{sin\beta}{2})+2R_T\hat{I}cos\beta-V_{F0}(\pi-2\beta)+2V_{F0}Mcos\varphi cos\beta)+$$
$$t_{bl}f_{sw}\hat{I}(R_{F0}\hat{I}/2+2V_{F0}/\pi) \quad (3.50)$$

where R_T, R_{F0} and V_{F0} represents the same parameters as for IGBT loss calculation expressions. t_{bl} is the blanking time and φ is the angle of displacement power factor. β is the parallel conduction angle and is

$$\sin\beta = \frac{V_{F0}}{R_T\hat{I}} \quad (3.51)$$

In the case of third harmonic injection, the following statement is to be added to (3.49) in order to compensate for non-sinusoidal phase voltage control

$$-\frac{MR_T\hat{I}^2}{60\pi}cos3\varphi(4sin^4\beta cos\beta+cos\beta-\frac{cos^3\beta}{3})(\frac{R_{F0}^2}{(R_t+R_{F0})^2}-1)-$$
$$\frac{MR_T\hat{I}R_{F0}V_{F0}}{24\pi(R_T+R_{F0})^2}cos3\varphi(\frac{sin4\beta}{2}-sin2\beta)-\frac{MR_TV_{F0}^2}{36\pi(R_t+R_{F0})^2}cos3\varphi cos3\beta \quad (3.52)$$

and

$$-\frac{MR_T\hat{I}V_{F0}}{96\pi(R_T+R_{F0})}(cos\varphi(2sin2\varphi cos2\beta-sin4\varphi cos4\beta)-sin\varphi(2sin2\varphi cos2\beta+sin4\varphi cos4\beta)+$$
$$\frac{MV_{F0}^2}{36\pi(R_T+R_{F0})}cos3\varphi cos3\beta \quad (3.53)$$

is to be added to (3.50). It is important to note that these expressions compensate for the reverse conduction of the MOSFET components, as well as the zero sequence signal injection method, as shown in [54].

3.8 Life Cycle Cost Determination

The life cycle cost is the discounted cost of an application over the life time. The life cycle cost of the losses of the WEC system is expressed as

$$LCC_{loss} = NPVL + C_i \tag{3.54}$$

where $NPVL$ is the net present value of energy losses and C_i is the investment cost. The investment cost realistically includes purchase, acquisitions and construction costs. In this work, the investment cost only includes the machine construction costs, i.e the cost of the material and manufacturing. The investment cost used in this project is expressed as

$$C_i = \sum m_m \rho_m + C_{manufacturing} \tag{3.55}$$

where m_m is the material weight, ρ_m is the material price and $C_{manufacturing}$ is the manufacturing cost. The NPVL is

$$NPVL = \sum_{n=1}^{t} \frac{R_t}{(1+r)^t} \tag{3.56}$$

where R_t is the net cash outflow, r is the discount rate and t is the life time. The net cash outflow is

$$R_t = W \rho_{el} \tag{3.57}$$

where W is the total annual energy loss and ρ_{el} is the electricity price per MWh.

A common approach for economical evaluation of electric power generation is the levelized cost of energy (LCoE). The LCoE is the average total cost to build and operate a power generating unit over a life time per unit produced energy, i.e it is expressed as the cost per MWh energy. This is particularly useful when assessing a power generating unit, since the LCoE of the unit can be compared to the energy price, meaning that the LCoE is the minimum price to sell energy in order to break even. However, in order to have a reasonable assessment many factors such as the investment cost of the whole plant, operation and maintenance costs, cost of the grid connection components must be known.

Chapter 4

Point Absorber Simulation Setup

4.1 Wave Availability and Single Point Absorber Simulation

4.1.1 Determining the Available Energy

Theoretically, in order to determine the available wave energy, the wave heights and periods must be known. These parameters are not obtained in a straight forward manner for a real location, since the ocean waves are irregular. An ocean wave consists of various sinusoidal components that have different frequencies and amplitude values. However, the sea-state characteristics can be determined empirically, using statistical parameters that are, significant wave height, H_s and mean wave period, T_z. Sea-state data is collected over several years in order to determine the range of the most common waves and how often they occur. The statistical data of the most common H_s and T_z combinations and their respective probability of occurrences can be represented in a, so called, scatter diagram. The scatter diagram considered in this work is presented in Table 4.1 and it is assumed that it represents a typical location in the North Sea.

It can be seen that some combinations have very low probability of occurrence (many rounded to 0%) and will not impact the energy potential greatly. Figure 4.1 shows the probability occur-

TABLE 4.1: The considered scatter diagram based observations of the studied location at North sea.

Tz[s] / Hs [m]	3,75	4,25	4,75	5,25	5,75	6,25	6,75	7,25	7,75	8,25
0,75	0,00%	0,40%	1,20%	1,60%	1,10%	0,70%	0,20%	0,00%	0,00%	0,00%
1,25	0,10%	4,90%	5,70%	6,20%	4,60%	4,30%	1,20%	0,30%	0,00%	0,00%
1,75	0,00%	0,70%	6,10%	9,60%	7,30%	5,20%	2,20%	0,80%	0,10%	0,00%
2,25	0,00%	0,00%	0,10%	3,20%	6,70%	5,10%	1,60%	0,70%	0,30%	0,00%
2,75	0,00%	0,00%	0,00%	0,10%	2,40%	5,00%	1,10%	0,60%	0,20%	0,10%
3,25	0,00%	0,00%	0,00%	0,00%	0,10%	1,60%	1,70%	0,70%	0,60%	0,20%
3,75	0,00%	0,00%	0,00%	0,00%	0,00%	0,10%	0,90%	0,50%	0,30%	0,10%
4,25	0,00%	0,00%	0,00%	0,00%	0,00%	0,00%	0,00%	0,50%	0,30%	0,10%
4,75	0,00%	0,00%	0,00%	0,00%	0,00%	0,00%	0,00%	0,00%	0,30%	0,10%
5,25	0,00%	0,00%	0,00%	0,00%	0,00%	0,00%	0,00%	0,00%	0,00%	0,10%

rence of all sea-states. It can be seen that the probability of sea states that have H_s higher than 3.75 m to occur is very low. These sea states are depicted as grey in the scatter diagram as well. Due to the low probability of occurrence level of the aforementioned sea states, all significant wave heights over 3.75 meters are neglected in this work. The limit is shown as the white dashed line in Figure 4.1.

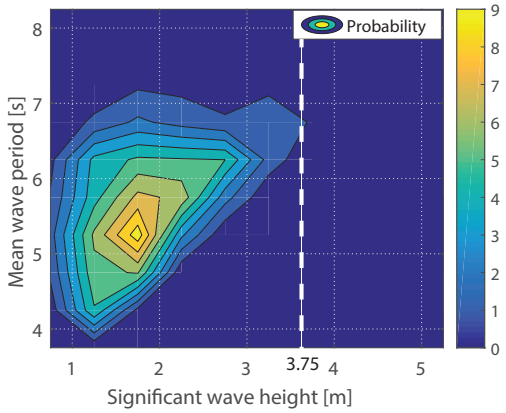

Figure 4.1: Probability of occurrence.

Figure 4.2 shows the cumulative wave energy distribution for the significant wave heights rows of the scatter diagram. The available wave energy is calculated using JONSWAP spectrum. It can be seen that by neglecting the wave heights over 3.75 meter, the average available wave energy is decreased less than 10%.

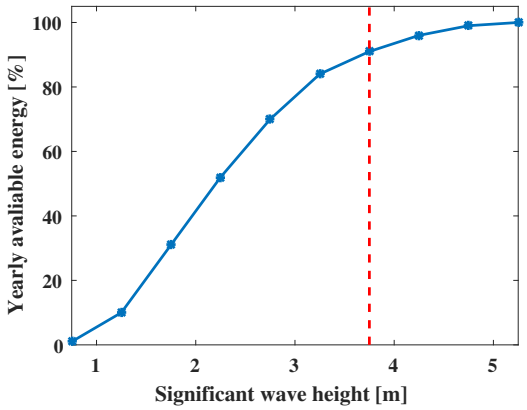

Figure 4.2: Wave energy distribution with relation to the significant wave height.

Fig. 4.3 shows the available wave power and wave energy per unit length. It can be observed that the power increases with increasing H_s and T_z. Furthermore, it is shown that the highest power areas do not correspond to the highest energy areas, since the waves with the highest powers have less than 1% probabilities of occurrence. Accordingly, an important issue is to find a trade-off between the sizing of the mechanical design and the energy capture. The WEC generation would be significantly oversized if it is designed to accommodate the highest power

TABLE 4.2: Properties of the wave energy converter

Diameter	$15m$
Height	$10m$
Draft	$4.5m$
Mass	$813386.9kg$
Displacement	$793.55m^3$
x-radius of gyration	$4.5m$
y-radius of gyration	$4.5m$
z-radius of gyration	$50m$
Centre of gravity - y position	$-0.7m$
Centre of buoyancy - y position	$-2.25m$
Water plane area	$176.34m^2$
Water plane inertia	$2474.65m^4$

wave, however using the most energetic wave as the design criteria might cause a drastic loss in energy capture.

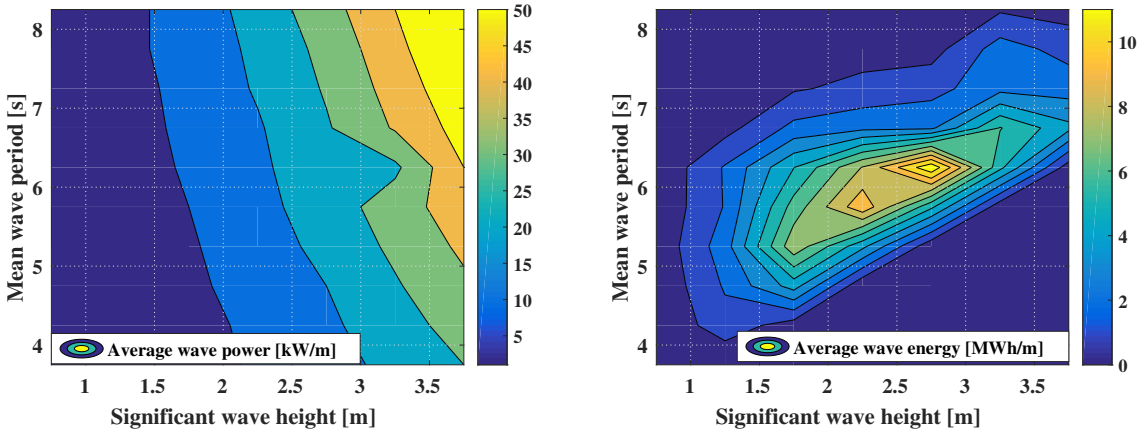

(a) Wave power

(b) Wave energy

Figure 4.3: Available wave power and energy per meter wave front.

4.2 Single Point Absorber WEC

Fig. 4.4 shows the general scheme of the single point absorber, which is a cylindrical buoy of $15\ m$ diameter and $10\ m$ height. At equilibrium $4.5\ m$ of the buoy height is submerged. The water depth is $50\ m$, therefore deep sea conditions can be used for calculations. Table 4.2 shows further properties of the buoy.

The electrical generation unit can be placed at the sea bottom or on a platform on the sea surface, however in this work the placement of the generation unit is not specified as it is assumed to have a negligible impact on the results.

Here, the buoy is considered to be an ideal cylinder and the viscous damping is neglected.

As seen in (2.16), in order to simulate the buoy motion one needs the frequency dependent hydrodynamic coefficients, namely added mass, radiation damping and the amplitude and phase

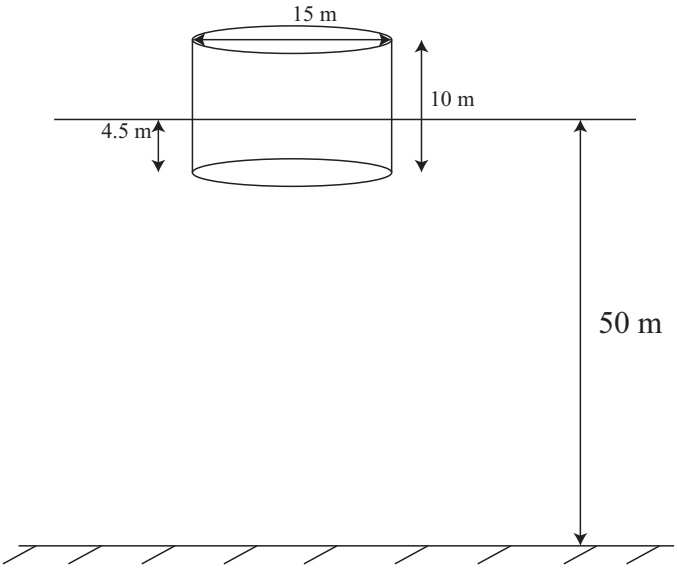

Figure 4.4: Buoy Shape and placement.

TABLE 4.3: Power extraction coefficient for different mean wave periods

Mean wave period [s]	3.75	4.25	4.75	5.25	5.75	6.25	6.75	7.25	7.75	8.25
Power extraction coefficient [kNs/m]	346	354.6	411.2	504.8	632.9	788.3	960.2	1139	1319	1497.6

of the wave excitation. These hydrodynamic coefficients are computed through Ansys AQWA, by guest researcher Dr. Guilherme Moura Paredes and can be seen in Appendix B.

The average extracted power and energy can be estimated through spectral analysis, however the peak extracted power can only be estimated through time domain simulations, therefore that is the preferred method to obtain the extracted power. The time domain simulations are performed using WEC-Sim 2.1, an open source MATLAB base toolbox.

According to (2.23), a power extraction coefficient is needed in order to determine the extracted power. The power extraction coefficient, R_p, can be optimized for each sea state or it can be a single value that maximizes the total extracted energy.

In order to determine an optimal R_p for each sea state, different R_p values are tried for power extraction calculation and the value that gives the maximum average power is selected, for each sea state. The yearly extracted energy while using the sea state optimized R_p method is higher than the single coefficient method, since the WEC has optimal performance at each sea state. However, this method requires a complex control algorithm since the power extraction coefficient needs to be tuned for each different sea state.

For determining the single R_p value, different R_p values are swept for the extracted average energy calculation and the R_p that maximizes the average extracted energy is selected. The single power coefficient method requires a simple control strategy, however, as mentioned, the average extracted energy will be lower than the tuned R_p strategy.

The single R_p value in this work is calculated to be $739.7\ kNs/m$. The sea state optimized R_p can be seen in Table 4.3.

Figure 4.5 shows the difference in the energies obtained using tuned and single R_p values, for different T_z values. It can be seen that the energy difference between the tuned and single R_p cases is fairly small. The total average extracted energy for a single R_p value is 478.5 MWh, and it is increased to 490.5 MWh if the tunable control is performed, which is an increase of 2.5%. The tunable control is not utilized in this work.

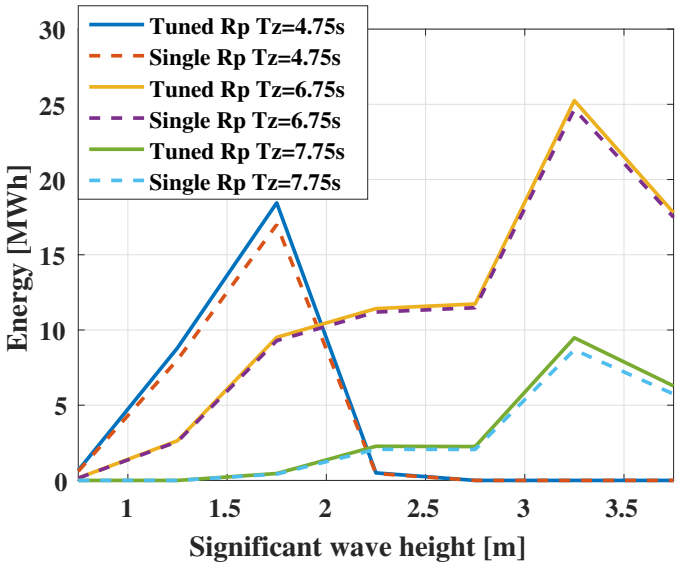

Figure 4.5: Energy differences between the tuned and single R_p for different T_z values.

The values presented here are the average values, however the instantaneous power of each sea state includes significantly higher peaks. In order to be able to harness the previously calculated total average extracted energy, the WEC generator needs to be designed for the highest peak power, which means that the WEC unit would be over 10 times oversized. The oversized WEC generation unit would not only be costly, but also most probably operate with a lower efficiency for the sea states with high probabilities of occurrence, which are the sea states that contribute the most to the overall energy capture. In order to remedy this issue, a peak power limit can be introduced, which means that all power peaks exceeding this value will be limited to it. This is called power curtailment. In order to decide the power curtailment limit, the average extracted energy for different power curtailment levels are calculated. Figure 4.6 shows the energy extraction variation for different power curtailment values. Based on this investigation, the rated power of the WEC unit in this work is selected to be 335 kW, which causes a mere energy loss of 7.5%, roughly.

Figure 4.7a shows the non-curtailed instantaneous and the average power for the sea state $H_s = 3.25$ m and $T_z = 8.25$ s. It can be seen that the average power for this sea state is 184 kW and maximum peak power can be over 10 times this value. Figure 4.7b shows the described power limitation. It can be seen that even though all the peaks are limited to the power curtailment level, 335 kW, the average power is decreased from 184 kW to 143 kW, for the selected high energy sea state. Due to the low probability of occurrence of the high power sea states as well as the insignificant impact of it on the average extracted power value, the power curtailment manages to decrease the WEC generation unit size by approximately 7 times. Note

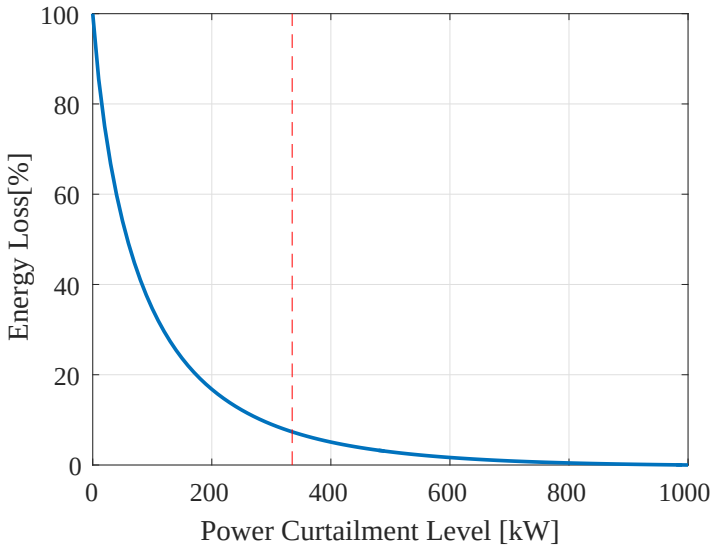

Figure 4.6: Energy loss percentage dependent on the peak power curtailment level.

that the power curtailment study is performed using the previously limited sea states, meaning that the average available wave energy is circa 90% of the unlimited value. In the case of using all sea states depicted in Table **??**, the downsizing would be significantly more pronounced.

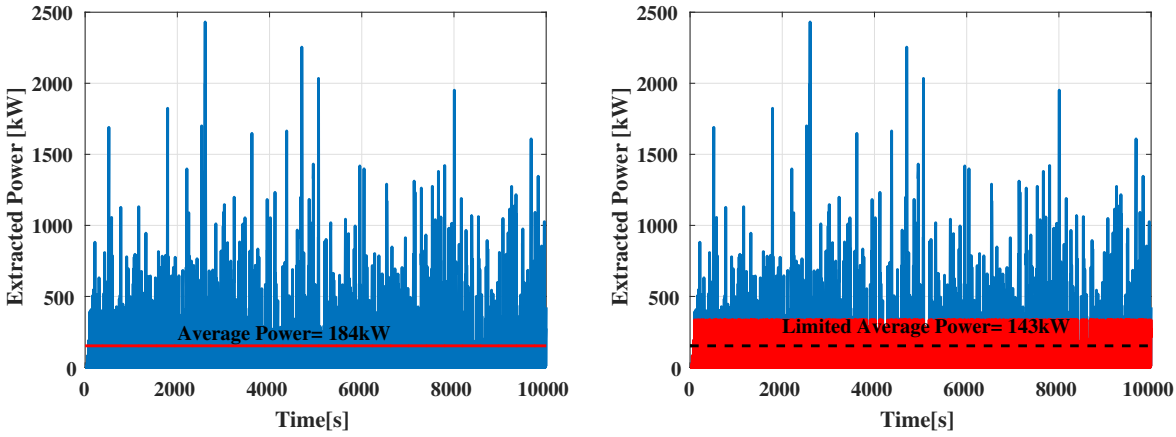

(a) Non-curtailed

(b) Curtailed

Figure 4.7: Non-curtailed and curtailed instantaneous and average power values for $H_s = 3.25$ m and $T_z = 8.25$ sea state.

4.3 Linear to Rotational Motion

The WEC system used in this work consists of the single point absorber to harness the wave energy, a stiff rod together with an ideal gearbox in order to translate the linear motion into

rotational and this is coupled to the WEC generator shaft. The generator is controlled through a two level three phase power electronic converter. Figure 4.8 shows an overview of the WEC system that is considered.

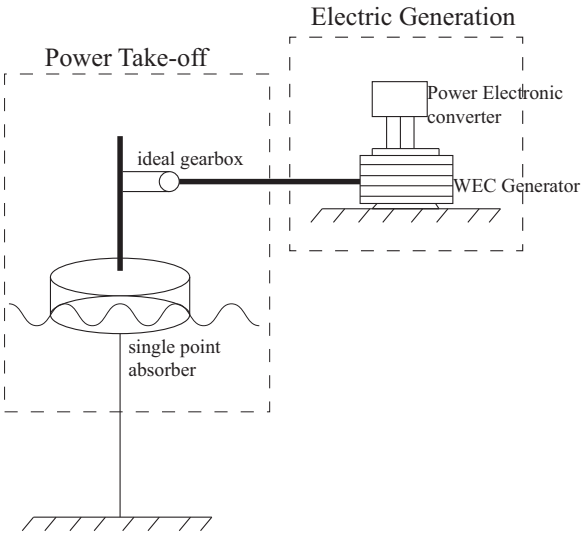

Figure 4.8: An overview of the WEC system.

The power take-off of the WEC is assumed to be designed to have a maximum power capture of 335 kW. Figure 4.9a shows the power and Figure 4.9b shows force obtained for the heave motion of the buoy as a function of vertical speed, both for the unlimited and the 335 kW maximum power capture cases.

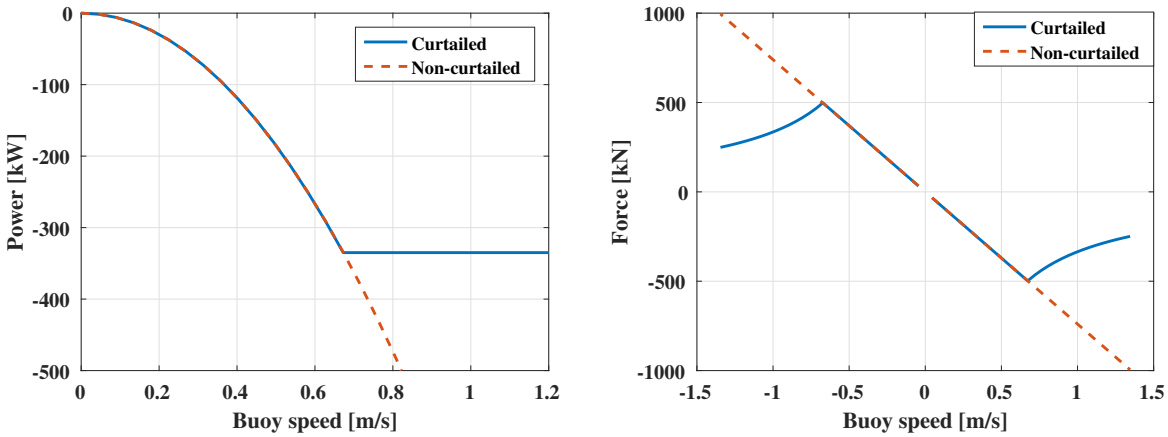

(a) Buoy power

(b) Buoy force

Figure 4.9: Curtailed and non-curtailed power and force from the buoy as a function of the buoy speed.

It can be observed that for the non-curtailed buoy power the force-speed relation is linear

and for the curtailed case, the force decreases for the increasing speed at the constant power values, based on (2.23).

The WEC generators in this project are radial flux machines, therefore the characteristic parameters are rotational vectors. Given that the mechanical losses of the power train are neglected, the output power from the buoy is transferred entirely to the generator input,

$$P_{buoy} = P_{gen} \tag{4.1}$$

which states that the power of the buoy is equal to the input power of the electric generator at any given time, therefore

$$f_{buoy} v_{buoy} = T_{gen} \omega_{gen} \tag{4.2}$$

The rated rotational speed of the WEC generators are selected to be 1500 rpm. The maximum generator torque can be calculated as

$$T_{gen_{max}} = \frac{P_{max}}{\omega_{rated}} \tag{4.3}$$

where P_{max} is 335 kW and the rated speed is 1500 rpm, which results in a maximum torque of 2.14 kNm. The required torque-speed relation of the buoy motivates the use of the field weakening strategy for high speed operation, which is an effective way to utilize the electric drive. The linear motion is translated to rotational motion through a mechanical translation gear. The translation ratio is expressed as

$$k_{gb} = \frac{f_{buoy_{max}}}{T_{gen_{max}}} \tag{4.4}$$

The translation ration for this application is calculated to be 2230 $1/m$.

Chapter 5

Generator Design and Verification

In this chapter, four main generator designs, IPM, VPM, SMPM and the PM assisted SRM, are evaluated for the task of being the WEC generator. These four designs are selected due to their popular use in variable speed drives, such as the electric vehicle and wind power applications. The stack length - outer diameter ratio of the generators are selected based on the previous work conducted on this project, which is presented in [55]. It can be argued whether the selected generators are the most optimal designs. In this thesis, the main focus is on investigating and quantifying the impact of various design and material possibilities, therefore the main aspects of the variations will remain even though another starting point is selected.

The four main generators have the same steel lamination material, same stator geometry as well as the axial length and the same magnet weight per volume. The electrical steel used in the main designs is M400-50A [56], the dysprosium NdFeB magnet is NMX-37F [57]. The IGBT modules that are used in this work have 225 A nominal current and 1700 V voltage blocking ability [58], and each half phase leg consists of two parallel modules in order for the converter to be able to operate at the rated current of the generator. More information regarding the semiconductor components used in this work can be found in Appendix A. The key geometry data and the rated operation parameters of the machines is given in Table 5.1.

TABLE 5.1: Key Geometry and Operational Parameters of the WEC Generators

Stator outer diameter	400 mm
Stator inner diameter	282 mm
Rotor outer diameter	280 mm
Rotor inner diameter	140 mm
Axial length	600 mm
Number of pole pairs	4
Number of slots	48
Number of turns per layer	6
Number of parallel branches	4
Slot body height	30 mm
Slot body width	12 mm
Magnet area per pole	450 mm^3
Rated Power	335 kW
Rated Speed	1500 rpm
Rated Current RMS	305 A
Peak line to line Voltage RMS	1100 V

The stator outer diameter is 400 mm and the axial length is 600 mm. The cross sectional magnet area per pole is 450 mm^2. All machines have 8 poles and 48 stator slots with double layer windings. The axial overhang is considered to be 35 mm and the length of the end windings is 440.7 mm, based on (3.41).

5.1 Default WEC Generator: Interior Permanent Magnet Generator

The original machine is selected to be an interior permanent magnet machine, which was proven to be a favorable design at earlier stages of this work [59]. Figure 5.1 shows a cross sectional illustration of the default IPM generator used in this work.

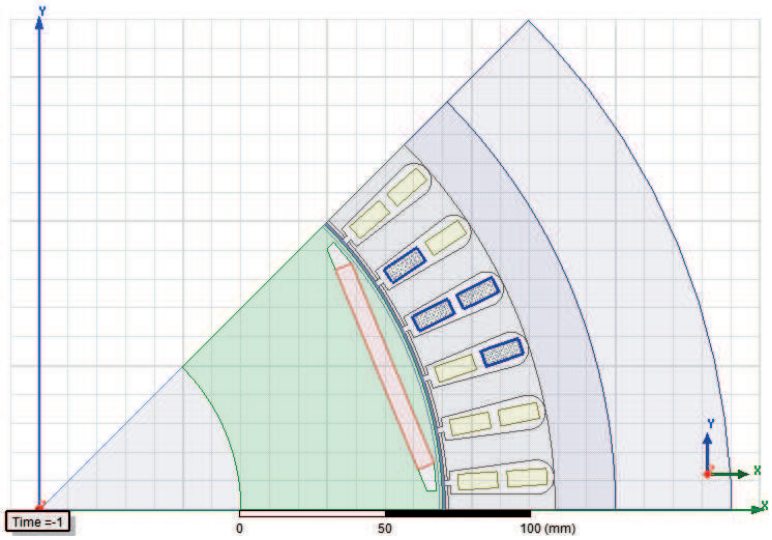

Figure 5.1: The cross sectional depiction of the IPM generator

Here, the phase-A coils are highlighted.

5.2 No-load Performances of the WEC Generators

5.2.1 Interior Permanent Magnet Generator

In order to study the adequacy of the permanent magnet amount and strength, no load simulations are performed. Figure 5.2 shows the flux density field for a cross-section of the generator. It can be seen that the flux density in the stator tooth and the yoke is 1.5 T which is an appropriate value. The rotor iron at the magnet corners is saturated, which prevents a great part of the magnetic flux to go in the iron bridges instead of over the air gap into the stator.

In Figure 5.3a and 5.3b, the three phase flux linkages and the induced voltages are depicted. It can be seen that the flux linkages have the desired cosine behaviour and the phase sequence is correct. The induced voltages are fairly sinusoidal.

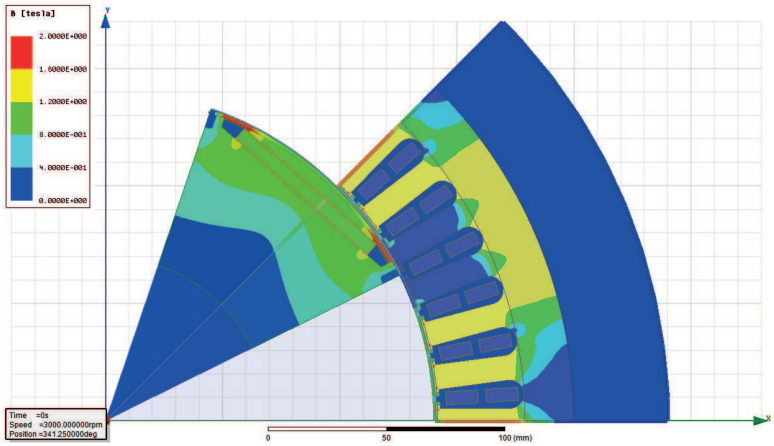

Figure 5.2: No load flux density distribution of the IPM generator

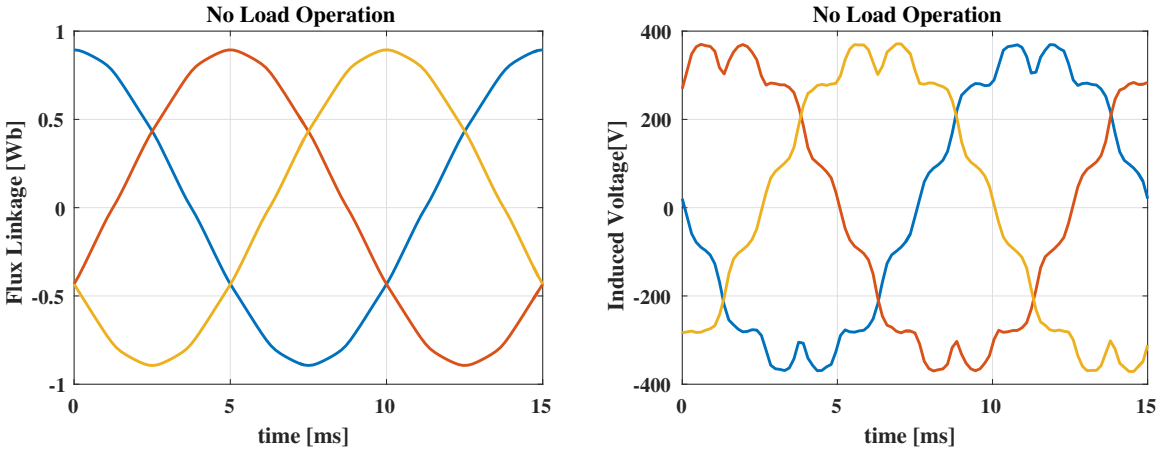

(a) Flux linkage

(b) Induced voltage

Figure 5.3: No load three phase flux linkages and induced voltages of the IPM generator

5.2.2 V-shaped Interior Permanent Magnet Generator

Another type of interior permanent magnet generator is the v-shaped permanent magnet machine, where a pair of magnets that resembles a v-shape are interior mounted to the rotor, in order to form one machine pole. Due to the rotor geometry, the VPM generator has a higher saliency compared to the IPM generator. Figure 5.4 shows the flux density distribution through the cross section of the machine. It can be seen that the flux density in the stator tooth is reduced. The flux density at the stator yoke reaches 1.5 T.

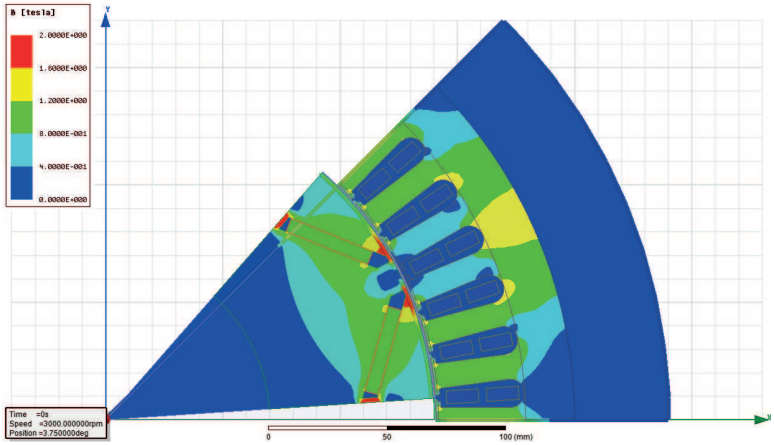

Figure 5.4: No load flux density distribution of the VPM generator

5.2.3 Surface Mounted Permanent Magnet Generator

Surface mounted permanent magnet generators are one of the most common types of permanent magnet generators, and therefore such a design is considered in this work. Figure 5.5 shows the no load flux density field of the surface mounted generator. Once again the 1.5 T flux density at the stator tooth is reached.

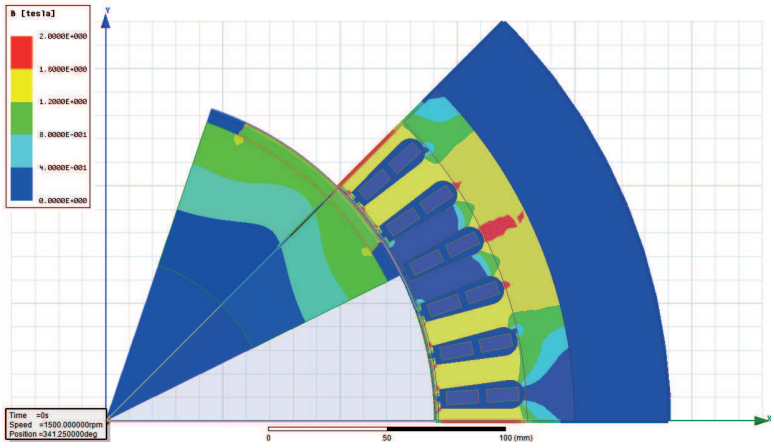

Figure 5.5: No load flux density distribution of the SMPM generator

5.2.4 PM Assisted Synchronous Reluctance Generator

The no load flux density field of the PM assisted synchronous reluctance (SRM) generator is shown in Figure 5.6. In this thesis, when the notation PM assisted SRM is used the magnets are of the same type as the previous designs. In later chapters when a ferrite magnet used as the SRM magnets, it is named Ferrite assisted SRM.

It is shown that the flux density in the stator teeth is approximately 1 T, which is considerably

lower than the previously mentioned generators, due to the deep-set placement of the magnets. However, the magnet flux linkage does not affect the overall torque as severely as for example the SMPM generator, since the reluctance torque is the prominent torque component given the highly salient rotor design.

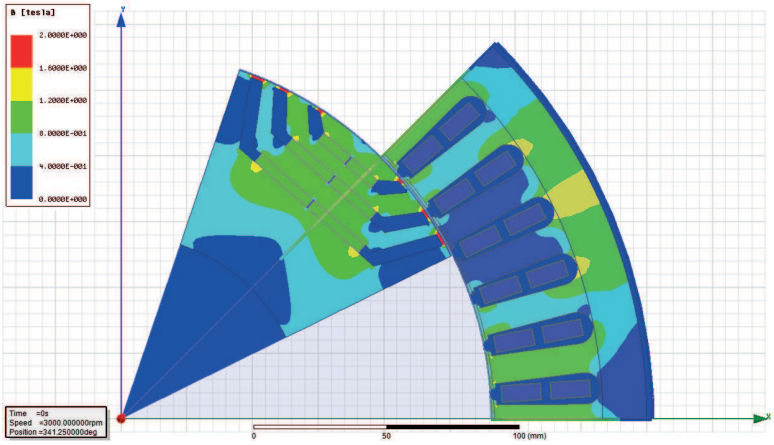

Figure 5.6: No load flux linkage density of the PM assisted SRM generator.

5.3 Operating Point Comparison of the Permanent Magnet Generators

Figure 5.7 shows the flux linkage on the d-axis in relation to the q-axis current, when d-current is kept zero, i.e the magnet flux linkage according to (3.29). It is observed that the no load flux linkage of the IPM is approximately 0.87 Wb and it decreases with increasing current, i.e. increasing saturation level. The no load magnet flux linkage of the VPM is 0.75 Wb and the saturation is fairly prominent for this generator. It can be also observed that the permanent magnet of the SMPM design supplies a no load flux linkage of 0.96 Wb, which is significantly higher than the IPM and VPM generators. Even though the high no load flux linkage level of the surface mounted design, a drawback of this magnet placement is that the magnet losses are higher compared to the interior magnet variants. The no load flux linkage of the PM assisted SRM generator is 0.71 Wb which is lower than the previous machines.

Figure 5.8a shows the analytically calculated operation diagram of the IPM generator. The dashed current trajectory describes that the generator is gradually loaded from no load to maximum current level, 305 A RMS. The current angle is calculated based on maximum torque per ampere control strategy until 1500 rpm and based on a field weakening algorithm until 3000 rpm, which is approximately the maximum translated rotational speed of the buoy. Figure 5.8b shows the d-q current variation within the operating range of the WEC for the VPM generator. The current magnitude and the angle is calculated based on the MTPA control strategy until the maximum voltage is reached and the field weakening algorithm determines the current angle while the magnitude is the maximum.

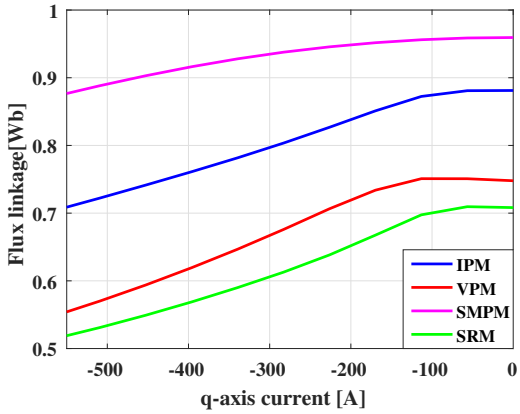

Figure 5.7: Flux linkages as a function of q-axis current for zero d-current.

The SMPM generator is simulated for the same operating conditions as mentioned earlier. The d-q currents within the operating range is shown in Figure 5.8c. It is observed that the current angle is much smaller compared with the interior machines viewed earlier, only deviating a few degrees from the -90^o current angle even at high current operations. Theoretically, the surface mounted machine is non-salient, meaning that the values of the d and the q inductance are equal. However due to the saturation of the magnetic path in the rotor iron, the reluctance paths end up having different permeability values, therefore there is a slight difference between the inductances. Traditionally, SMPM machine is controlled only by the q-current, however, in this work due to the slightly non-ideal behaviour, MTPA control strategy is used for this design as well.

Figure 5.8d shows the d and q current variations for different operating points for the PM assisted SRM generator. It is observed that the current angle is higher than those of the previously studied permanent magnet generators, which indicates a higher saliency.

Figure 5.9a shows the torque requirement of the buoy and the electrodynamic torque that can be supplied by the machines. Similarly, Figure 5.9b shows the power requirement of the buoy and the machine power that is available.

It can be seen that all the machines have adequate torque during the linear-load operation, and only the SMPM generator torque fails to fulfill the buoy requirement at field weakening operation. This is due to the fact that the SMPM torque depends greatly on the magnet torque due to its very low saliency (theoretically non-salient). Since the current angle must increase in order to operate in the field weakening region, as well as the fact that the added reluctance torque originating from the increased current angle is very low, the SMPM machine has a poor field weakening performance. Accordingly, it can be expected that the more salient machines can achieve a better performance during the field weakening operation. The most salient generator amongst the investigated is the PM assisted SRM generator, which is the design that supplies the greatest rated torque and has the best field weakening performance.

Table 5.2 shows the d and q axis inductances and the no load flux linkages of the investigated WEC generators at rated operation. It can be seen that the SMPM inductances are quite close in

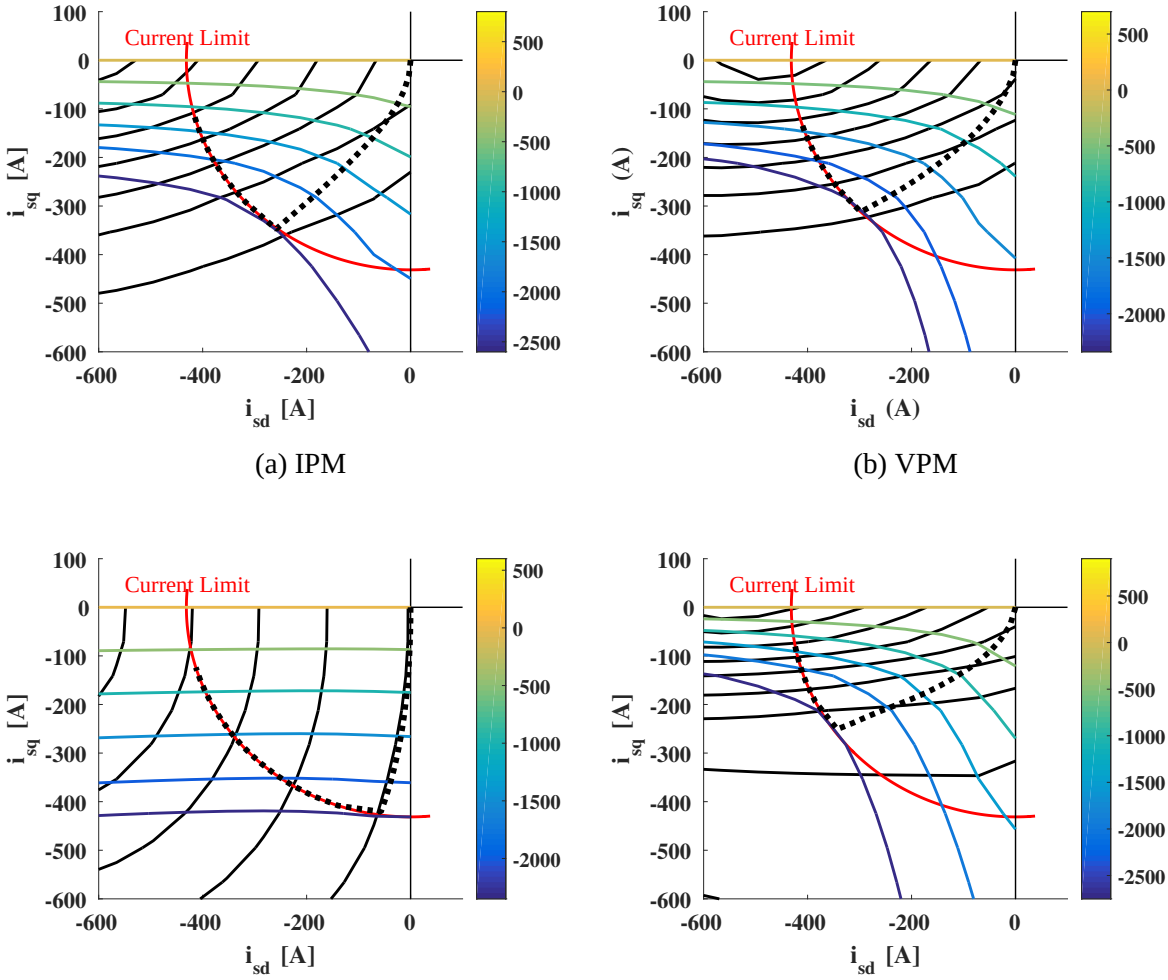

(a) IPM

(b) VPM

(c) SMPM

(d) PMa SRM

Figure 5.8: Operation diagram of the WEC generators.

value and the most salient machine is the PM assisted SRM generator.

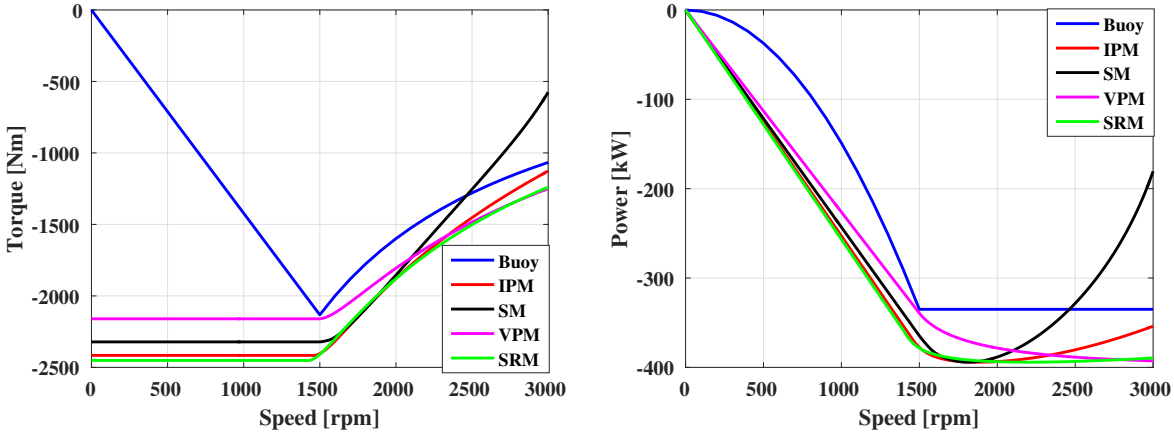

(a) Torque (b) Power

Figure 5.9: Torque and Power trajectories of the permanent magnet generators and the buoy requirement of the WEC generator designs.

TABLE 5.2: d-q inductances and the no load flux linkages of the studied WEC generators at rated operation

Generator Type	d-inductance mH	q-inductance mH	No load flux linkage Wb
Interior Permanent Magnet Generator	1.016	2.672	0.87
V-shaped Interior Permanent Magnet Generator	1.375	3.03	0.75
Surface Mounted Permanent Magnet Generator	1.135	1.09	0.96
PM Assisted Synchronous Reluctance Generator	1.19	4.686	0.71

Chapter 6

WEC Unit Operation

6.1 Operating Point Determination

The WEC generators are to be able to operate on the maximum operating trajectory required by the buoy. Figure 6.1 shows the torque-speed requirement of the buoy and the PTO, which is the ideal operating trajectory, the maximum torque-speed capability of the generators and the resulting operating trajectory. It can be seen that IPM, VPM and SRM generators can follow the required trajectory, however the SMPM generator cannot supply enough torque at the highest speeds (see Figure 6.1c), therefore it has a different operating trajectory with a slightly lower torque value for the higher speeds. The lower torque trajectory of the SMPM generator results in a 0.14% decrease in the annual energy production, which is a very slight impact, therefore this design can be used as a WEC generator.

Figure 6.2a shows the magnet torque values and Figure 6.2b shows the reluctance torque values of the different generator designs. The magnet torque is dependent of the flux linkage, based on (3.17) and the reluctance torque depends on the difference between the d and q inductances, as shown in (3.18). The reluctance and magnet torque values are in correspondence with the expected results that are based on Table 5.2. It can be seen that the SMPM generator, which has the highest flux linkage, has the highest magnet torque. The magnet torque increases in order to accommodate the increasing load torque until the rated speed is reached and decreases drastically for increasing speeds. Moreover the slight increase of the reluctance torque during the field weakening operation can be seen. The most salient design, the PM assisted SRM has the highest reluctance torque throughout the operation. It is also observed that for the designs that have high magnet torques, the reluctance torque is lower and vice versa.

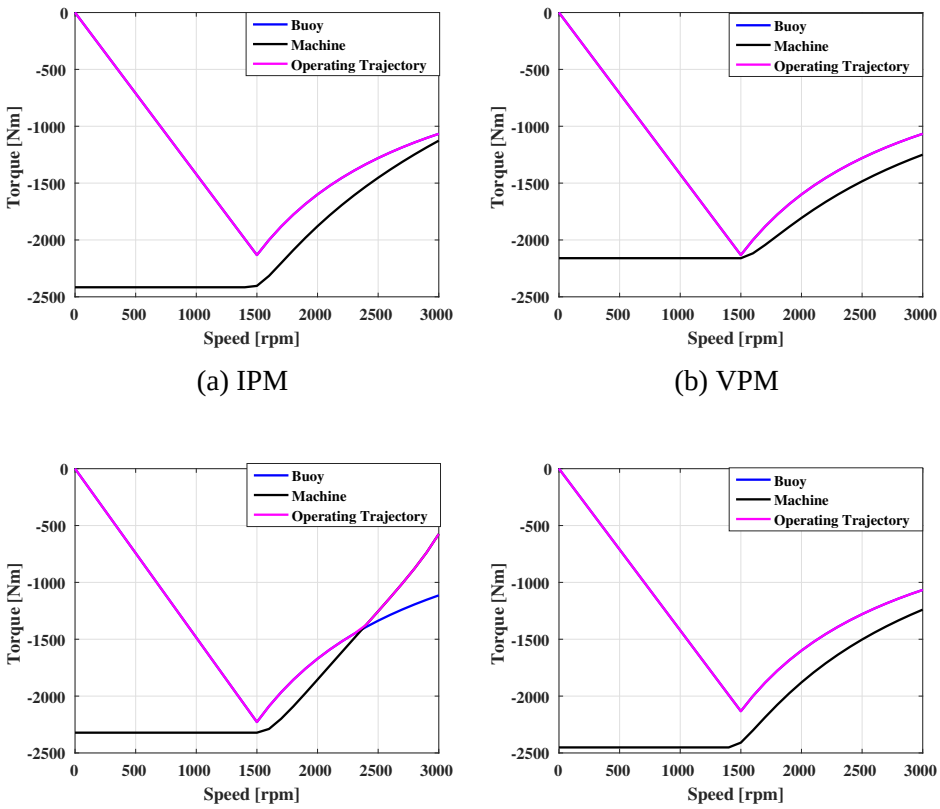

(a) IPM (b) VPM

(c) SMPM (d) PMa SRM

Figure 6.1: Machine capability and operating points of the WEC generators.

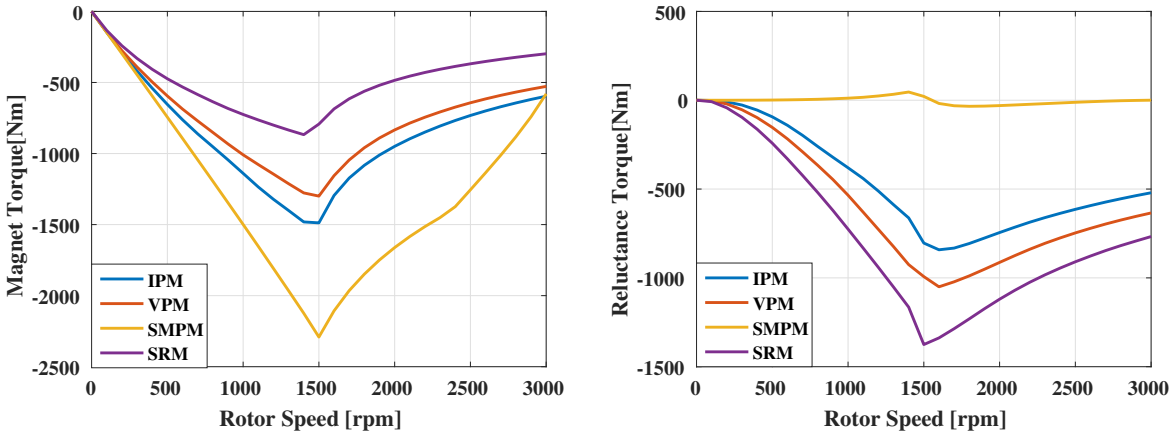

(a) Magnet torque (b) Reluctance torque

Figure 6.2: Comparison of the torque components of the WEC generators.

6.2 Determination of the Power Losses and the Energy

Once the operating trajectory is decided, the required d-q currents and the electrical frequency are calculated for each selected operating point. These parameters are fed to the FEM software in order to assess the operation of the corresponding point and the machine losses are obtained. It is to be noted that the core losses obtained through the FEM calculations are expected to be lower than the realistic results (such as the core losses obtained through experimentation), due to the methods used by the FEM software and more importantly the neglected material degradation caused by the punching or laser cutting of the electric steel sheets. More information about the degradation depth and determination of the non-degraded and fully degraded magnetic characteristics of the sheets can be found in [60] and [61]. In this work, no compensation is performed for adjusting the core loss values, since each different generator design is analysed using the same FEM software and the main objective is to compare their behaviour. Furthermore, the mesh size and the time steps of the FEM simulations are kept unchanged throughout the work in order to eliminate all software based factors that could affect the results.

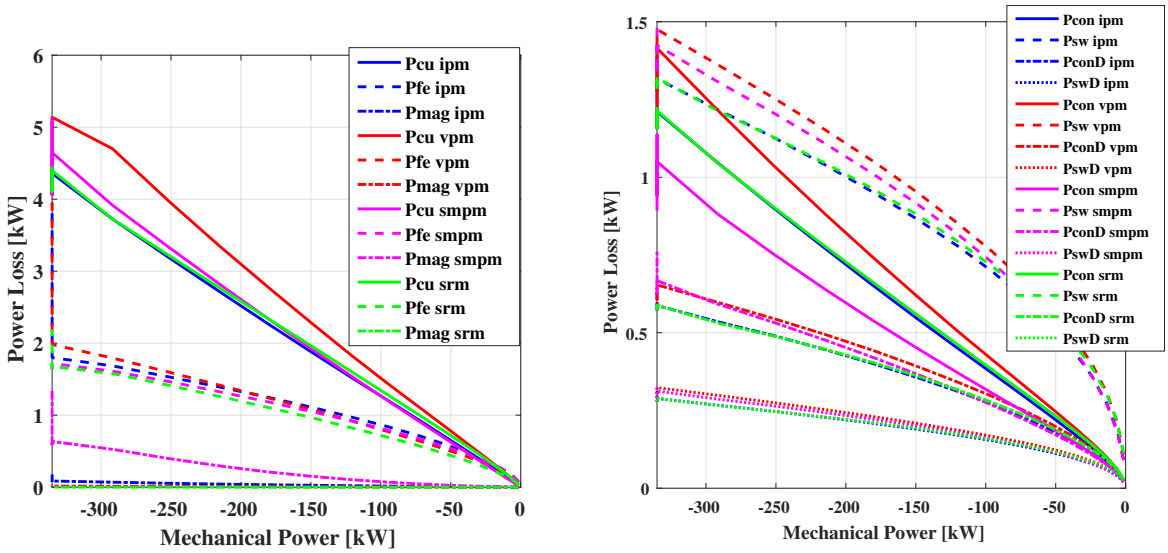

(a) Machine losses

(b) Converter losses

Figure 6.3: Power losses of the main WEC generators.

Figure 6.3a shows the copper, core and magnet losses of the WEC generators. It can be seen that the machine losses vary with the power level, e.g. the SMPM has the lowest losses for low power levels (i.e. low H_s and T_z), yet the losses grow with the increasing input power. A very distinct result is that the magnet losses are drastically higher for the SMPM generator, which is typical for surface mounted machines. Figure 6.3b shows the conduction and switching losses of the IGBT switches and the diodes of the power electronic converter. The switching losses of the IGBTs are dominating, and the conduction losses of the IGBTs are roughly 50% lower than the switching losses. The switching frequency is selected to be $2\ kHz$ for all generators. It can be seen in these figures that at maximum power there are several values of losses. This is

due to the wide range of speed and thus operating points that have the same power at the field weakening operation.

Figure 6.4a shows an overall comparison of the total losses of the WEC generators. Up until $70\ kW$ input power the SMPM generator has the lowest losses, however they increase with increasing power. The VPM generator has the poorest performance throughout the operation range. The SRM generator has the lowest losses for the higher power levels, due to its effective performance during field weakening. Figure 6.4b, shows the total losses of the WEC generators as a function of the rotor speed. The constant torque and field weakening regions can be clearly seen. The losses increase with the increasing speed until the rated speed. Here, the field weakening control replaces MTPA control, since the converter voltage limit is reached. First, the losses decrease due to the decreasing fundamental flux, however since both the current magnitude and the rotor speed are increasing, the total losses increase for higher speeds of the field weakening region.

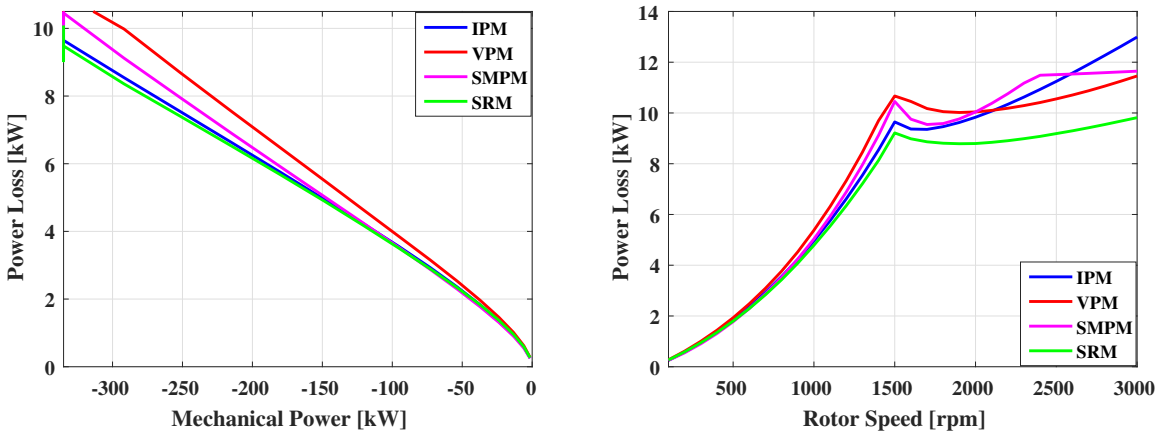

(a) Mechanical power

(b) Rotor speed

Figure 6.4: Comparison of overall losses of the WEC generators as a function of mechanical power and rotor speed.

Figure 6.5 shows the efficiency comparison of the WEC generators for the whole operating range and for the low power operation. It is again seen that the efficiency relations between the generators vary with the level of input power. For lower power levels, the SMPM has the highest efficiency and for higher power levels the PM assisted SRM has the best performance. The IPM generator has consistently high performance throughout the operation range and the VPM has the poorest. This finding was unexpected, since the VPM design is favorable for many applications. Due to this variation in efficiencies it is not intuitive to realize which generator could capture the most energy, since the WEC most often is active at the low power region, yet better efficiency at high power levels can cause a distinct increase in energy generation. In order to be able to quantify the generator operations from an energy point of view, the WEC generator energy production and loss are studied.

Figure 6.6 shows the total annual energy production and loss values of the generators. As speculated, there is no distinct difference between the IPM, SMPM and SRM generators en-

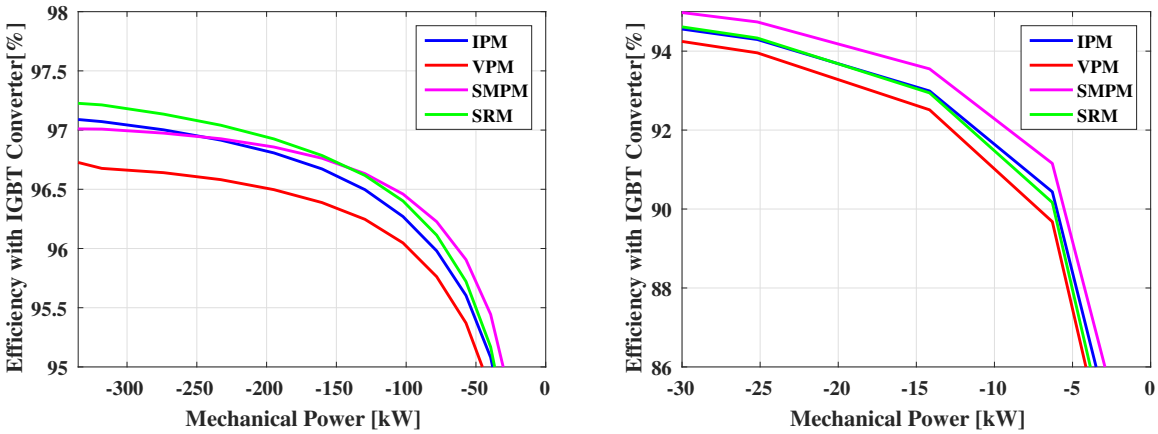

(a) Overall (b) Low power

Figure 6.5: Efficiency comparison of the WEC generators.

ergy productions and losses. The VPM generator has the lowest production, due to having the highest losses. This is expected due to the fact that the VPM generator has the lowest efficiency throughout the WEC operation.

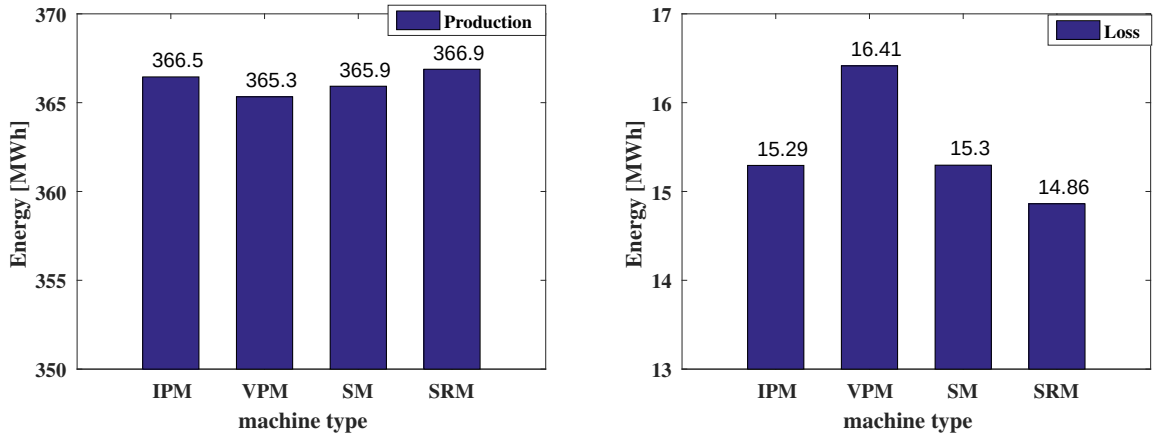

(a) Production (b) Loss

Figure 6.6: Annual energy productions and losses.

6.2.1 Instantaneous Behavior of the IPM Generator

The operating points of the generators are selected using the buoy operation trajectory, however for simplicity, several speed equidistant points are selected for detailed simulations and the simulation results would be reference points. The instantaneous performance of the generators are achieved by interpolating the reference points with the instantaneous buoy requirement. Figure 6.7 shows the instantaneous power from the buoy and the IPM generator at 1.75 m H_s and 5.75 s T_z, which is one of the most occurring sea states and at 3.25 m H_s and 8.25 s T_z, which is a high power sea state. It can be seen for the medium sea state, except for some peaks, the power curtailment level is not reached, however for the maximum sea state the power level is almost consistently at the curtailment level. The probability of occurrence of the medium sea state is 7.3% and of the high power sea state considered in this work is 0.2% therefore the constant curtailment of the maximum level does not impact the energy capture greatly, whereas even small power limitations on the most occurring states might have significant effects.

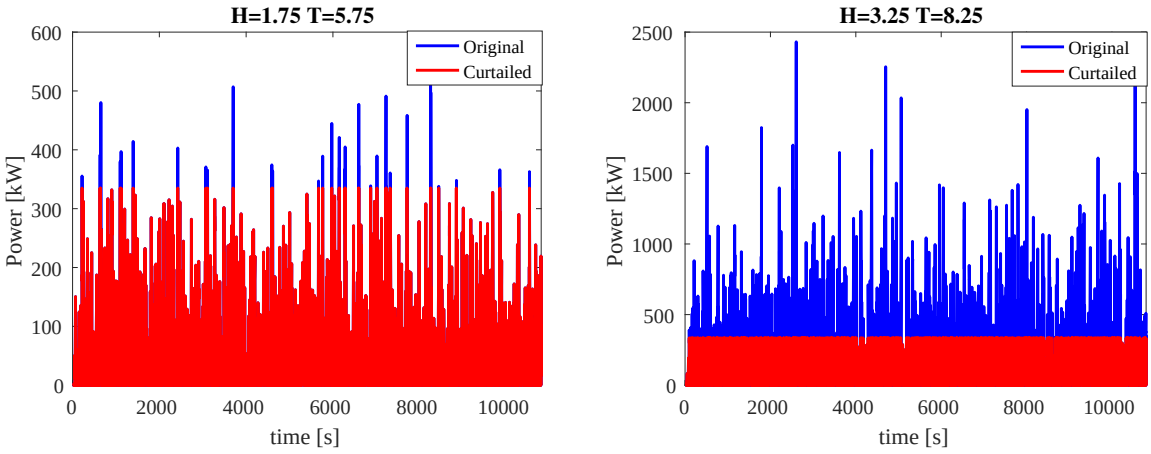

(a) $H_s = 1.75$ m and $T_z = 5.75$ s

(b) H=3.25 m and T=8.25 s of IPM

Figure 6.7: Instantaneous power of IPM at different sea states.

Figure 6.8(a) shows the instantaneous machine losses and Figure 6.8(b) is zoomed in for better understanding the instantaneous behaviour. The red line in instantaneous plots indicate the mean value of the parameter. Similar to the instantaneous power, the instantaneous losses also have a high ratio between the peak and the average values. The peak values of the copper and core losses are approximately 4 kW and 2 kW respectively, whilst the average values of these losses are 0.8 and 0.4 kW.

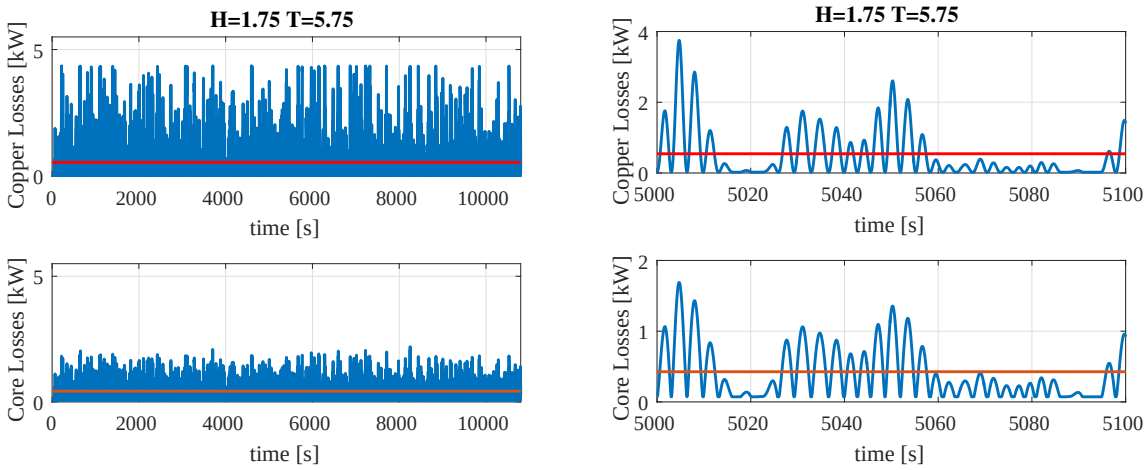

(a) Overall

(b) Zoomed in

Figure 6.8: Instantaneous machine losses at H=1.75 m and T=5.75 s of IPM.

6.3 Economical Evaluation of the Main Designs

In order to select the most favorable WEC generator, the economical impacts of the generator performances are to be quantified, using the life cycle cost analysis. For simplicity, only the electric generation unit is investigated economically, since the price information of the mechanical part, grid connection components and the maintenance is expected to be the same for all WEC systems. Due to this, the economical evaluation is studied using the LCC method purely for the electric drive, rather than the Levelized Cost of Energy (LCoE).

In order to calculate the LCC values of the investigated generators, the investment cost of the generator needs to be determined. Table 6.1 shows the prices of the materials that are used for the WEC generator construction. The VACODUR 48 cobalt-iron material and Stronium Ferrite permanent magnet are used in the coming chapters.

TABLE 6.1: Price of the materials used in machine construction as €/kg.

M400-50A	NeFeB	copper wire	VACODUR 48	Stronium Ferrite
2.5	50	8	20	5

The weight of the copper, iron and neodymium magnets used to construct the WEC generators are shown in Table 6.2. The copper and magnet weights of all four designs are equal, since the magnet volume is constant and all generators have the same stator configuration. Moreover, the iron volume that is purchased for construction is also considered to be the same for all designs in this work. This is due to the fact that, even though the rotor configurations are different, the stator and rotor for each material are punched out from a circular sheet that has the stator outer diameter. The unused parts are discarded, therefore the rotor design does not affect the volume of the purchased electric steel. Approximately 77% of the machine is made of electric steel, 22% is constructed of copper wire and 2% is the permanent magnet content.

TABLE 6.2: Weights of different materials used in machine construction in kg.

M400-50A	NMX-37F	copper wire
577	16.2	158

Figure 6.9 shows the components of the investment cost. The most costly material is the electrical steel, due to its high volume, and is followed by the copper wire and the permanent magnets. The manufacturing cost is selected to be half of the total investment cost. The total cost of one generator is 5300 € and the price of the IGBT converter is 1265 € [62].

Figure 6.10a shows the NPVL comparison of the four main WEC generator designs. In this work, the electricity price is assumed to be 30 €$/MWh$ [63]. The WEC life time is considered to be 20 years and the discount rate is set to be 9%. The NPVL shows expected results, since it reflects the energy loss comparison of the generators. The IPM, SMPM and PM assisted SRM generators have similar NPVLs, whereas the VPM has approximately 10% higher cost of losses than the other designs. By using the PM assisted SRM generator as the WEC generator, instead of the default IPM generator, the NPVL decreases by 660 €, which is an expected result since the NPVL is to a great extent dependent on the energy losses.

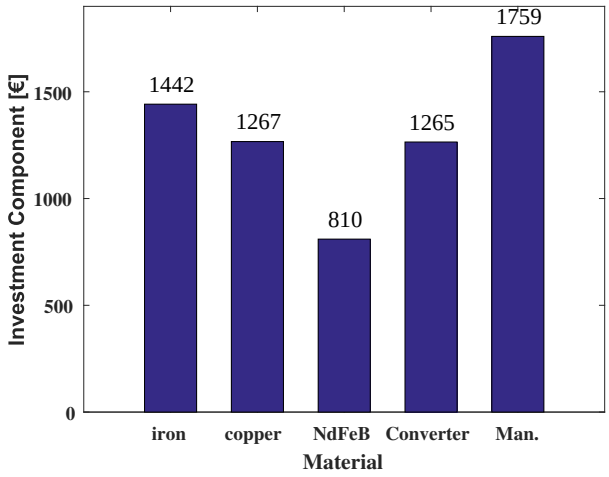

Figure 6.9: Iron, copper, permanent magnet, converter and manufacturing costs.

Figure 6.10b shows the LCC comparison of the four main designs. Since the investment cost is kept constant, the LCC variation is only dependent on the NPVL and the results can be explained in a similar fashion. Based on the LCC analysis of the four main generator types of this work, the PM assisted SRM generator is the favorable WEC generator.

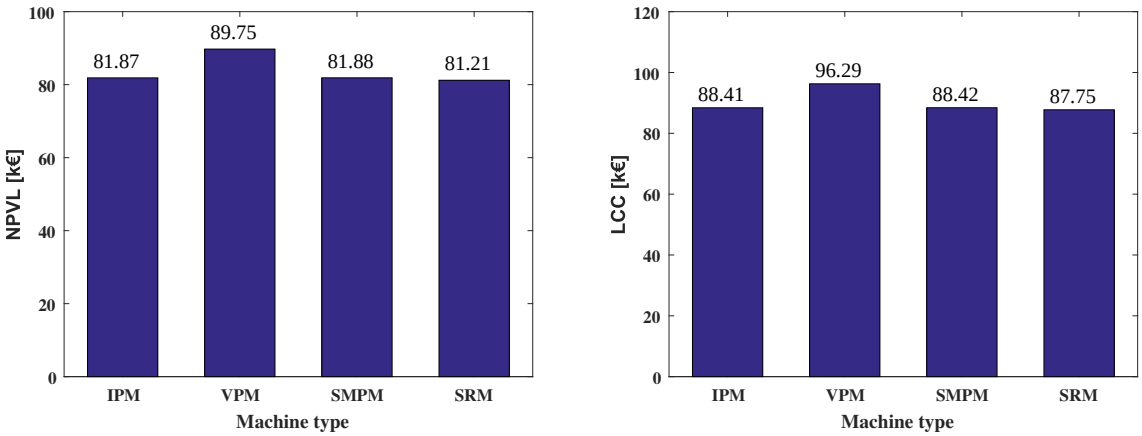

(a) NPVL (b) LCC

Figure 6.10: Net present value of losses and the life cycle cost of the WEC generators.

Chapter 7

Design Variations

In this chapter, various geometric and component designs are investigated in order to better understand the effect of different parameters of the machine geometry and construction materials on the machine performance. The main focus of these investigations is to determine the impact of a specific variation and to what degree it affects the machine performance. The motivation is that the knowledge obtained through these investigations aids a systematic optimization analysis to achieve the ultimate performance for a chosen wave energy application.

7.1 Effect of the Electric Steel Lamination

Electrical machine bodies are manufactured from steel laminations that are stacked together. These materials have different thicknesses and core-loss characteristics, as well as different B-H relations. In this work, the default lamination is selected to be M400-50A, and in this section, M270-35A, M350-50A, M470-50A and M700-50A laminations are studied. Here, the first part of the material name represents the approximate core loss value of the material at 1.5 T and 50 Hz. The second part of the material represents the thickness. The core losses of the electric steel material is decreased by increasing the silicon content of the material, since the added silicone increases the electrical resistivity of the material, therefore the eddy current losses will be decreased [56]. For example, the M270-35A has the lowest core losses and its thickness is 0.35 mm, however this procedure results in a reduced B-H characteristic. In Figure 7.1 the B-H relations of the studied materials can be observed.

It can be seen that all materials have similar trends, yet the M470-50A and M700-50A materials have higher induction levels than the others. The reason might be that the silicon content of these materials are lower than those of the low core loss variants.

Figure 7.2a shows the torque-speed relations, as well as the buoy requirement and Figure 7.2b shows a close up on the rated torques. It can be seen that there is no significant deviation from the original M400-50A design regarding the torque performance, which is as expected. A slight reduction of maximum torque for the M270-50A design is noted.

Figure 7.3a displays the eddy and hysteresis losses of the mentioned designs. It can be ob-

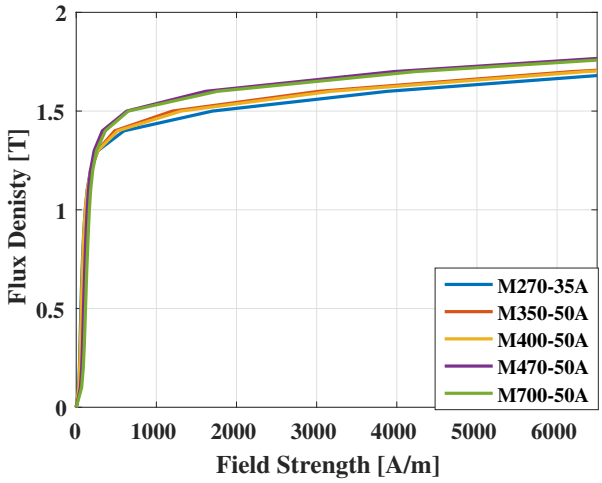

Figure 7.1: B-H curves of the considered steel laminations

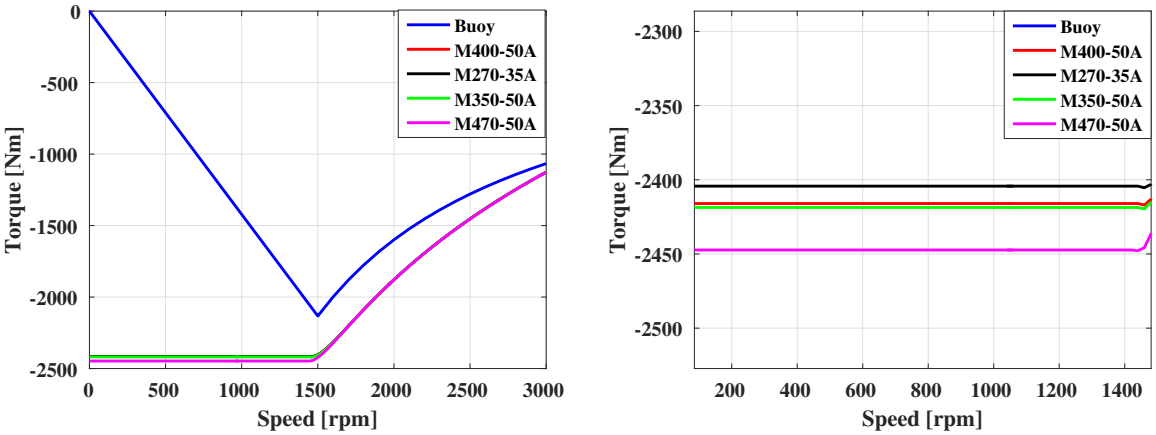

(a) Torque

(b) Rated torque

Figure 7.2: Overall and close-up torque trajectories of different steel lamination designs.

served that the eddy losses for the M270-35A, M350-50A and M400-50A are fairly comparable, however the M470-50A and M700-50A materials have significantly higher eddy current losses. A similar trend is present for the hysteresis losses, however the change is not as drastic. Figure 7.3b shows the copper and core losses of different designs. It can be seen that the steel lamination variation has the biggest impact on the core losses.

Figure 7.4 shows the efficiency comparison of the aforementioned designs. Once again, it is not possible to observe a significant change in efficiency of M270-35A, M350-50A and M400-50A designs, however the efficiency decreases for the lamination designs with higher core loss characteristics.

Since all variants have similar performance, the difference is best quantified through the annual energy production and loss. Figure 7.5 shows the annual energy productions and losses of each design variation. It can be seen that using the lowest core loss material results in a 430

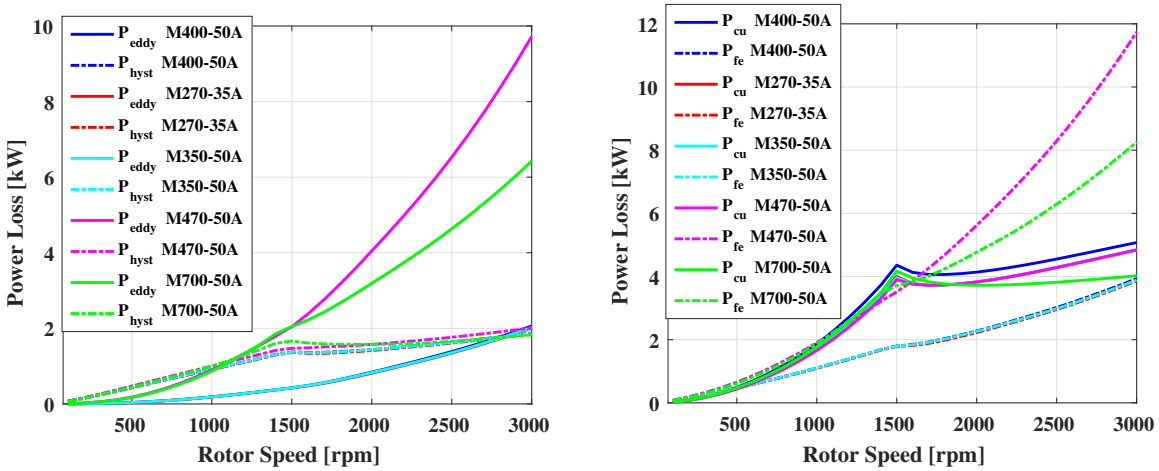

(a) Eddy and Hysteresis Losses

(b) Copper and core losses

Figure 7.3: Power losses for different steel lamination designs.

kWh annual energy production surplus and the highest core loss material has approximately 2 MWh higher annual losses compared with the default design.

Another important aspect to note is that the annual energy loss of the M350-50A lamination design is slightly lower than that of the M270-35A design, even though it is a higher core loss lamination. Owing to the better B-H performance, the M350-50A design can achieve the same operation with lower current due to better induction, compared to the M270-35A design. This would result in lower copper losses, even though using this material increases the core losses, as it is seen in Figure 7.3b. Since the core losses are approximately half of the copper losses, a slight decrease in copper losses have a bigger impact on overall energy losses than the increased core losses. It can be concluded that the M350-50A lamination has the lowest annual energy losses, therefore is the preferable lamination choice from an energy point of view, however the favorable design must be determined based on the LCC results.

Figure 7.6 shows the NPVLs of the WEC generator designs using different lamination materials. It is seen that the M350-50A material has the lowest cost of the energy losses, meaning that as long as the extra cost of this material is less than 3900 €, compared with the default material, using M350-50A generator gives the lowest LCC.

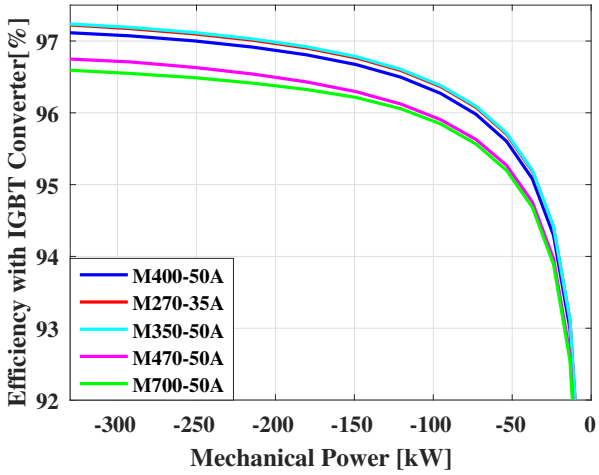

Figure 7.4: Efficiency comparison of different steel laminations

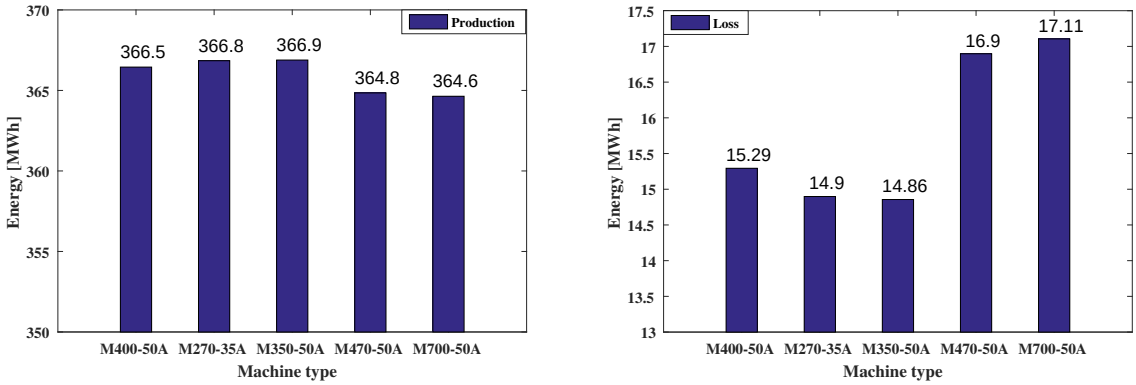

(a) Production

(b) Losses

Figure 7.5: Annual energy productions and losses for different steel laminations.

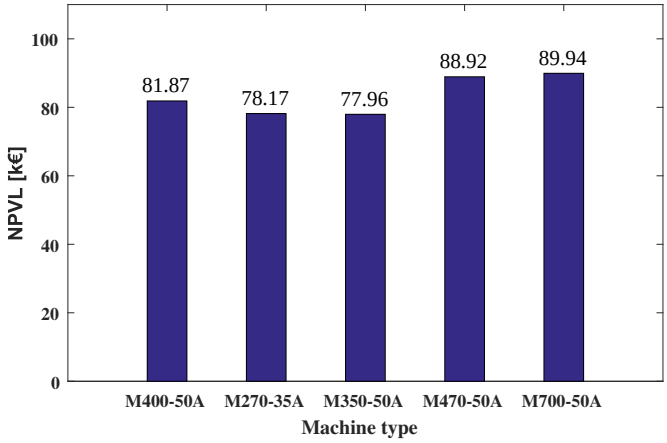

Figure 7.6: NPVL comparison of the WEC generator designs using different laminations.

7.2 Cobalt-Iron Rotor

In this section, the rotor of the IPM generator is constructed using cobalt-iron material, VACODUR 48. Cobalt-iron alloys have the highest saturation polarization of all magnetic alloys, measuring up to 2.35 T [64]. In this work, the cobalt-iron material is used only for the rotor construction in order to increase the air gap flux. The stator is constructed of M400-50A. The cobalt-iron material is not initially preferred for the stator, due to higher core losses compared to the ordinary silicon based electrical steel, however the results are presented for this case for a more extensive comparison. Figure 7.7 presents the B-H curve of the cobalt-iron material in comparison with the M400-50A material.

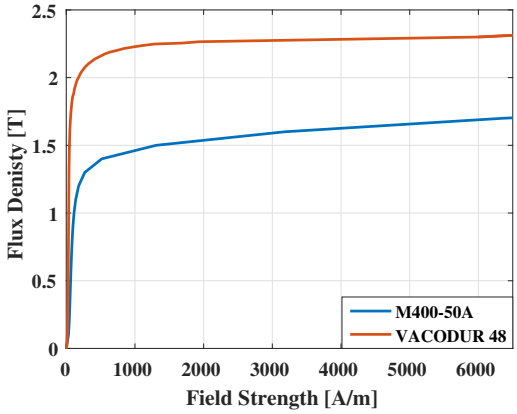

Figure 7.7: B-H curves of the cobalt-iron and the M400-50A materials

The high saturation point of the cobalt-iron material can be clearly seen in this figure. Figure 7.8 shows the torque and power trajectories of the cobalt-iron rotor and totally cobalt-iron WEC generator designs.

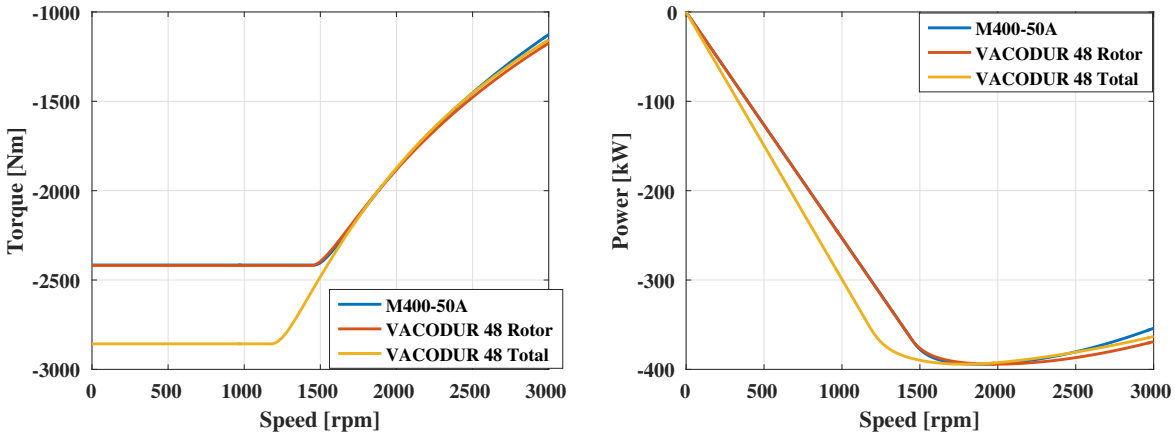

(a) Torque

(b) Power

Figure 7.8: Torque and power trajectories of the cobalt-iron designs.

It can be seen that due to the higher induction levels, the design that uses only cobalt-iron material has the highest rated torque, whereas the cobalt-iron rotor design has similar torque-speed and power-speed relations to the default generator design. Figure 7.9a shows the copper and core losses comparison of the investigated designs. It can be seen that the copper losses are decreased for the cobalt-iron rotor design, due to the lower maximum current. However, the core losses are increased, due to the core loss characteristic of the cobalt-iron material. It can also be seen that when both the rotor and the stator of the machine is constructed of the cobalt-iron material, the core losses are doubled, compared to the original design. This is due to the fact that the high flux in the stator teeth combined with the poor core loss characteristic of the cobalt-iron material result in significantly higher core losses.

Figure 7.9b shows that the core loss increase is predominantly caused by the hysteresis losses.

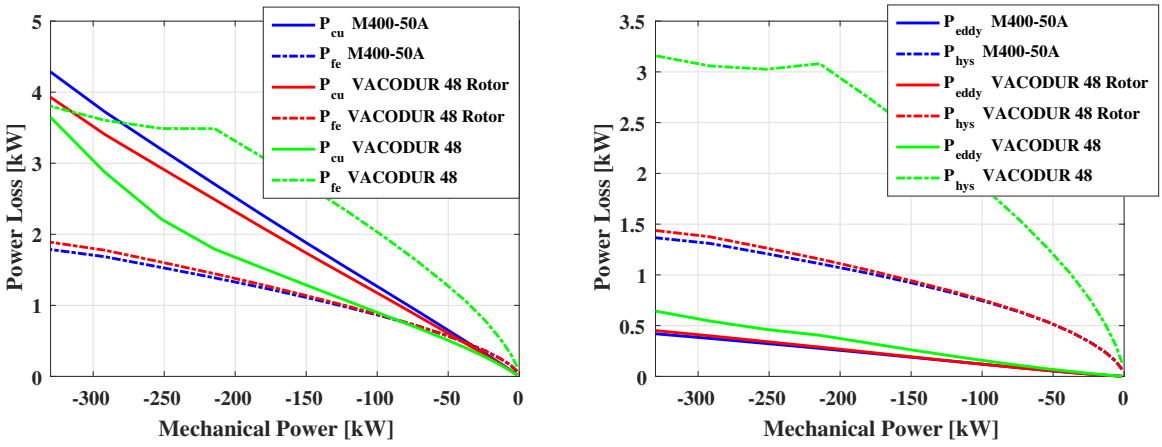

(a) Copper and core losses

(b) Eddy and hysteresis losses

Figure 7.9: Power losses of the cobalt-iron rotor IPM generator designs.

Figure 7.10 shows the efficiency comparison of the studied designs. It can be seen that the cobalt-iron rotor design has a higher efficiency throughout the operation, due to the lower overall losses. Due to the significantly higher core losses, the fully cobalt-iron generator has the lowest efficiency.

The impact of the improved efficiency on the annual energy is shown in Figure 7.11. It can be seen that the annual energy loss is decreased approximately 1.3%. Furthermore, it is observed that using the total cobalt-iron machine, the energy losses increase almost up to 20%, therefore it is omitted from further investigations.

Figure 7.12a shows the NPVL of the IPM design with VACODUR 48 rotor in comparison with the original design. It can be seen that using cobalt-iron material decreases the NPVL by 1.6%. Figure 7.12b shows the investment cost of the cobalt-iron rotor WEC generator, together with investment cost of the default design. It can be seen that the investment cost of the cobalt-iron rotor design is significantly higher than the original IPM generator, due to the high material price.

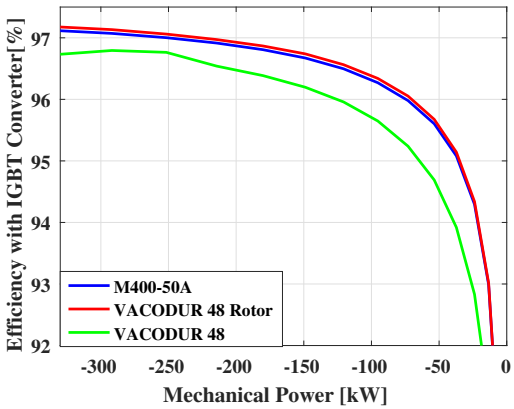

Figure 7.10: Efficiency comparison of cobalt-iron and the initial IPM generator designs.

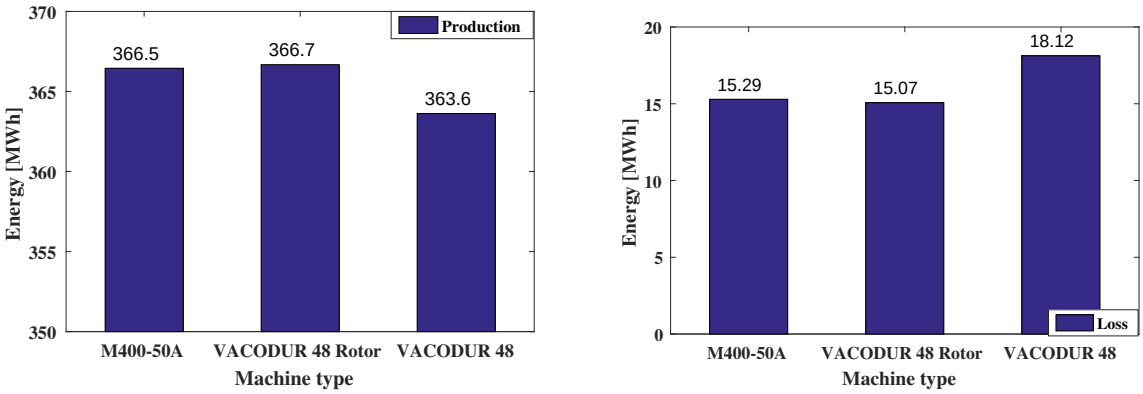

(a) Production

(b) Losses

Figure 7.11: Annual energy for the cobalt-iron rotor IPM generator design.

Figure 7.13 shows the LCC comparison of the cobalt-iron rotor and the default IPM generators. It can be seen that, even though the NPVL is lower, due to the high investment costs, using the cobalt-iron rotor WEC generator increases the LCC by 8%.

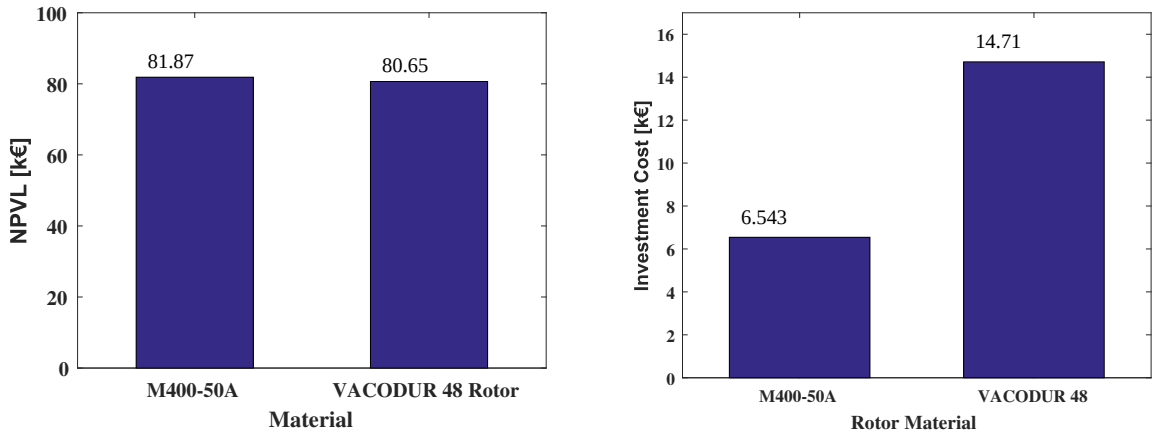

(a) NPVL (b) Investment Cost

Figure 7.12: NPVL and investment cost comparison of the WEC generator designs with M400-50A and VACODUR 48 rotor.

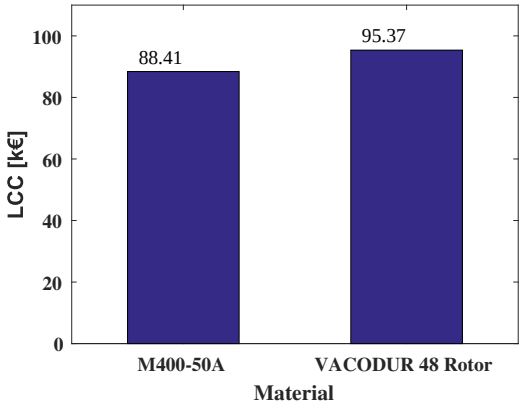

Figure 7.13: LCC comparison of the WEC generator designs with M400-50A and VACODUR 48 rotor.

7.3 Effect of the Stacking Factor

Electrical machines are often made up of laminated sheets of electrical steel, in order to reduce the eddy losses. The laminations are stacked together to construct the machine body. The steel laminations are insulated with a non-magnetic and non-conductive coating and furthermore the sheets are not perfectly flat due to the construction, meaning that the total volume of the laminations, apparent volume, does not have flux carrying capacity. Stacking factor (SF) is the ratio between the effective magnetic volume and the apparent volume.

Stacking factor generally ranges between 90 - 99%, and a theoretical 100% SF means that there is no coating on the sheets. Thick laminations can have high stacking factors, whereas the SF decreases for thinner laminations.

A rule of thumb that estimates the SF based on the lamination thickness is

$$SF = 0.0425\delta_{FE} + 0.6032 \arctan(108.16\delta_{FE}) \tag{7.1}$$

where δ_{FE} represents the lamination thickness [65]. Using this method, the SF values are calculated to be 96% and 94% for the 0.5 mm and 0.35 mm thick laminations, respectively. In [66], it is shown that the SF values calculated using the rule of thumb is roughly 2% lower than actual, therefore the stacking factors of 0.5 mm and 0.35 mm thick laminations are selected to be 98% and 96%, accordingly.

Figure 7.14 shows the copper and core losses of the M400-50A, M350-50A and M270-35A designs. The solid case is analyzed as a lamination with infinitely large SF (99.999% in the FEM software). The M350-50A steel lamination has a thickness of 0.5 mm, which means that its SF is 98%, as the M400-50A lamination. The M270-35A is 0.35 mm in thickness, hence a SF of 96% is selected, as determined previously.

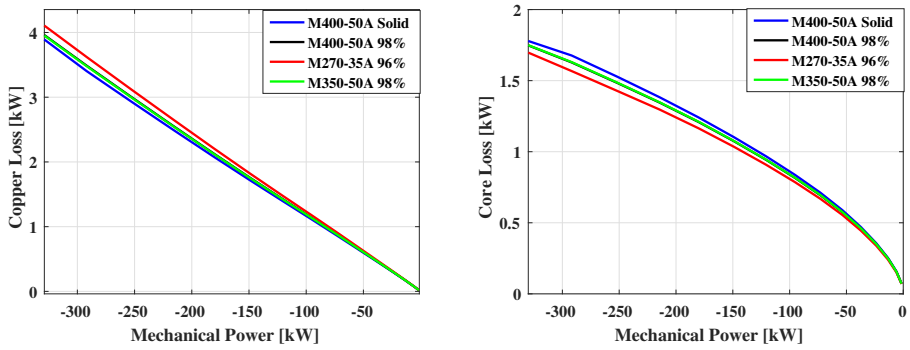

(a) Copper losses (b) Core losses

Figure 7.14: Power losses of the different stacking factors for different steel materials IPM generators.

It can be seen that M350-50A with 98% SF has the lowest copper loss compared with the other laminations, except the infinitely large SF variant, which is not a realistic design. Further-

more, the lowest core loss operation is achieved by the M270-35A with 96% SF, due to the core loss characteristic of this material and lower SF value.

In Figure 7.15, the efficiencies of the investigated designs are depicted. Besides the solid SF, the highest efficiency design is the M350-50A with 98% SF, which is expected since this design has the lowest copper losses amongst all the investigated lamination designs and furthermore, the M350-50A material is earlier determined to be the most efficient material.

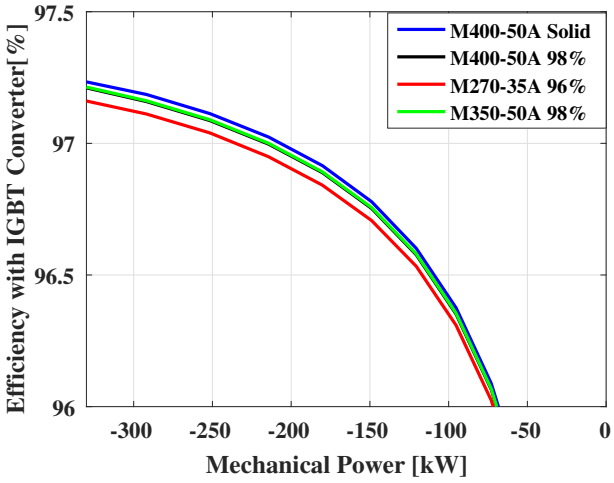

Figure 7.15: Efficiency comparison of the different stacking factors for different steel materials IPM generators

Figure 7.16 shows the annual energy production and loss of the different stacking factor lamination designs. It can be seen that the lowest energy loss is achieved by the solid electrical steel, however it is not possible to apply an infinitely thin layer of coating, therefore the best operation from an energy efficiency point of view is achieved by the M350-50A material with 98% SF.

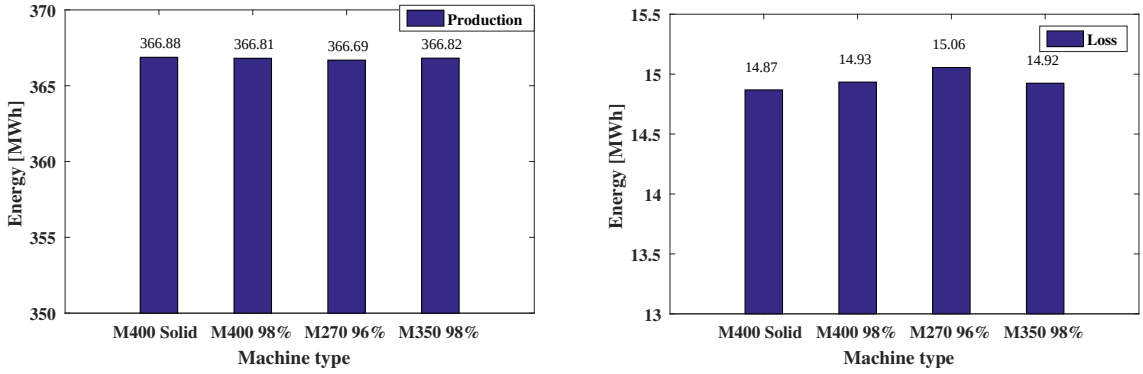

(a) Production

(b) Losses

Figure 7.16: Annual energy production and losses for the different stacking factors for different steel materials IPM generators.

7.4 Effect of the Stator Slot Height

In this section, the effect of the stator slot dimensioning is investigated. The slots height is increased and decreased by 25% and 10%. The airgap and outer radius is kept constant, meaning that the stator yoke is adjusted to accommodate the slot height variations. Figure 7.17a shows the torque-speed and Figure 7.17b shows the power-speed relation of the different slot geometry designs. The maximum current is kept constant and the coil area is varied with the slot size. It can be seen that decreasing the slot size improves the torque-speed or power-speed relation. Furthermore, 25% bigger slot design has significantly lower maximum torque, which is less than the required torque of the buoy, which results in an insufficient power profile as well. The torque profile of the generator designs can also be translated into the current values, meaning that the lower the rated torque, the higher the rated current in order to achieve the same operating points.

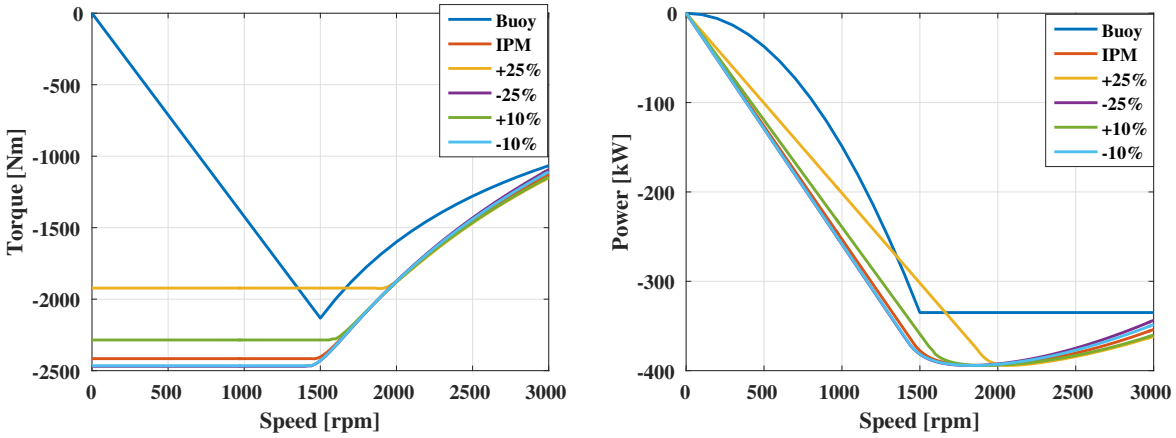

(a) Torque (b) Power

Figure 7.17: Comparison of the electrodynamic torque and the power trajectories for different stator slot heights.

The 25% higher slot design is ruled out due to its insufficient performance. 10% higher and shorter designs, as well as the 25% shorter slot design are used as the WEC generator. Figure 7.18a displays the copper and core losses of the IPM generator with different slot heights and in 7.18b the corresponding total machine and converter losses are shown. When the slot height is increased, the slot area is also increased, therefore the resistance is decreased based on (3.38), and similarly the resistance increases for smaller slot heights.

It can be seen that the 25% smaller slot design has the highest copper losses, since the resistance for this design is the highest amongst the investigated variants. The copper losses however, are increased only by 10% instead of 25%, since the current is decreased for the same torque level, for the 25% slot size. The reduced slot height designs lead to an improved induction, i.e the flux linkage, and thus lower current for the same torque value. Furthermore, this design has the lowest core loss, due to the increased iron area for the stator yoke. For the 10% smaller slot design, the resistance increase is not as drastic and the current is decreased, so

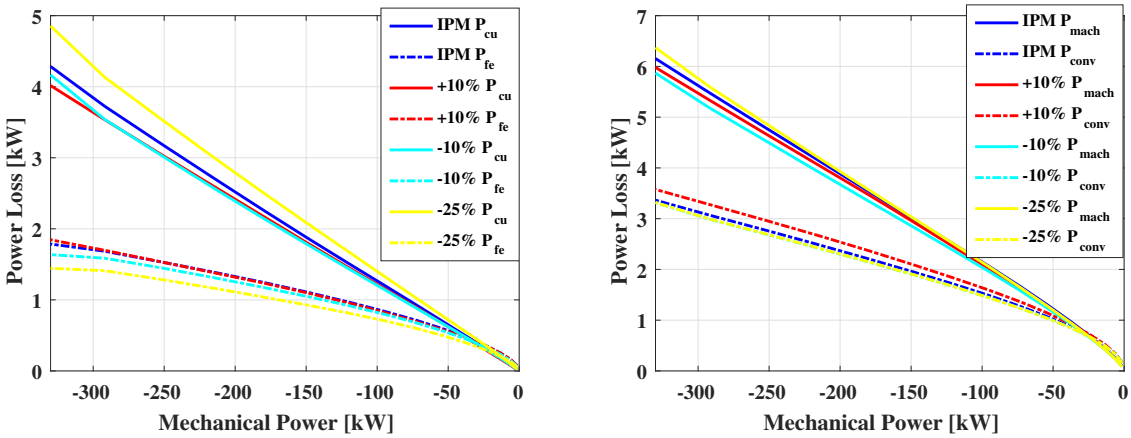

(a) Copper and core losses

(b) Total machine and converter losses

Figure 7.18: Power losses of different slot height designs.

the overall effect on the copper losses is positive, i.e the copper losses are decreased. Similar to the 25% smaller slot case, the core losses are decreased due to the increased stator yoke area.

The full-torque current of the 10% increased slot height case is increased compared to the original design, however the resistance is decreased, therefore the resulting copper losses are decreased. The core losses are increased slightly, due to the smaller stator yoke.

Figure 7.19 shows the comparison of the corresponding efficiencies of the IPM generator variants with different slot sizes. It can be seen that the 10% lower slot height design has the highest efficiency throughout the operation.

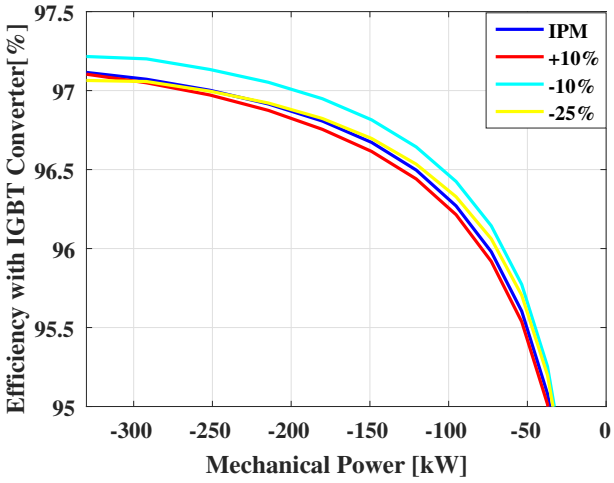

Figure 7.19: Efficiency comparison of different slot height designs

The annual energy productions and losses of the different slot height designs are displayed in 7.20. As expected, the 10% smaller slot height design has the lowest annual energy losses.

Figure 7.21 shows the NPVL comparison between the designs with different slot height

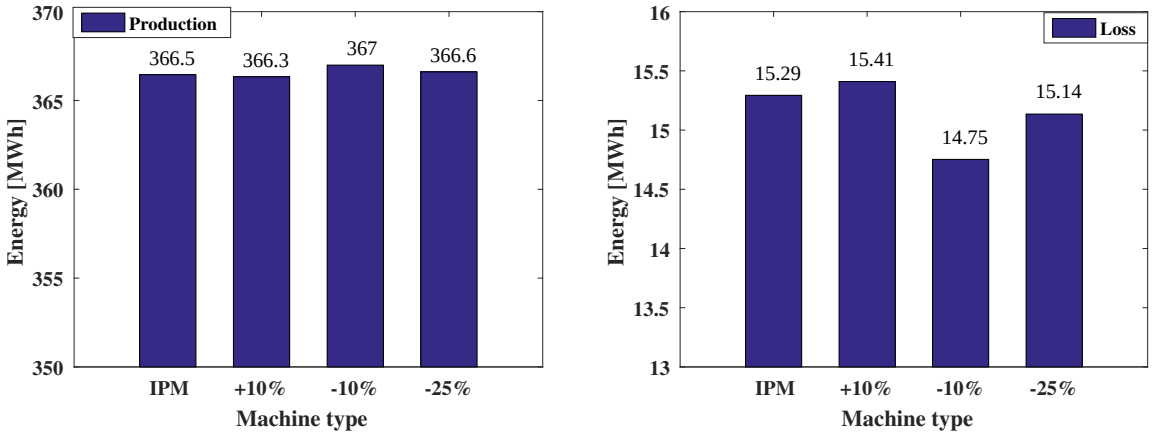

(a) Production (b) Losses

Figure 7.20: Annual energy productions and losses of different slot height designs.

designs. It can be seen that decreasing the slot height by 10% results in a 3900 € decrease in energy loss cost, which corresponds to 4.8%. Furthermore, the investment for the copper wire would also decrease by 10%, which causes the total investment cost to decrease by 3.8%.

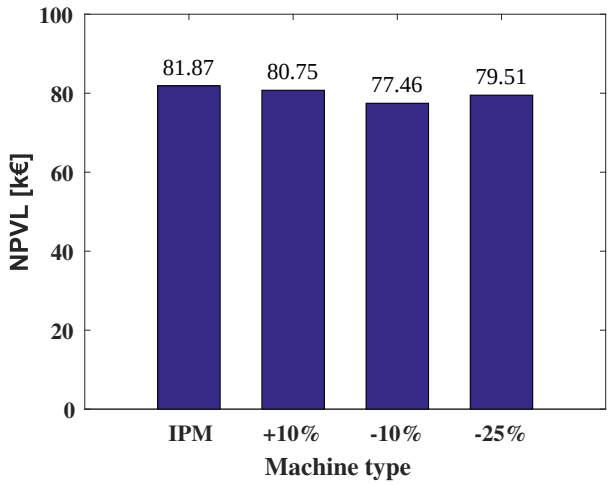

Figure 7.21: NPVL comparison of the WEC generator designs with different slot heights.

7.5 Effect of the Stator Slot Width

In this section, the effect of the slot width on the overall generator performance is investigated. Here the cases of 5% and 10% larger slot widths, as well as the 5% smaller slot width is studied. The fill factor is kept unchanged. The torque-speed relation is depicted in Figure 7.22a and the power-speed relation can be seen in Figure 7.22b.

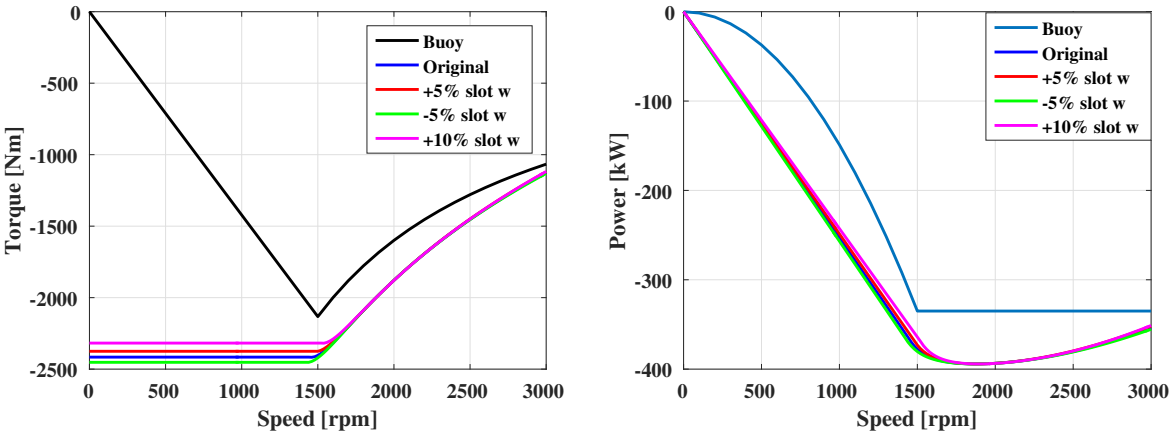

(a) Torque (b) Power

Figure 7.22: Comparison of the electrodynamic torque and the power trajectories for different stator slot widths.

The aforementioned figures show that the power-speed relations of the different slot width designs are significantly similar, as well as the torque-speed relation at the field weakening operating region. Furthermore, it is seen that for the same rated current, the 5% smaller width design has the highest rated torque, followed by the original design and the 5% and 10% wider slot designs, respectively. For the smaller slot width design, the stator teeth width increases. The increased iron area results in a better induction, which means that the 5% smaller slot width design can achieve a higher rated torque for the same maximum current.

Figure 7.23 shows the copper and core losses of the different slot width designs. There is no significant difference between different designs, this is due to the fact that the change in the iron mass of the machine is fairly small in order to accommodate the slot width changes. The copper losses of the studied designs differ more as the speed increases until the rated operating point and the difference is more prominent in the field weakening region. The 5% smaller slot width case only slightly deviates from the copper loss of the original generator, since the maximum current for this design is lower, however the resistance is increased due to the decreased slot area. The rated current is improved only 1.5%, whereas the resistance is increased approximately by 6%. Similarly, despite the current increase for larger slot width designs, the resistance decreases due to the increasing slot area, hence the copper losses are decreased. The 5% wider slot design has an increased rated current of 1.5%, and the resistance is decreased roughly 5.5%. The rated current of the 10% wider slot design is increased by 4%, however the resistance is decreased by 10%. Since the change in resistance is much more drastic than that

of the current, the copper losses are predominantly affected by the resistance for the slot width variations. Using the 10% wider slot design decreases the copper losses by 13% at the rated operating point.

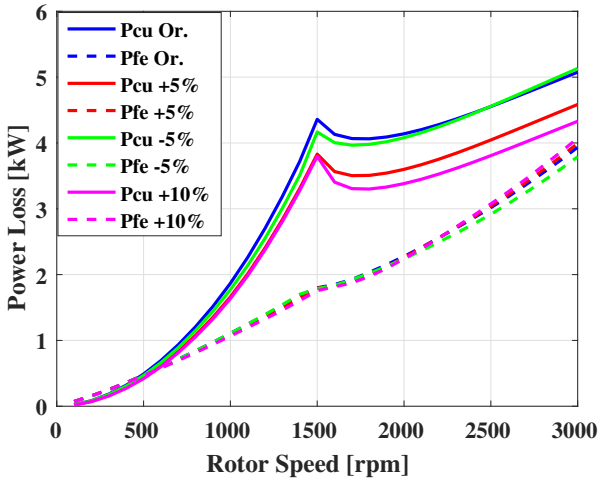

Figure 7.23: Copper and core losses of the different slot width designs.

Figure 7.24 shows the efficiency comparison of the different slot width generator designs. Here, it can be seen that the efficiency of the designs have a strong dependency on the copper losses, and since all designs have lower copper losses than the original design, the efficiencies are as well improved. As expected, the 10% larger slot width design has the highest efficiency.

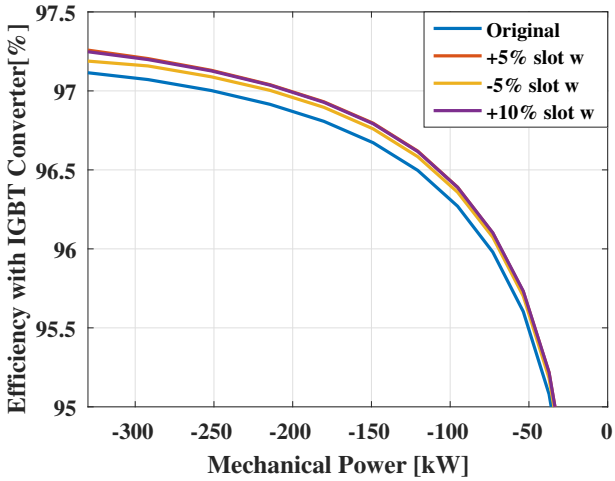

Figure 7.24: Efficiency comparison of different slot width designs

The annual energy productions and losses obtained by using the different slot width generators are depicted in Figure 7.25. The copper loss dependency of the annual energies can be observed in this figure, as the lowest copper loss design, 10% larger slot width, has also the lowest annual energy losses. The difference between the 10% and 5% larger slot width designs

are minuscule, however the annual energy losses decrease approximately by 3.3% if the original slot width is increased by 10%.

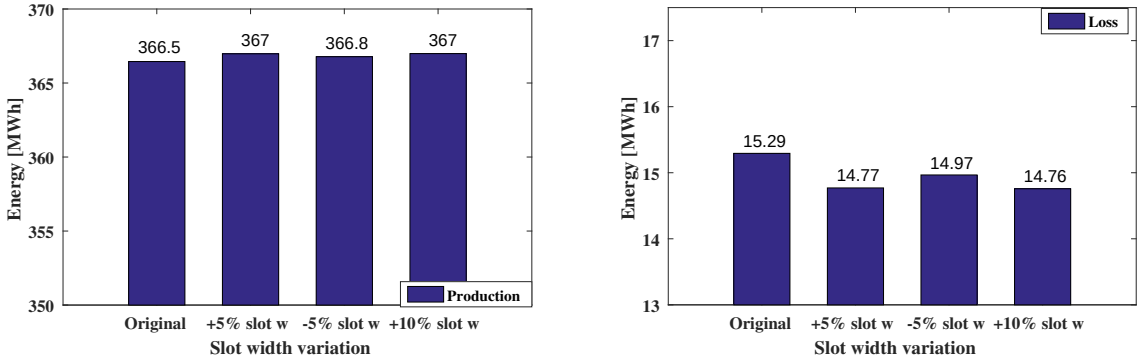

(a) Production (b) Losses

Figure 7.25: Annual energy productions and losses of different slot width designs.

The economical impact of the slot width variations are shown in Figure 7.26. Here, only the NPVL of the studied designs are shown, since investment cost is unchanged. It can be seen that the NPVL of the variations are consistent with the annual energy loss results, as expected. The 10% larger slot width variant decreases the NPVL by 2870 € for the lifetime operation. The investment cost increases due to the increased copper volume, however the difference is only 40 €.

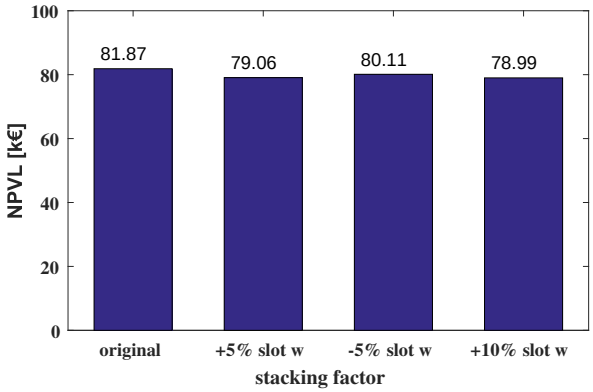

Figure 7.26: NPVL comparison of the WEC generator designs with different slot widths.

7.6 Effect of the Rotor Diameter

In this section, the rotor diameter is increased and decreased by 5 mm. It should be noted that there are several ways to adjust the stator geometry for rotor diameter alterations, and in this work the outer diameter and the stator yoke dimensions are kept unchanged, meaning that the slots are adjusted in order to accommodate the rotor diameter variations. The designs where the stator yoke is altered is not investigated within this project.

The torque and power trajectories as a function of the rotor speed are shown in Figure 7.27. It can be seen that the 5 mm shorter rotor diameter design has the lowest rated torque and the 5 mm longer rotor diameter case has the highest, however the torque obtained using this design is lower for the field weakening operation.

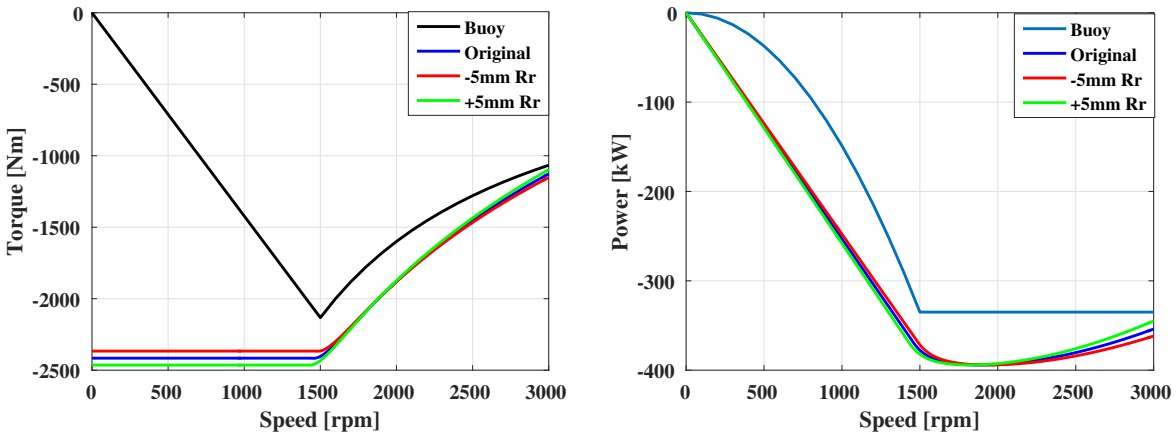

(a) Torque (b) power

Figure 7.27: Comparison of the electrodynamic torque and the power trajectories for different rotor diameter designs.

Figure 7.28 shows the copper and core losses of different rotor diameter designs. It can be seen that while there is no drastic change in the core loss, the copper losses vary significantly. The design with 5 mm shorter rotor diameter has the lowest copper losses, despite that it achieves the rated torque at a higher current, since the resistance of this design is approximately 8% lower than the original generators. During the MTPA operation, the 5 mm longer rotor design has slightly lower copper losses than the original design. This is due to the fact that the lowest rated current of the design, however there is no drastic decrease since the resistance of this design is increased due to the smaller slot area. The copper losses of the longer rotor diameter design is increased during the field weakening operation, due to the decreased rated torque during field weakening.

Figure 7.29 shows the efficiencies of the studied rotor diameter designs. It can be seen that the efficiencies of the generators are predominantly affected by the copper losses. The high copper loss of the longer rotor design at higher rotor speeds does not have a great impact on the efficiency, since the high speed operation seldom occurs.

The resulting annual energy productions and losses are depicted in Figure 7.30. It is seen

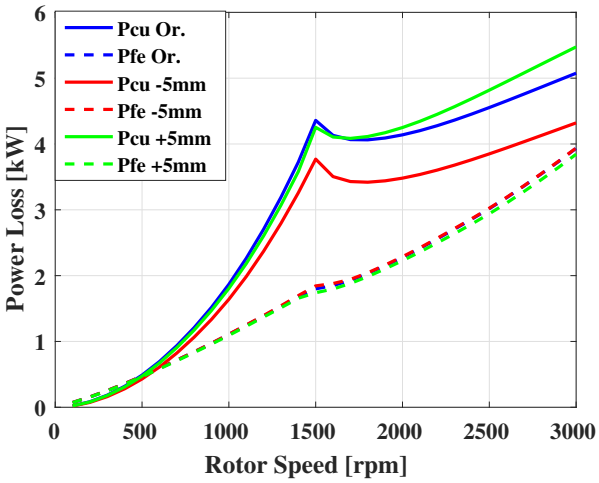

Figure 7.28: Copper and core losses of the different rotor diameter designs.

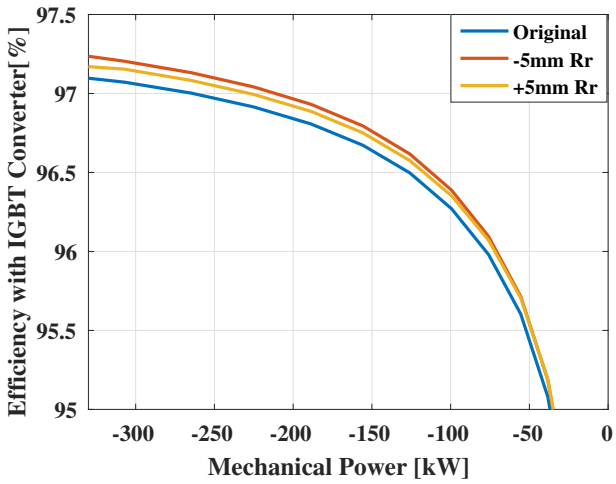

Figure 7.29: Efficiency comparison of different rotor diameter designs.

that using both design instead of the original design results in a decrease in the annual energy losses. The longer rotor diameter case has approximately 2% lower losses and the shorter rotor diameter design improves the energy losses by approximately 3.3%.

The economical impact of different designs are investigated by comparing the NPVL, since the investment costs are unchanged. The results are presented in Figure 7.31. It can be observed that the NPVL of the 5 mm shorter rotor diameter design is 2580 € lower than the original design.

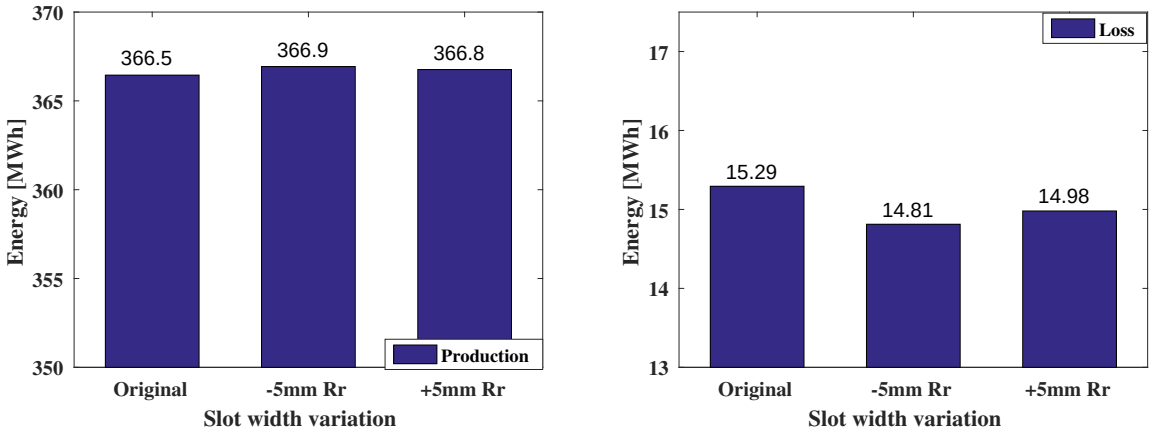

(a) Production (b) Losses

Figure 7.30: Annual energy productions and losses of different rotor diameter designs.

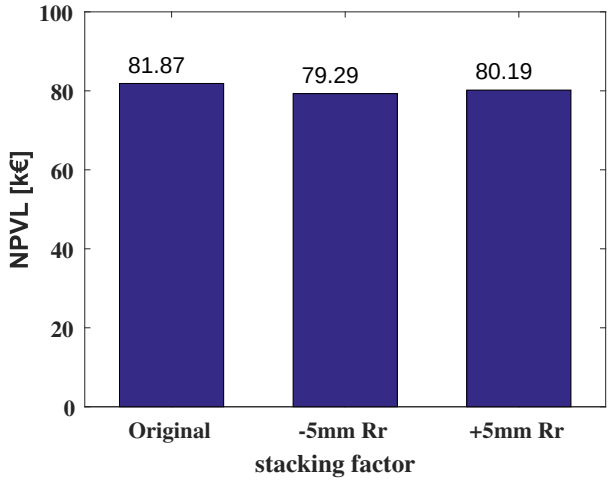

Figure 7.31: NPVL comparison of the WEC generator designs with different rotor diameters.

7.7 SiC MOSFET Converter

The converter losses impact the overall energy losses. In this section, a SiC MOSFET converter is investigated. In this work, a 1700 V module with a current rating of 225 A is selected [67], which has the correct blocking voltage for the application, however the current rating is too low. Therefore, for each half phase leg of the converter, two parallel SiC MOSFET modules are used, in order to be able to operate at the rated generator current. Note that the IGBT modules of the original converter are also selected to have the same voltage and current rating as the SiC MOSFET and two parallel modules are used for each half phase leg, for a better comparison, since a SiC MOSFET converter that could operate for the generator rated current could not be found commercially.

Figure 7.32 shows the components of the converter losses of the IGBT and SiC MOSFET converters. It can be seen that the IGBT converter losses are over 2 times higher than that of the SiC MOSFET converters at the highest power, furthermore all conduction and switching losses of the SiC MOSFET converter are significantly lower than that of the IGBT converter and the diode switching losses are zero for the SiC MOSFET converter. The drastic improvement in the converter losses results in a significant improvement in the system efficiency, as seen in Figure 7.33.

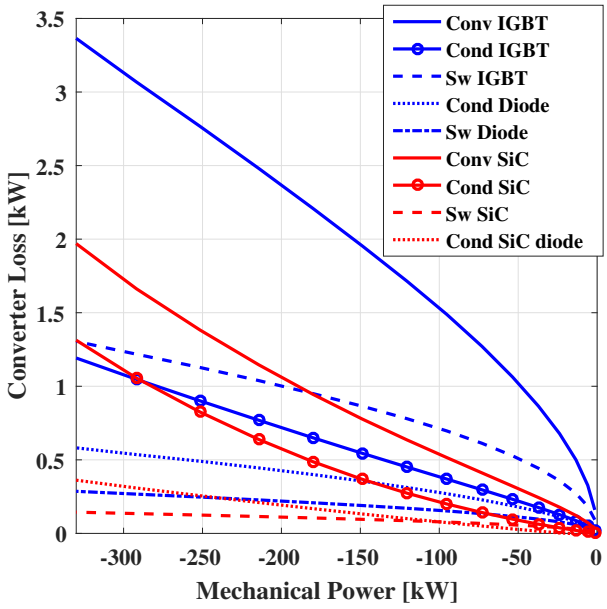

Figure 7.32: Comparison of converter losses for the WEC generating unit using an IGBT and a SiC MOSFET converter

Figure 7.34 shows the energy production and loss of the WEC system with different converters. It can be seen that the annual energy losses of the WEC system decreases by approximately 5 MWh for the SiC MOSFET converter case.

Figure 7.35a shows the investment costs of WEC generation unit using the SiC MOSFET and the IGBT converters. The price of a single IGBT module used in this work is 105 € and the

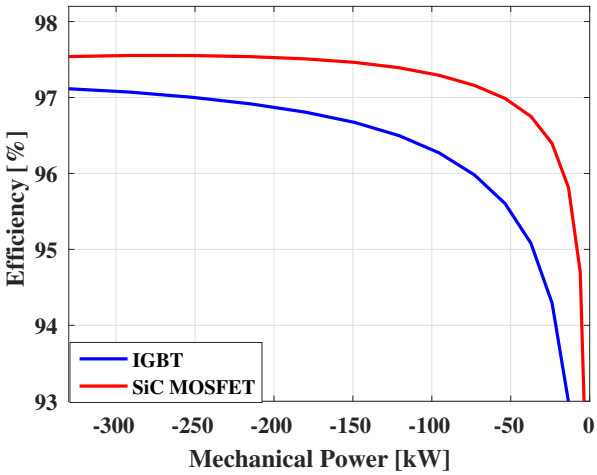

Figure 7.33: Efficiencies of the WEC generating unit using an IGBT and a SiC MOSFET converter

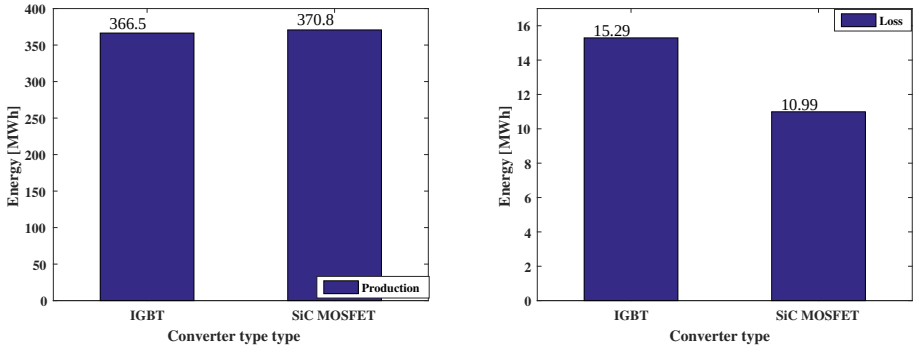

(a) Production (b) Losses

Figure 7.34: Annual energy productions and losses of the WEC generating unit using an IGBT and a SiC MOSFET converter.

price of a single SiC MOSFET module is 730 €[62]. The total IGBT converter price is 1260 €, as previously mentioned and the total SiC MOSFET converter costs 8760 €, since each converter consists of 12 modules. It can be seen that the investment cost of the SiC MOSFET design supersedes the IGBT variant vastly. Figure 7.35b shows the NPVL values for WEC generating systems using IGBT and SiC MOSFET converters.

It can be seen that using the SiC MOSFET converter significantly decreases the NPVL and approximately 23000 € can be saved in energy costs.

Figure 7.36 shows the LCC comparison of the investigated variants. It can be seen that despite the higher investment costs, the SiC MOSFET converter design has a lower LCC, due to its lower annual energy losses.

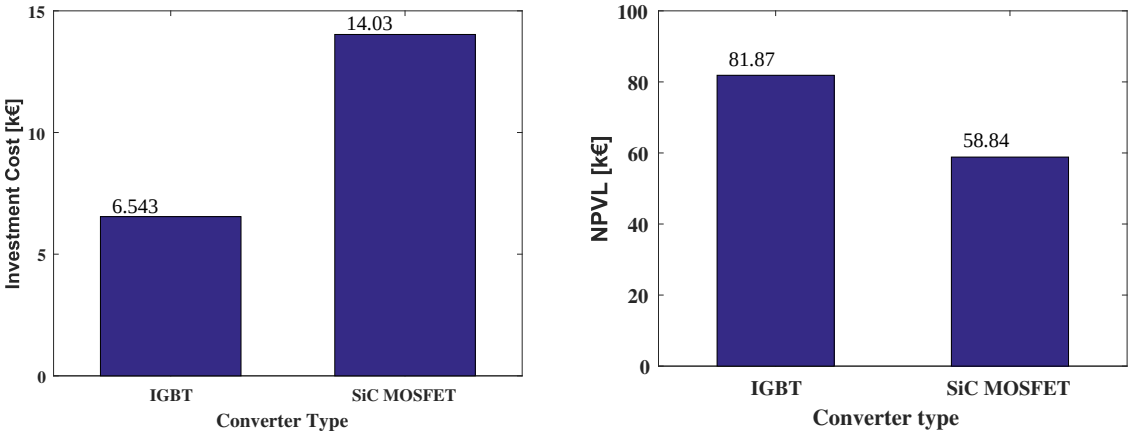

(a) Investment Cost (b) NPVL

Figure 7.35: Semiconductor investment cost and NPVL comparison of the WEC generator designs using IGBT and SiC MOSFET components

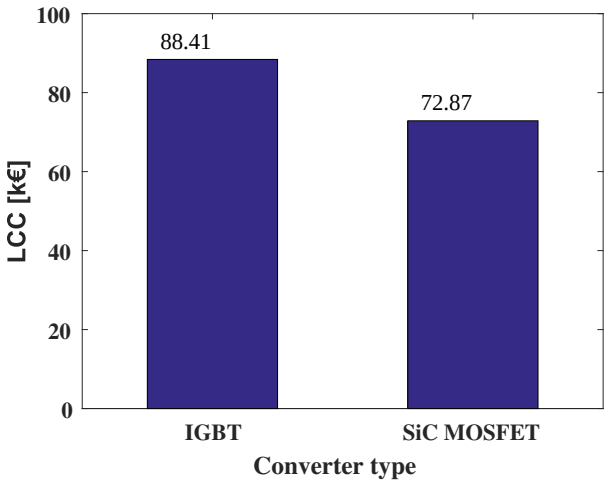

Figure 7.36: LCC comparison of the WEC generator designs using an IGBT and a SiC MOSFET converter.

7.8 Inset Permanent Magnet Generator

Another popular permanent magnet machine design is the inset design. The permanent magnets are placed as in the SMPM, however instead of being placed outside the rotor yoke, they are placed into the groves that are cut out of the rotor yoke. The magnet dimensions are unchanged. The main visible design difference is the iron pieces at the magnet sides. Figure 7.37 shows a cross sectional view of the inset machine.

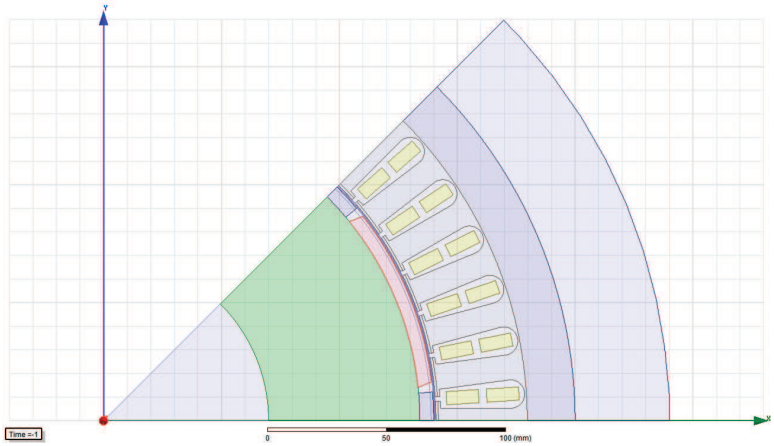

Figure 7.37: Cross sectional view of the inset WEC generator

In this work, four different variations are considered. For three of the variations, the iron side widths are selected as 2^o, 3^o and 5^o arc pieces and the fourth variation has a 5^o arc piece iron side with half the thickness. Figure 7.38a shows the torque-speed comparison of the studied designs. It can be seen that increasing the iron side width increases the maximum torque. Figure 7.38b shows the power variation in relation to the speed. It can be seen that the 5^o iron piece variation not only is the design that can achieve the highest maximum torque, but also that the operation during the field weakening is improved.

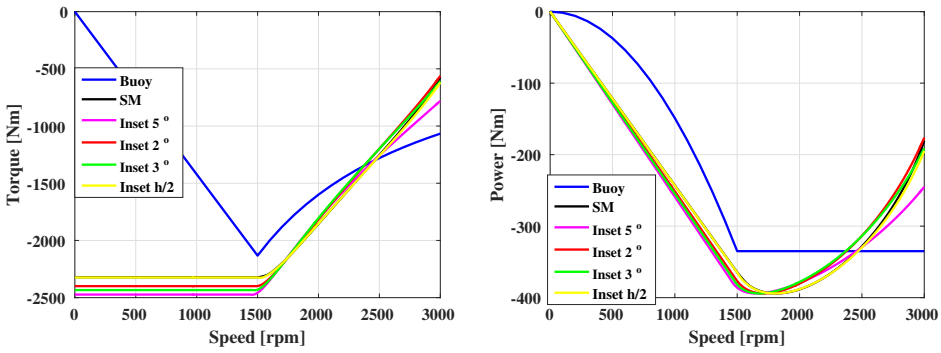

(a) Torque (b) Power

Figure 7.38: Comparison of the torque and power trajectories for different inset designs.

In Figure 7.39, the magnet and reluctance torque comparisons of the 5^o iron side inset vari-

ation and the SMPM generator are shown. It can be observed that the SMPM generator has a very low reluctance torque as expected, since it is a theoretically non-salient machine, and the increased saliency of the inset design causes a reluctance torque increase. However, it can be seen that the magnet torque of the SMPM generator is higher than that of the inset generator, since the inset design uses a higher negative d-current, which reduces the magnet flux linkage.

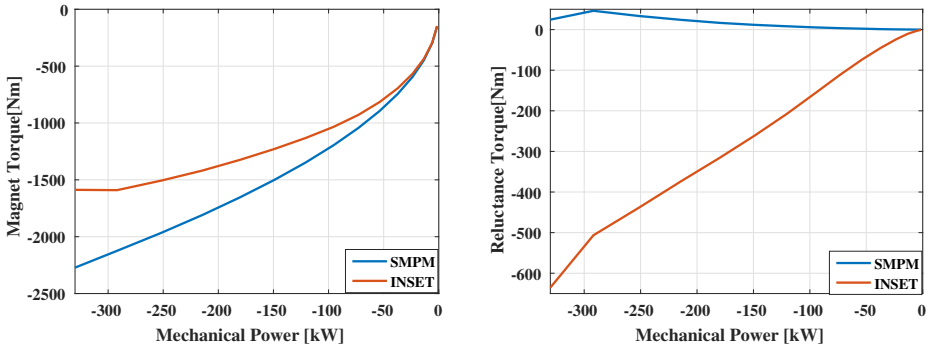

(a) Magnet torque (b) Reluctance torque

Figure 7.39: Comparison of the torque components of different generator designs.

Even though the torque-speed curve seemingly is improved, it does not indicate any clear trend towards the energy production and loss. Figure 7.40a shows the copper and core losses and Figure 7.40b shows the efficiency of the inset design compared to the SMPM generator. It is seen that the inset design has higher core losses than those of the SMPM generator. The SMPM generator has higher copper losses for power levels exceeding 100 kW due to its torque-speed relation, however since the WEC operates often at low power points, it can be seen that the SMPM generator has a higher efficiency than the Inset design.

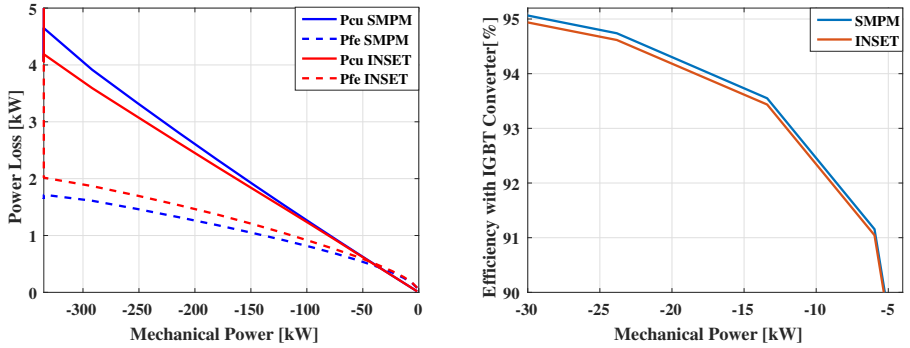

(a) Copper and core losses (b) Efficiency

Figure 7.40: Power loss and efficiency comparisons of the Inset and SMPM generators.

The 5^o iron side design is simulated as the WEC generator and Figure 7.41a shows the energy production, whilst Figure 7.41b shows the energy loss of the previous generators and the inset generator. It can be seen that the inset generator is comparable to the other generators, however, even though the torque-speed curve is improved, due to the power distribution and

the corresponding efficiency, the inset generator has lower energy production than the SMPM generator, which is unexpected, since the inset design has a higher rated torque.

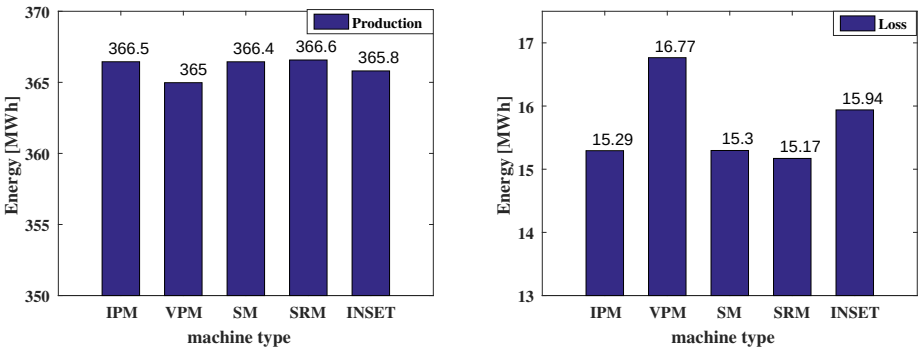

(a) Production (b) Losses

Figure 7.41: Annual energy production and loss of the inset generator compared to the main designs.

Figure 7.42 shows the NPVL of the best performing inset WEC generator design, compared with the four main designs of WEC generators. It can be seen that inset generator has a NPVL of 85.3 k€, which means that the energy losses of this design cost 3440 € more than the default SMPM design. Still, the inset design has a lower NPVL than the VPM generator.

The investment costs of the two generators are equal, since they have the same stator geometry, the same axial length and the same magnet volume. The LCC is fully dependent on the NPVL. It can be decided that the SMPM generator is the favorable choice between the two investigated machines.

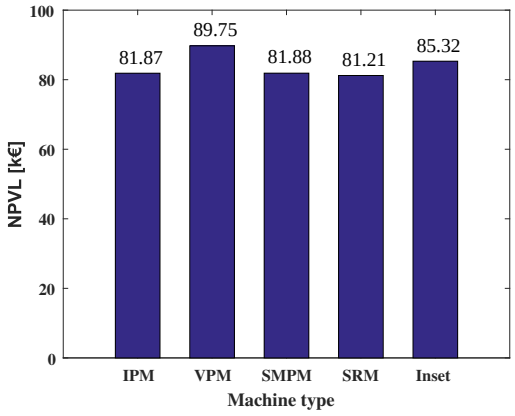

Figure 7.42: NPVL of the selected inset design in comparison with the main designs.

7.9 Ferrite Assisted Synchronous Reluctance Generator

Ferrite is a ceramic compound and it is both non-conductive and ferromagnetic, therefore it can be used as a permanent magnet in electrical machines. The ferrite magnets have a coercivity ranging between 100 -300 kA/m, whereas coercivity of neodymium magnets is 800 - 950 kA/m, therefore the ferrite magnets have a tendency to demagnetize at lower magnetic fields. Furthermore, the magnetic flux output per volume of the ferrite magnets are significantly lower compared with the neodymium magnets, therefore a machine with ferrite magnets has a much lower power density. The ferrite magnet used in this work is a stronium ferrite type, STRO-30-26 and the magnet characteristics can be seen in [68].

The surface mounted and the interior mounted permanent magnet generators rely heavily on the magnet torque, due to their non or low saliency, therefore in order to replace the neodymium magnets with ferrite magnets and achieve a similar performance, the generators need to be much larger. However, since the PM assisted SRM generator is a highly salient design and the reluctance torque component is predominant, the Ferrite assisted SRM does not need to be scaled up as much as the SMPM or the interior mounted variants.

In this work, the Ferrite assisted PM generator is 60% longer in axial length and the number of turns is decreased by one turn in order to lower the max voltage, to fit the converter requirements. The magnet area is increased to circa 685 mm^2. Figure 7.43 shows the no load flux density distribution over the machine cross section. It can be seen that the flux density in the stator teeth is approximately 0.25 T, which is much lower than the neodymium design, due to the lower magnetic flux output of the ferrite magnets.

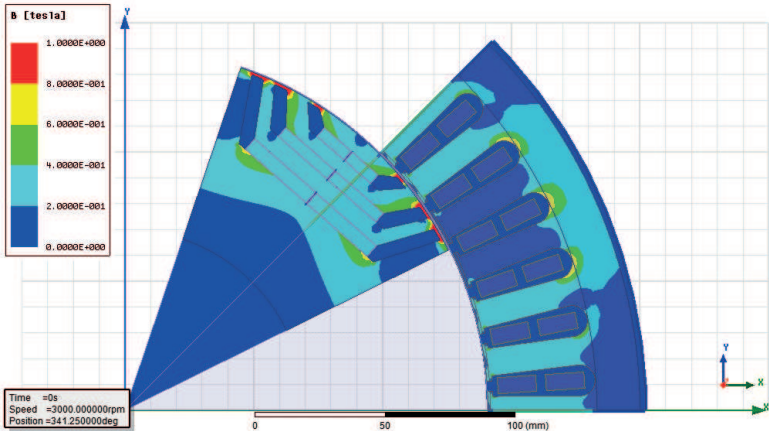

Figure 7.43: No load flux linkage distribution of the Ferrite assisted SRM generator

Figure 7.44 shows the magnet flux linkage in relation to the q-axis current. It can be observed that the no load magnet flux linkage is approximately 4 times lower than the PM assisted SRM generator.

Figure 7.45 shows the current trajectory of the Ferrite assisted SRM generator. It can be observed that similar to the PM variant, the current angle is fairly high, which can be explained through the magnet and reluctance torque comparisons of the designs.

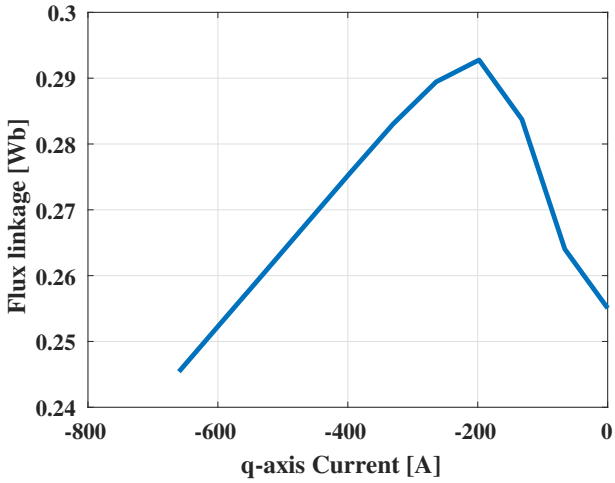

Figure 7.44: Magnet flux linkage of the Ferrite assisted SRM generator

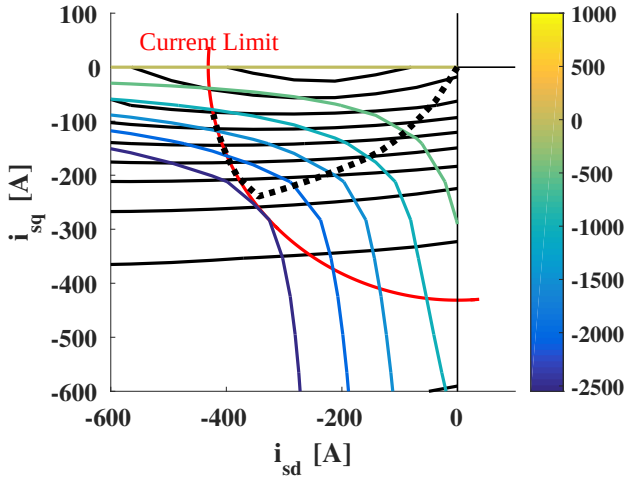

Figure 7.45: Operation diagram of the Ferrite assisted SRM generator

In Figure 7.46b the maximum power trajectories and in Figure 7.46a the maximum torque trajectories of the PM assisted and Ferrite assisted SRM generators, as well as the buoy requirement are displayed. It can be seen that the Ferrite assisted SRM barely achieves the rated torque required, and the field weakening operation starts at a lower speed compared to the PM assisted SRM. As mentioned before, the number of turns of the Ferrite assisted SRM generator is decreased in order to decrease the maximum voltage of the machine, therefore the rated speed is now 1400 rpm instead of 1100 rpm.

The reluctance and magnet torque values of the SRM designs are depicted in Figure 7.47. The magnet torque of the PM assisted SRM is higher than that of the Ferrite assisted variant as seen in 7.47a, since the neodymium magnets have a much better magnetic performance. Since the total electrodynamic torque is dictated by the buoy, the Ferrite assisted generator compensates for the lower magnet torque with a higher reluctance torque value.

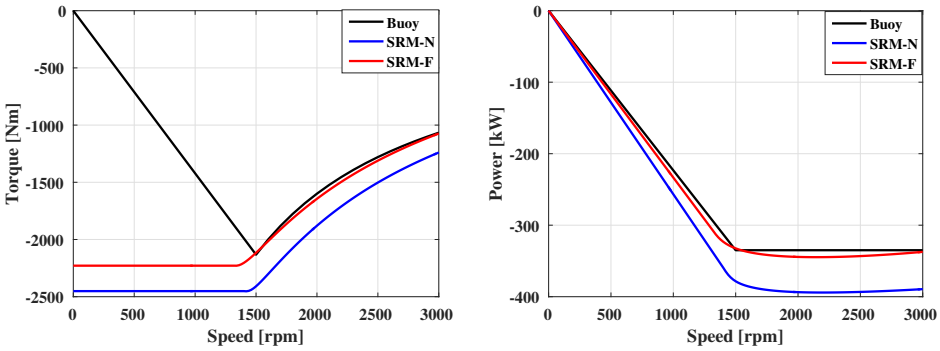

(a) Torque (b) Power

Figure 7.46: Operating range comparison of the PM and Ferrite assisted SRM generators.

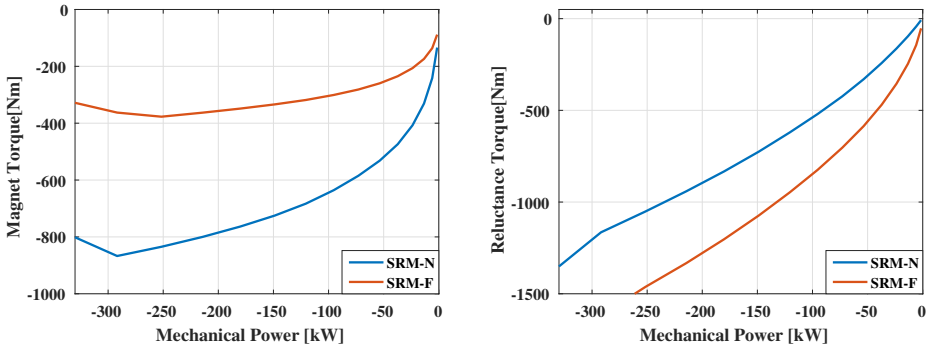

(a) Magnet torque (b) Reluctance torque

Figure 7.47: Comparison of the torque components of the PM and Ferrite assisted SRM Generators.

Figure 7.48a shows the copper and core losses of the Ferrite assisted SRM in comparison with the losses of the PM assisted SRM. The copper loss of the Ferrite assisted SRM is high for low speeds, since the current is higher. For the higher speeds, at field weakening operation, the Ferrite assisted SRM requires less d-axis current since the flux linkage in the machine is already low, and the overall current is lower, compared to the PM assisted SRM. This causes the copper losses of the PM assisted generator to be higher than those of the Ferrite assisted design, for higher speeds. The Ferrite assisted SRM has higher core loss value, since the longer axial length of the generator increases the iron volume of the machine. The fact that the fundamental flux linkage being lower for the Ferrite assisted design does not help, since the core losses are to a great extent caused by the harmonics. Figure 7.48b shows the efficiencies of the Ferrite and PM assisted SRM generators. It can be seen that the Ferrite assisted SRM generator has a lower efficiency compared to the PM assisted design, however the Ferrite assisted machine operates fairly efficiently despite the significantly lower magnet flux linkage.

Figure 7.49 shows the annual energy production and the losses of the Ferrite and PM assisted SRM generators. It can be seen that the annual energy losses of the Ferrite variant are over 25% higher.

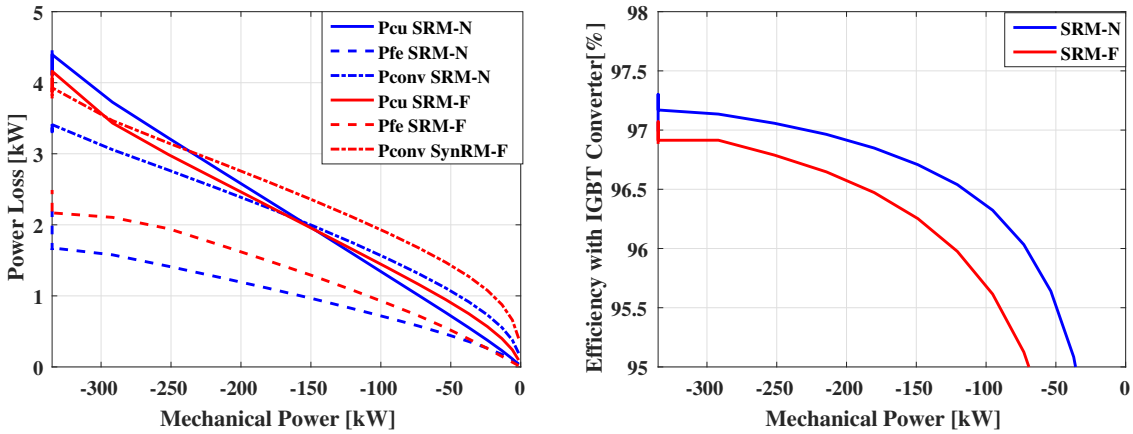

(a) Copper and core losses (b) Power

Figure 7.48: Power loss and efficiency comparisons of the PM and Ferrite assisted SRM generators.

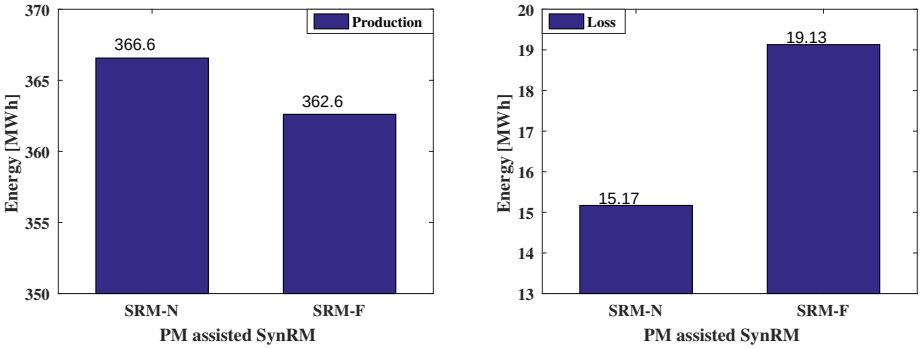

(a) Production (b) Losses

Figure 7.49: Annual energy production and losses of the Ferrite assisted SRM generator.

Figure 7.50a shows the investment cost values of the PM and Ferrite assisted SRM generators. It can be seen that the Ferrite variant costs roughly 500 € more, even though the per unit price of the ferrite magnet is much less the neodymium price, since the Ferrite assisted SRM generator is 60% longer in axial direction which increases the total volume of all materials. Figure 7.50b presents the NPVL comparison of the PM and Ferrite assisted SRM generators. It is once more seen that the lower energy losses results in a lower NPVL value. Here, the NPVL of the PM assisted SRM generator is approximately 80 k€ and the NPVL for the Ferrite variant is circa 100 k€, which means using the PM assisted SRM generator decreases the NPVL of the WEC generation system by 20%.

Figure 7.51 shows the results of the LCC analysis for the PM and Ferrite assisted SRM generators. It can be seen that even though the investment costs of the generators differ, the LCC is still predominantly dependent on the NPVL. Here, the LCC of the PM assisted SRM is again circa 20% lower, as the NPVL, since the investment cost is very small compared to

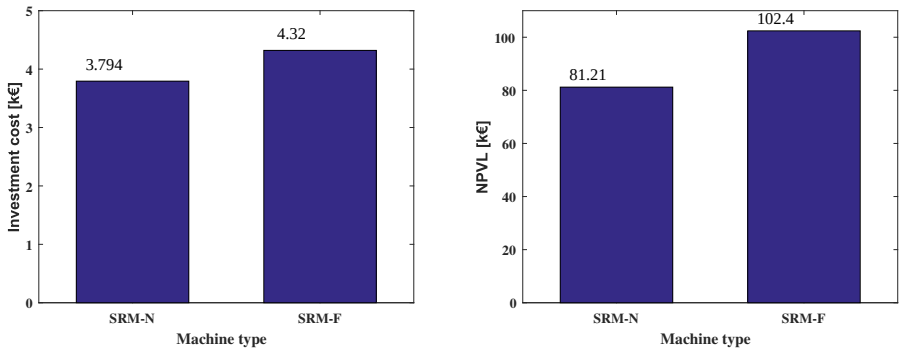

(a) Production (b) Losses

Figure 7.50: Investment cost and NPVL comparisons of the PM and Ferrite assisted SRM Generators.

the NPVL, therefore it does not impact the LCC significantly. To sum up, the Ferrite assisted SRM cannot compete with the neodymium magnet equipped variant for the studied wave energy application.

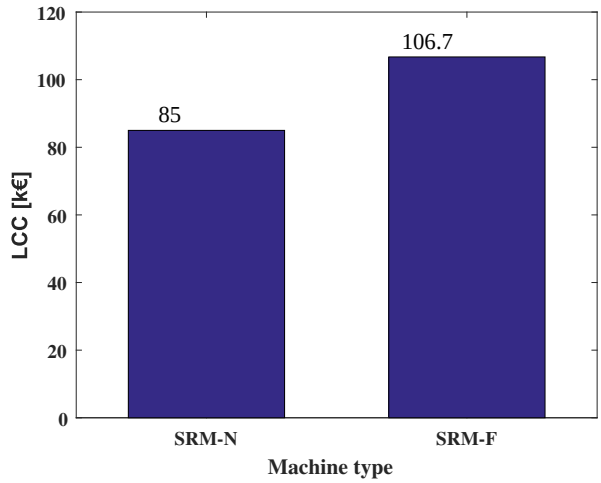

Figure 7.51: LCC comparison of the PM and Ferrite assisted SRM Generators.

Chapter 8

Conclusions and Future Work

8.1 Conclusions

In this work, several WEC generator variants using different permanent magnet rotor topologies and design alterations regarding these topologies are investigated. The aim of the investigation is to understand the effect of the studied designs and alterations on the generator performance. The economical impact of the different generator performances are quantified using LCC analysis and compared, in order to assess the favorable design, within each investigation.

The available wave energy is obtained using spectral analysis and the extracted wave energy is determined through hydrodynamic simulations. Due to their low probabilities and high power levels that require a large PTO, sea states with a H_s higher than 3.75 m are omitted from the available energy calculations. The omitted sea states account for approximately 10% total available wave energy. Furthermore, the highest peak power values of the irregular waves are over 10 times the average power for a given sea state, therefore a limitation for the high power peaks is introduced in order to limit the generator size. The power curtailment level is selected to be 335 kW, which results in a 7.5% loss of the extracted energy, and this value is the rated power of the WEC generator.

IPM, VPM, SMPM and PM assisted SRM generators are designed based on the 335 kW rated power, and the machine performances are compared. It is found that the VPM generator has the poorest performance for this application and the PM assisted SRM has the highest energy efficiency. Moreover, using the PM assisted generator instead of the default IPM design decreases the annual energy losses from 15 MWh to 14.86 MWh, which causes a 660 € decrease in the LCC. The annual energy losses of an inset generator design based on the SMPM generator, are increased 600 kWh, compared to the SMPM generator. Similarly, the WEC unit with a Ferrite assisted SRM generator, that is scaled up to deliver the rated power, has 30% increased annual energy losses.

Regarding the iron material of the generators, the best energy performance is achieved using the lamination material M350-50A, which is also undoubtedly the favorable design economically. This is due to the fact that the second best performance is achieved for the M270-35A

material, which is suspected to have a higher purchase price due to its lowered thickness and core losses. An important finding of this investigation points out that the B-H characteristic of the steel lamination has a more prominent impact on the performance compared to the core loss characteristic. Similar findings are obtained for the stacking factor variations, however, since the M270-35A has a lower SF due to its smaller thickness, a better performance when using the M350-50A material with 98% SF is obtained. The annual energy loss is improved by 2.7% when the M350-50A is used instead of the M270-35A and when the stacking factors are taken into consideration the improvement is roughly 9%, for the same comparison.

Another material investigation is done in order to assess the use of cobalt-iron material. It is concluded that due to its high core losses, the cobalt-iron is not preferred in the stator. The high core loss characteristic of this material however, does not result in a significant increase when used only for rotor construction, since the flux in the rotor yoke mainly is a DC flux. The machine with the cobalt-iron rotor has better performance than the original design, which lowers the annual energy losses by 1.5%, however the investment cost of the cobalt-iron rotor design is more than twice the cost of the original generator, which increases the LCC by 7 k€.

A study on the stator design investigates the effect of the stator slot size on the LCC of the WEC generator. The slot height is increased and decreased by 25% and 10%, and the results dictate that the 10% lower slot height design has the best energy efficiency. Using this variant, the annual energy losses decrease by 4.8%, furthermore the investment cost of the generator decreases due to the lowered copper volume, which results in a 200 € lower investment costs. Furthermore, increasing the slot width by 10% results in a 3.3% decrease in the annual energy losses.

The converter losses of the IGBT converter is comparable to the copper losses at the rated power operation. In order to increase the WEC generation unit efficiency, the converter losses can be improved. In this work, when a SiC MOSFET based converter replaces the default IGBT converter, the converter losses are drastically lowered. The annual energy losses of the WEC are decreased by 30%. Despite the investment cost being several times higher when using a SiC MOSFET instead of an IGBT converter, the LCC of the WEC that is equipped with the SiC MOSFET converter is decreased significantly.

To sum up, the favorable machine out of the main four designs is the PM assisted SRM and the most significant improvement is caused by using a SiC MOSFET based converter. The highest LCC is obtained when using the Ferrite assisted SRM. The LCC throughout the work ranges between circa 70 k€ to 106 k€. The cobalt-iron investigation presents that some alterations that improve the energy efficiency, might be a poorer choice from an economical point of view. To conclude, an economical assessment of the performance variation when evaluating different generator designs is crucial, in order to gauge the impact of the energy variations on the life cycle cost of the system and therefore select a favorable generator.

8.2 Future Work

A valuable continuation to the work would be to investigate some of the studied design alterations by using finer steps, such as the stator slot height and width cases and different rotor diameter designs. It is also interesting to perform a systematic optimization, using for instance genetic algorithms and investigate how the findings tie in with the results of this work. Further investigation regarding the generator size, mainly obtaining an ideal stack length-outer diameter ratio depending on the primary objective of the optimization would provide valuable findings.

To establish the economical consequences of using rectangular hair pin windings instead of round wires as well as quantifying the impact of the skin effect would be a significant contribution, both regarding the active part of the machine and the end-winding size. Furthermore, for applications where the machine size is limited, studying the thermal limitations would prove useful.

An important issue with FEM based investigation is that the core losses are usually too low, since the punching effects are not taken into consideration. A method that accounts for the material degradation is an interesting subject to further study. To perform verifying measurements is always an important task, however, here it would be important to find a special feature to validate, in case a machine is build and subjected to a measurement campaign. A further study regarding the demagnetization risk, in particular the ferrite magnet designs would provide important findings.

The WEC generators are selected to be radial flux machines in this project, however, other flux path machines such as the axial flux and transversal flux machines, as well as other concepts such as the electrically magnetized machine, switched reluctance and the induction machine are worthy to be investigated. Furthermore, another permanent magnet rotor topology, the spoke generator, is worth looking into.

One of the important findings of this work was that the power electronic converter has a significant impact on the machine performance. Studying the energy efficiency and the economical evaluation of the multilevel inverters, such as the Neutral Point Clamped (NPC) and Modular Multilevel Converter (MMC) would provide insightful results.

Here, the economical investigation focused only on the electric drive of a WEC and is performed using the LCC method. An important work to conduct is the investigating the full WEC system that consists of the hydrodynamic and mechanical parts. Even though the electrical system efficiency is worth optimizing, optimizing the point absorber can increase the efficiency of the WEC application substantially. Using a reactive power control of the buoy is a highly interesting possibility, as mentioned in [15], the energy gain can be increased. The obvious challenge regarding wave energy is the high costs of the PTO and PTO suspension systems. Further study upon these subjects in order to effectively reduce the WEC system costs can lead to a break-through for the future wave energy applications.

References

[1] "2020 energy strategy," https://ec.europa.eu/energy/en/topics/energy-strategy-and-energy-union/, accessed: 2018-02-18.

[2] P. Meisen and T. Hammons, "Harnessing the untapped energy potential of the oceans: tidal, wave, currents and otec," in *IEEE Power Engineering Society General Meeting, 2005*, June 2005, pp. 1853–1854.

[3] A. Clément, P. McCullen, A. F. ao, A. Fiorentino, F. Gardner, K. Hammarlund, G. Lemonis, T. Lewis, K. Nielsen, S. Petroncini, M. Pontes, P. Schild, and B.-O. Sj "Wave energy in europe: current status and perspectives," *Renewable and Sustainable Energy Reviews*, vol. 6, no. 5, pp. 405 – 431, 2002. [Online]. Available: http://www.sciencedirect.com/science/article/pii/S1364032102000096

[4] J. G. Vining and A. Muetze, "Economic factors and incentives for ocean wave energy conversion," *IEEE Transactions on Industry Applications*, vol. 45, no. 2, pp. 547–554, March 2009.

[5] A. Pecher and J. Kofoed, *Handbook of Ocean Wave Energy*, ser. Ocean Engineering & Oceanography. Springer International Publishing, 2017.

[6] T. Thorpe, "The wave energy programme in the uk and the european wave energy network," pp. 19–72, 2000.

[7] M. A. Mueller, H. Polinder, and N. Baker, "Current and novel electrical generator technology for wave energy converters," in *2007 IEEE International Electric Machines Drives Conference*, vol. 2, May 2007, pp. 1401–1406.

[8] M. Leijon, R. Waters, M. Rahm, O. Svensson, C. Bostrom, E. Stromstedt, J. Engstrom, S. Tyrberg, A. Savin, H. Gravrakmo, H. Bernhoff, J. Sundberg, J. Isberg, O. Agren, O. Danielsson, M. Eriksson, E. Lejerskog, B. Bolund, S. Gustafsson, and K. Thorburn, "Catch the wave to electricity," *IEEE Power and Energy Magazine*, vol. 7, no. 1, pp. 50–54, January 2009.

[9] A. V.-W. M. C. S. B. R. B. M. Hannon, J. Griffiths and S. Wyatt, "World energy resources marine energy 2016," 2016.

[10] D. Kavanagh, A. Keane, and D. Flynn, "Capacity value of wave power," *IEEE Transactions on Power Systems*, vol. 28, no. 1, pp. 412–420, Feb 2013.

[11] K. U. Amann, M. E. Magana, and O. Sawodny, "Model predictive control of a nonlinear 2-body point absorber wave energy converter with estimated state feedback," *IEEE Transactions on Sustainable Energy*, vol. 6, no. 2, pp. 336–345, April 2015.

[12] M. Trapanese, "Optimized design of a sea wave energy conversion system," in *2008 34th Annual Conference of IEEE Industrial Electronics*, Nov 2008, pp. 2051–2054.

[13] S. Tyrberg, O. Svensson, V. Kurupath, J. Engstrom, E. Stromstedt, and M. Leijon, "Wave buoy and translator motions - on-site measurements and simulations," *IEEE Journal of Oceanic Engineering*, vol. 36, no. 3, pp. 377–385, July 2011.

[14] A. Bozzetto and E. Tedeschi, "Wave power extraction with constrained power take-off: Single capture vs. double capture point absorbers," in *2014 Ninth International Conference on Ecological Vehicles and Renewable Energies (EVER)*, March 2014, pp. 1–7.

[15] E. Tedeschi and M. Molinas, "Tunable control strategy for wave energy converters with limited power takeoff rating," *IEEE Transactions on Industrial Electronics*, vol. 59, no. 10, pp. 3838–3846, Oct 2012.

[16] E. Enferad and D. Nazarpour, "Implementing double fed induction generator for converting ocean wave power to electrical," in *4th Annual International Power Electronics, Drive Systems and Technologies Conference*, Feb 2013, pp. 448–453.

[17] K. Yuen, K. Thomas, M. Grabbe, P. Deglaire, M. Bouquerel, D. Osterberg, and M. Leijon, "Matching a permanent magnet synchronous generator to a fixed pitch vertical axis turbine for marine current energy conversion," *IEEE Journal of Oceanic Engineering*, vol. 34, no. 1, pp. 24–31, Jan 2009.

[18] P. Roshanfekr, T. Thiringer, M. Alatalo, and S. Lundmark, "Performance of two 5 mw permanent magnet wind turbine generators using surface mounted and interior mounted magnets," in *2012 XXth International Conference on Electrical Machines*, Sept 2012, pp. 1041–1047.

[19] G. Pellegrino, A. Vagati, P. Guglielmi, and B. Boazzo, "Performance comparison between surface-mounted and interior pm motor drives for electric vehicle application," *IEEE Transactions on Industrial Electronics*, vol. 59, no. 2, pp. 803–811, Feb 2012.

[20] J. Dong, Y. Huang, L. Jin, and H. Lin, "Comparative study of surface-mounted and interior permanent-magnet motors for high-speed applications," *IEEE Transactions on Applied Superconductivity*, vol. 26, no. 4, pp. 1–4, June 2016.

[21] A. Wang, Y. Jia, and W. L. Soong, "Comparison of five topologies for an interior permanent-magnet machine for a hybrid electric vehicle," *IEEE Transactions on Magnetics*, vol. 47, no. 10, pp. 3606–3609, Oct 2011.

[22] L. Guo and L. Parsa, "Effects of magnet shape on torque characteristics of interior permanent magnet machines," in *2009 IEEE Electric Ship Technologies Symposium*, April 2009, pp. 93–97.

[23] P. Roshanfekr, S. Lundmark, T. Thiringer, and M. Alatalo, "A synchronous reluctance generator for a wind application-compared with an interior mounted permanent magnet synchronous generator," in *7th IET International Conference on Power Electronics, Machines and Drives (PEMD 2014)*, April 2014, pp. 1–5.

[24] P. Roshanfekr, S. T. Lundmark, T. Thiringer, and M. Alatalo, "Comparison of a 5mw permanent magnet assisted synchronous reluctance generator with an ipmsg for wind application," in *2014 International Conference on Electrical Machines (ICEM)*, Sept 2014, pp. 711–715.

[25] R. Leuzzi, P. Cagnetta, F. Cupertino, S. Ferrari, and G. Pellegrino, "Performance assessment of ferrite- and neodymiumassisted synchronous reluctance machines," in *2017 IEEE Energy Conversion Congress and Exposition (ECCE)*, Oct 2017, pp. 3958–3965.

[26] T. K. A. Brekken, H. M. Hapke, C. Stillinger, and J. Prudell, "Machines and drives comparison for low-power renewable energy and oscillating applications," *IEEE Transactions on Energy Conversion*, vol. 25, no. 4, pp. 1162–1170, Dec 2010.

[27] Q. Chen, G. Liu, L. Sun, Y. Jiang, and J. Yang, "Comparison of five topologies rotor permanent magnet motors with improved fault-tolerance," in *2013 IEEE International Symposium on Industrial Electronics*, May 2013, pp. 1–5.

[28] H. Li, L. Qu, and W. Qiao, "Life-cycle cost analysis for wind power converters," in *2017 IEEE International Conference on Electro Information Technology (EIT)*, May 2017, pp. 630–634.

[29] A. Rassolkin, S. Orlova, T. Vaimann, A. Belahcen, and A. Kallaste, "Environmental and life cycle cost analysis of a synchronous reluctance machine," in *2016 57th International Scientific Conference on Power and Electrical Engineering of Riga Technical University (RTUCON)*, Oct 2016, pp. 1–5.

[30] G. Dalton, D. Madden, and M. C. Daly, "Life cycle assessment of the wavestar," in *2014 Ninth International Conference on Ecological Vehicles and Renewable Energies (EVER)*, March 2014, pp. 1–9.

[31] A. Têtu, *Power Take-Off Systems for WECs*. Cham: Springer International Publishing, 2017, pp. 203–220. [Online]. Available: https://doi.org/10.1007/978-3-319-39889-1_8

[32] A. Sproul and N. Weise, "Analysis of a wave front parallel wec prototype," *IEEE Transactions on Sustainable Energy*, vol. 6, no. 4, pp. 1183–1189, Oct 2015.

[33] D. L. OFLSullivan and A. W. Lewis, "Generator selection and comparative performance in offshore oscillating water column ocean wave energy converters," *IEEE Transactions on Energy Conversion*, vol. 26, no. 2, pp. 603–614, June 2011.

[34] R. C. Thomson, G. P. Harrison, and J. P. Chick, "Full life cycle assessment of a wave energy converter," in *IET Conference on Renewable Power Generation (RPG 2011)*, Sept 2011, pp. 1–6.

[35] N. Müller, S. Kouro, M. Malinowski, S. Rivera, and B. Wu, "Cascaded h-bridge multilevel converter interface for wave dragon energy conversion system," in *IECON 2013 - 39th Annual Conference of the IEEE Industrial Electronics Society*, Nov 2013, pp. 6201–6206.

[36] N. Müller, S. Kouro, J. GlarÃa, and M. Malinowski, "Medium-voltage power converter interface for wave dragon wave energy conversion system," in *2013 IEEE Energy Conversion Congress and Exposition*, Sept 2013, pp. 352–358.

[37] M. Prado and H. Polinder, "Direct drive in wave energy conversion - aws full scale prototype case study," in *2011 IEEE Power and Energy Society General Meeting*, July 2011, pp. 1–7.

[38] H. Polinder, M. E. C. Damen, and F. Gardner, "Linear pm generator system for wave energy conversion in the aws," *IEEE Transactions on Energy Conversion*, vol. 19, no. 3, pp. 583–589, Sept 2004.

[39] H. Polinder, B. C. Mecrow, A. G. Jack, P. G. Dickinson, and M. A. Mueller, "Conventional and tfpm linear generators for direct-drive wave energy conversion," *IEEE Transactions on Energy Conversion*, vol. 20, no. 2, pp. 260–267, June 2005.

[40] N. Daratha, H. Polinder, and M. de Sousa Prado, "A first-order energy storage requirements estimation for an archimedes wave swing park," in *2008 IEEE International Conference on Sustainable Energy Technologies*, Nov 2008, pp. 1161–1165.

[41] "Seabased ab," http://www.seabased.com/en/, accessed: 2017-11-26.

[42] S. Tyrberg, R. Waters, and M. Leijon, "Wave power absorption as a function of water level and wave height: Theory and experiment," *IEEE Journal of Oceanic Engineering*, vol. 35, no. 3, pp. 558–564, July 2010.

[43] M. Leijon, O. Danielsson, M. Eriksson, K. Thorburn, H. Bernhoff, J. Isberg, J. Sundberg, I. Ivanova, E. Sjostedt, O. Agren, K. Karlsson, and A. Wolfbrandt, "An electrical approach to wave energy conversion," *Renewable Energy*, vol. 31, no. 9, pp. 1309 – 1319, 2006. [Online]. Available: http://www.sciencedirect.com/science/article/pii/S0960148105002120

[44] O. S. E. Strömstedt, A. Savin and M. Leijon, "Time series-, time-frequency- and spectral analyses of sensor measurements in an offshore wave energy converter based on linear generator technology," pp. 70–91, 2013.

[45] J. Newman, *Marine Hydrodynamics*. Wei Cheng Cultural Enteroprise Company, 1977.

[46] L. Bergdahl, *Wave-Induced Loads and Ship Motions*. Chalmers University of Technology, 2010.

[47] L. Holthuijsen, *Waves in Oceanic and Coastal Waters*. Cambridge University Press, 2010.

[48] A. Babarit and J. Hals, "On the maximum and actual capture width ratio of wave energy converters," in *Ninth European Wave and Tidal Energy Conference, Southampton, UK*, 2011, pp. 1–7.

[49] L. Harnefors, *Control of variable-speed drives*. Västerås: Applied Signal Processing and Control, Department of Electronics, Mälardalen University, 2002.

[50] J. Härsjö, *Modeling of PMSM Full Power Converter Wind Turbine with Turn-To-Turn Fault*. Institutionen för energi och miljö, Chalmers tekniska högskola.

[51] J. Hendershot and T. Miller, *Design of Brushless Permanent-magnet Machines*. Motor Design Books, 2010.

[52] Semikron, *Theory of Loss and Temperature Calculation*, 2011.

[53] O. Josefsson, *Energy Efficiency Comparison Between Two-level and Multilevel Inverters for Electric Vehicle Applications*. Institutionen för energi och miljö, Chalmers tekniska högskola.

[54] A. Acquaviva and T. Thiringer, "Energy efficiency of a sic mosfet propulsion inverter accounting for the mosfet's reverse conduction and the blanking time," in *2017 19th European Conference on Power Electronics and Applications (EPE'17 ECCE Europe)*, Sept 2017, pp. P.1–P.9.

[55] P. Tokat and T. Thiringer, "Sizing of ipm generator for a single point absorber type wave energy converter," *IEEE Transactions on Energy Conversion*, vol. PP, no. 99, pp. 1–1, 2017.

[56] "Cogent, a tata steel enterprise," https://cogent-power.com/, accessed: 2017-12-16.

[57] "Neodymium-iron-boron magnets neomax series," http://www.hitachi-metals.co.jp/, accessed: 2017-12-16.

[58] "Infineon, ff225r17me4," https://www.infineon.com/cms/en/product/power/igbt/igbt-modules/igbt-modules-up-to-1600v-1700v/ff225r17me4/.

[59] P. Tokat, *Design and Evaluation of a Permanent Magnet Generator for Wave Power Applications*. Institutionen för energi och miljö, Chalmers tekniska högskola.

[60] M. Bali and A. Muetze, "The degradation depth of electrical steel sheets due to mechanical and laser cutting," in *2017 IEEE 11th International Symposium on Diagnostics for Electrical Machines, Power Electronics and Drives (SDEMPED)*, Aug 2017, pp. 544–549.

[61] M. Bali, H. D. Gersem, and A. Muetze, "Determination of original nondegraded and fully degraded magnetic characteristics of material subjected to laser cutting," *IEEE Transactions on Industry Applications*, vol. 53, no. 5, pp. 4242–4251, Sept 2017.

[62] "Digi - key electronics," http://www.digikey.com/en/, accessed: 2017-12-16.

[63] “Nord pool,” https://www.nordpoolgroup.com/.

[64] “Vacuumschmelze,” http://www.vacuumschmelze.com, accessed: 2017-12-11.

[65] “Emetor,” https://www.emetor.com/blog/post/rule-thumb-calculating-stacking-factor/.

[66] S. T. Lundmark and P. R. Fard, “Two-dimensional and three-dimensional core and magnet loss modeling in a radial flux and a transverse flux pm traction motor,” *IEEE Transactions on Industry Applications*, vol. 53, no. 3, pp. 2028–2039, May 2017.

[67] “Cree, cas300m17bm2,” https://www.wolfspeed.com/cas300m17bm2, accessed: 2017-12-16.

[68] “Hard ferrite magnets,” http://www.magnete.de/uploads/media/kat-hf_en.pdf, accessed: 2017-12-16.

Appendix A

Semiconductor Parameters

The key parameters of the investigated semiconductor components are listed in this chapter.

TABLE A.1: Parameters of Semiconductor Modules

Module type	IGBT	SiC MOSFET
Device Name	Infineon FF225R17ME4	Cree CAS300M17BM2
Blocking Voltage	$1700V$	$1700V$
$I_{C,nom}$	$225A$	$225A$
V_{T0}	0.8	0
R_s	$7.7m\Omega$	$16m\Omega$
E^*_{on}	$105mJ$	$13mJ$
E^*_{off}	$103mJ$	$10mJ$
k_{iT}	1	1
k_{vT}	1.35	1.35
k_{iD}	1	1
k_{vD}	0.6	0.6
T^*_j	150^oC	150^oC
V^*_{ref}, I^*_{ref}	$(900V, 300A)$	$(900V, 300A)$
V_{d0}	$0.8V$	$0.7V$
R_{d0}	$5.8m\Omega$	$5.3m\Omega$
E^*_{swD}	$53mJ$	$0mJ$

Appendix B

Frequency Dependent Hydrodynamic Coefficients

The frequency dependent hydrodynamic parameters, added mass, radiation damping and wave excitation force phase and magnitude are computed using Ansys AQWA, for heave motion. The results are shown in this chapter.

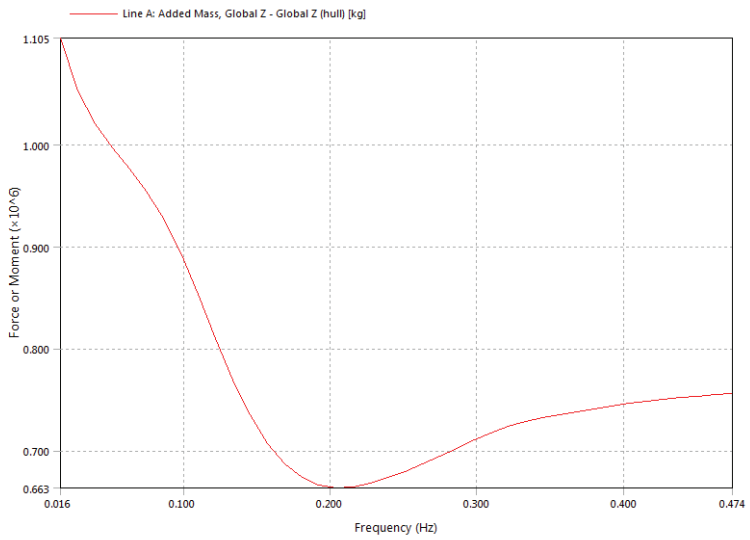

Figure B.1: Heave added mass values for the investigated WEC.

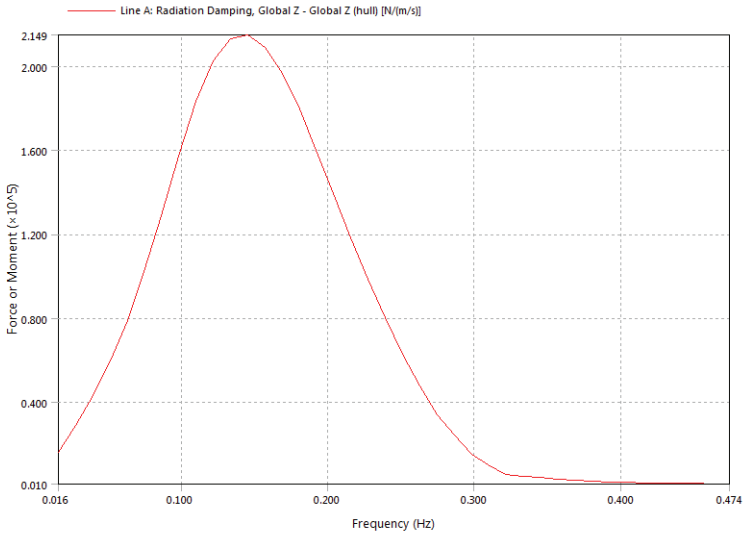

Figure B.2: Heave radiation damping values for the investigated WEC.

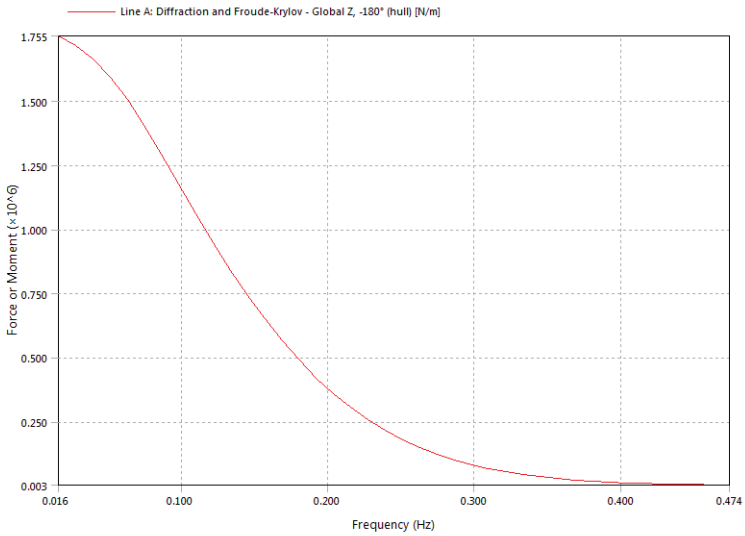

Figure B.3: Heave excitation force magnitude values for the investigated WEC.

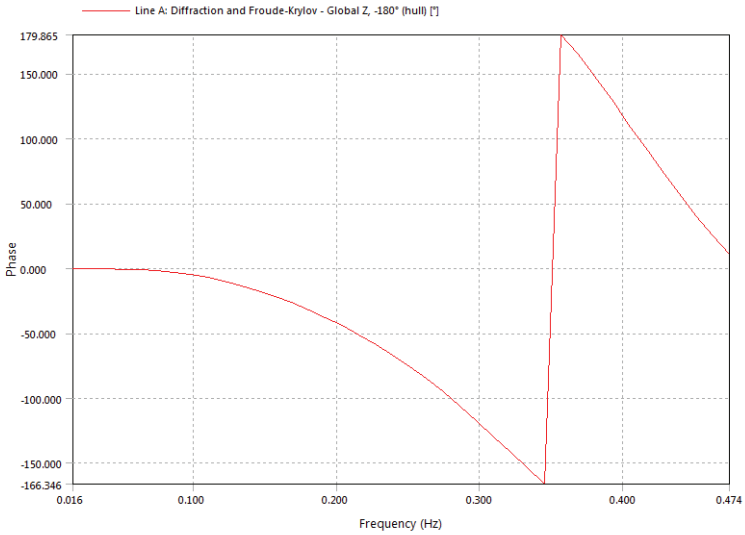

Figure B.4: Heave excitation force phase shift values for the investigated WEC.